

Microstructure Engineering in Multi-material Fibers

THÈSE N° 7922 (2017)

PRÉSENTÉE LE 27 OCTOBRE 2017

À LA FACULTÉ DES SCIENCES ET TECHNIQUES DE L'INGÉNIEUR
LABORATOIRE DES FIBRES ET MATÉRIAUX PHOTONIQUES
PROGRAMME DOCTORAL EN SCIENCE ET GÉNIE DES MATÉRIAUX

ÉCOLE POLYTECHNIQUE FÉDÉRALE DE LAUSANNE

POUR L'OBTENTION DU GRADE DE DOCTEUR ÈS SCIENCES

PAR

Wei YAN

acceptée sur proposition du jury:

Prof. F. Stellacci, président du jury
Prof. F. Sorin, directeur de thèse
Prof. T. Gacoin, rapporteur
Dr A. Stolyarov, rapporteur
Prof. M. Rappaz, rapporteur



ÉCOLE POLYTECHNIQUE
FÉDÉRALE DE LAUSANNE

Suisse
2017

To my family

Acknowledgements

On June 1st 2013, I came to EPFL, Switzerland from Shenyang, China with a four-day visa to meet Prof. Fabien Sorin who is my PhD advisor now. When I got off from M2, I realized that he and Tung (the first PhD student at FIMAP) were waiting for me at the EPFL station and I was 5 minutes late. This is not a very nice start, but I can make the course of my PhD wonderful and have a perfect ending.

I majored my Bachelor in Powder Metallurgy, and then I did a 3-year Master project in modelling of phase transition using phase-field methods. At the end of my Master, I got several PhD offers from UK, Germany, Holland and Switzerland. Except the one from EPFL, the topic of all other PhD offers was about structural materials science. To my surprise, I performed a 180° turn away from major, and into a completely new field—smart fiber devices. I was also surprised (yet delighted and grateful) that Fabien could offer me a PhD position in his group. I gradually took the reins of this project and progressively love the field. The first person I appreciate a lot is my advisor—Prof. Fabien Sorin. He has been giving me overwhelming support and warm help in all of different moments of my PhD. Fabien, apart from being an extremely smart mentor, is one of the most optimistic and positive people I have ever met in my life. This can definitely influence me forever. His vision and passion, both from scientific and human perspective, are overwhelming. I also appreciate a lot that he supported me to attend many many international conferences and seminars, and to go to MIT for an internship, and that he was extremely supportive and gave me insightful suggestions during the period when I looked for postdoc positions. I am always proud of being his PhD student.

I am grateful to all the members of the jury of my PhD exam. Thanks a lot to them—Prof. Francesco Stellacci (president) and Prof. Michel Rappaz from EPFL, Prof. Thierry Gacoin from École Polytechnique, and Dr. Alexander Stolyarov from MIT who could accept my request and will spend their precious time reading my thesis.

I have to thank a tremendous number people who have helped me develop from a naïve student into a researcher without requesting anything over the past four years: Prof. Michel Rappaz, who is always patient to answer any questions I have and shares his deep insights and knowledge in materials science; Prof. Andres Mortensen, the expert of the jury of my candidacy exam, who always gives me wonderful and inspiring comments; Prof. Tileli Vasiliki who can sacrifice her precious time to work on in-situ TEM with me; Prof. Michele Ceriotti who contributed to the nanowire formation mechanism for my Advanced Materials paper; Prof. Roland Logé who discussed with me many times about the crystal growth of Se annealed by laser; Dr. Cyril Cayron, a great scientist with strong background in materials science, who is extremely helpful in EBSD characterization and is always there for discussions with me; Prof. Li Tang who always gives me thoughtful suggestions on my career; Prof. Theo Lasser from Laboratoire d'Optique Biomédicale, living in the same village with me, who always encourages and inspires me whenever we meet; Danièle Laub, a greatly professional expert in materials sample preparation, who is my always

one of my best teachers in my work and life; Prof. Lei Wei from Nanyang Technological University, Singapore, Prof. Guangming Tao from University of Central Florida, US and Prof. Xiaoting Jia from Virginia Tech, US who are always very delighted and prompt to give me insightful comments and suggestions about my career upon I ask; Prof. Yoel Fink from MIT who accepted me for my internship in his group and shared his thoughtful ideas about research and science.

To the people of FIMAP, I don't know whether I should call them colleagues or friends. In fact, they are my friends. All of them make the atmosphere so relaxed while they are serious and rigorous researches. Everyone in the group, in his/her own way, has been one part of my life at EPFL, bringing happiness, laughter and unforgettable memories. PhD life is not easy sometimes, but I feel happy and optimistic when I stay with them. I have to thank all of them: Anne Roy, our Swiss mother, Dang Tung Nguyen, Dr. Arthur Le Bris, Chie Kitano, Alexis Page, Marco Volpi, Dr. Yunpeng Qu, Dr. Tapajyoti Dasgapat, Shahrzad Shadman Yazdi, Dr. Federica Sordo, Nicola Bartolomei, Chaoqun Dong, Louis Martin-Monier, Inès Richard, Dr. Bastien Schyrr.

My gratitude to Colette Vallotton, Gregoire Baroz, Fabienne Bobard, Dr. Duncan Alexander, Dr. Marco Cantoni, Dr. Thomas LaGrange, Dr. Emad Oveisi from Interdisciplinary Center for Electron Microscopy (CIME) for their high-level technical and theoretical support on electronic microscope. I would like to thank Martin Friedl from Laboratory of Semiconductor Materials who worked on the fabrication of Se nanowire device in CMi, Sergio Allegri from Supramolecular Nanomaterials and Interfaces Laboratory who helped me a lot on optical setup, Dr. Enrico Colla who is always there whenever I need LabView support, Andrés Burgos from Group for Photochemical Dynamics who worked on characterization of carrier lifetime in Se nanowires.

Many thanks to my friends in Lausanne. It is them who make my life here more beautiful and colorful. Meng Lin from Laboratory of Renewable Energy Science and Engineering, his wife Jiangman Zhao, Xiaoqin Zhong from Laboratory of Physical and Analytical Electrochemistry, Shiwei Zhou, Shenghan Zhang from Earthquake Engineering and Structural Dynamics Laboratory, Liu Qiu from Laboratory of Photonics and Quantum Measurements, Cuiyun Shao, Yang Sun from Laboratory of Asymmetric Catalysis and Synthesis, Marco Volpi, Pandora Sits, Francesca Sorba, Timothée Klein, Ngoc Bao Tran, Erik Poloni, Simone Giaveri and Benjamin Grena, Michael Rein and Chong Hou from MIT.

Finally, I would like to express my deepest gratitude to my family: my parents, my younger brother, and my sister-in-law who are always supportive to my choices and my decisions. Thanks a lot to my parents to allow me to pursue my PhD abroad, which means I cannot meet or stay with them whenever they need. Their deep encouragement and love are the most important driving force for my research work and career.

This is the end of my PhD, but my sincere gratitude to my PhD advisor, my colleagues, my friends, people who have helped me grow up is endless.

Abstract

The integration of conducting and semiconducting architectures within thermally drawn thin and flexible fibers is emerging as a versatile platform for smart sensors and imaging systems, medical and biological probes, energy harvesting and advanced textile. Thus far however, fundamental aspects of the microstructure formation and the interplay between microstructure and properties are poorly understood, leading to limited optical, electronic and optoelectronic performances of semiconductor-based fibers. In addition, the integration of metallic glasses, which also entails the control over microstructure and crystallization during the drawing process, has remained unexplored. The first objective of my PhD thesis is hence to shine new light on the microstructure control over fiber-integrated semiconductors, via novel post-drawing schemes and in-depth characterization. A second objective that arises in the course of the project and turns out to progress rapidly with intriguing results, is the integration of metallic glasses within fibers. This time, it is a control of the microstructure during thermal drawing that is highlighted and characterized. Regarding the former, we first compare a regular annealing treatment of the as-drawn fiber with a laser annealing approach to tailor the microstructure of semiconductors in multi-material fibers. By judiciously controlling the laser parameters, we are able to fabricate an electrically addressed polycrystalline semiconductor domain with ultra-large grains, controllable crystallization depth as well as preferentially crystallographic orientations. We then turn to a simple and robust sonochemical approach applied to the amorphous semiconductor at ambient condition without any elevated temperature. The anisotropic surface energy of crystal planes in an organic solvent allows us to control the phase and orientation of monocrystalline nanowires that grow along the desired axis, directly in intimate contact with built-in electrodes. The resulting nanowire-based fiber devices exhibit an unprecedented combination of excellent optical and optoelectronic properties in terms of light absorption, responsivity, sensitivity and response speed that compare favorably with other reported nanoscale planar devices. To highlight the potential of this novel approach, we then demonstrate a fiber-integrated architecture with two nanowire-based devices positioned around a step-index optical fiber, enabling fluorescence imaging using a single multi-functional fiber. Regarding the second objective, we demonstrate, for the first time, the integration of a metallic glass (MG) into multi-material fibers via the thermal drawing approach in the supercooled liquid region. An exquisite control over the capillary-induced instability and crystallization-induced breakup enable us to scale down the thickness of MG to tens of nanometers from the bulk while maintaining their integrity. The

crystallization-induced breakup is observed to happen when the thickness of the MG reaches around 40 nm, although this limit could be lowered by proper processing. This simple size-reduction approach indeed provides a unique platform for making nanoscale MG samples with high geometric perfection, enabling the investigation on the nanoscale size effect in crystallization via in-situ heating in a TEM. Moreover, this approach allows for the fabrication of sophisticated fiber architectures, such as MG-rod based fibers, fiber probe with many MG nanowires inside, fiber metamaterial with alternating layers of MG and polymer, and MG hollow core fiber waveguide. More surprisingly, the in-fiber MGs with varying size exhibit the same electrical conductivity as that of the raw material. To highlight the electronic application, we show a nanowire-based optoelectronic fiber in which MGs act as high-performance electrodes in contact with semiconducting nanowires. The improved control over the microstructure of various constituents in the multi-material fiber platform brings new insight in the field and paves the way towards advanced fiber-based devices of unprecedented performance and functionalities.

Keywords: thermal drawing, multi-material fibers, functional fibers, microstructure, crystallographic orientation, semiconducting nanowires, optoelectronic devices, semiconductor fibers, metallic glasses, nanoscale size effect

Résumé

L'intégration d'architectures conductrices et semi-conductrices au sein de fibres fines et flexibles étirées à chaud est maintenant considéré comme une nouvelle plateforme polyvalente pour les capteurs intelligents ainsi que les systèmes d'imagerie, les sondes médicales et biologiques, la récupération d'énergie et les textiles intelligents. Toutefois, les aspects fondamentaux de la génération des microstructures ainsi que les liens microstructure-propriétés sont encore peu compris, ce qui mène à des performances optiques, électriques et optoélectroniques limitées pour ce type de fibre. De plus, l'intégration de verre métallique qui comprend également le contrôle sur la microstructure et la cristallisation lors de l'étirage à chaud, est restée en large partie inexplorée. Le premier objectif de cette thèse concerne le développement d'une microstructure de semi-conducteurs intra-fibre contrôlée par le biais d'étirages à chaud successifs, et de caractérisations approfondies. Un second objectif qui a émergé au cours du projet et qui progresse rapidement concerne l'intégration des verres métalliques dans les fibres. C'est cette fois-ci un contrôle de la microstructure lors de l'étirage à chaud qui est étudié en profondeur. Concernant le premier point, nous comparons d'abord un traitement thermique usuel d'une fibre étirée à chaud avec un traitement laser pour adapter la microstructure de semi-conducteurs dans les fibres multi-matériaux. Par un contrôle judicieux des paramètres du laser, nous sommes capables de fabriquer un domaine semi-conducteur polycristallin testé électriquement avec des grains ultra-larges, une profondeur de cristallisation contrôlable ainsi que des orientations cristallographiques préférentielles. Nous nous tournons ensuite vers une approche par sonication et traitement chimique simple et robuste appliqué à un semi-conducteur amorphe sous atmosphère ambiante sans élévation de température. L'anisotropie de l'énergie de surface de plans cristallins dans le solvant nous permet de contrôler la phase ainsi que l'orientation de nanofils monocristallins qui croissent selon l'axe désiré, en contact direct avec les électrodes intégrées. La fibre résultante possède des performances électroniques et optoélectroniques sans précédent à la fois en termes d'absorption de la lumière, temps de réponse, sensibilité, et type de réponse. Les performances sont nettement meilleures que l'ensemble des dispositifs plans à l'échelle nanométrique reportés dans la littérature. Nous démontrons ensuite une architecture particulière de fibre contenant deux dispositifs à base de nanofils placés autour d'une fibre optique à saut d'indice, permettant l'imagerie par fluorescence à l'aide d'une seule fibre multifonctionnelle. Concernant le second objectif, nous démontrons pour la première fois l'intégration de verres métalliques au sein des fibres multi-matériaux par la méthode de l'étirage

à chaud dans la région liquide hyper-refroidie. Un contrôle original sur les instabilités capillaires et liées à la cristallisation nous permet de réduire l'épaisseur des verres métalliques jusqu'à quelques dizaines de nanomètres tout en maintenant la continuité. La rupture induite par cristallisation se produit lorsque l'épaisseur du verre métallique atteint quelque 40 nm. Il est probable que cette fragmentation puisse être contournée en exploitant l'évolution des températures de cristallisation à l'échelle nanométrique en utilisant la microscopie électronique en transmission in situ. Nous sommes également capables de fabriquer des architectures de fibres plus sophistiquées, comme des cylindres à base de barreaux en verre métallique, des fibres sonde contenant une multitude de nanofils de verre métallique, des fibres méta-matériaux avec des couches alternées de polymère et de verre métallique, et des guides d'ondes creux à base de verre métallique. De manière plus surprenante, les nanofils de verre métallique de différentes tailles possèdent la même conductivité électrique que le matériau massif. Afin de surligner les applications électroniques, nous démontrons une fibre optoélectronique à base de nanofils en verre métallique qui agissent comme des électrodes à haute performance en contact avec des nanofils semi-conducteurs. Le contrôle amélioré sur plusieurs composants des fibres multimatériaux fournit un nouveau regard sur le domaine et entrouvre la voie vers des dispositifs à base de fibres multimatériaux aux performances et fonctionnalités jusqu'ici inégalées.

Mots-clés : étirage à chaud, fibres multi-matériaux, fibres fonctionnelles, microstructure, orientation cristallographique, nanofils semi-conducteurs, dispositifs optoélectroniques, verres métalliques, effet de réduction d'échelle

Contents

Acknowledgements	I
Abstract	III
Résumé.....	V
Chapter 1 Introduction	1
1.1 The advent of multi-material fibers	1
1.2 Multi-material fiber fabrication approaches	1
1.2.1 Direct thermal drawing.....	1
1.2.2 High-pressure chemical vapor deposition	2
1.3 Applications of multi-material fibers	3
1.3.1 Photonic fibers.....	3
1.3.2 Optoelectronic fibers	5
1.3.2 In-fiber synthesis and fabrication	8
1.4 Challenges in multi-material fibers field	14
1.4.1 Microstructure control over in-fiber semiconductors.....	14
1.4.2 Development of complex functionalities in fibers	15
1.4.3 In-fiber breakup of metallic elements	16
1.5 Objective and outline of the thesis	17
Chapter 2 Polycrystalline Semiconductor-based Optoelectronic Fibers	21
2.1 Fiber Fabrication and Characterization.....	21
2.2 Furnace-induced crystallization and characterization.....	22
2.3 Laser-induced crystallization and characterization.....	27
2.4 Discussion and summary	30
2.5 Experimental methods	32
Chapter 3 Controlling the Crystallographic Orientation of Semiconductors in Optoelectronic Fibers	33
3.1 Fiber Fabrication and Characterization.....	33
3.2 Crystallization strategy, crystallographic and performance characterization	34
3.3 Discussion and summary	46
3.4 Experimental methods	55
Chapter 4 Monocrystalline Semiconductor Nanowire-based Optoelectronic Fibers	57

4.1 Fiber Fabrication and Characterization	57
4.2 Nanowire synthesis and growth mechanism	58
4.3 Optical and optoelectronic characterization on the precursor fiber	64
4.4 Hybrid fiber making, characterization and application	70
4.5 Large-area integration of nanowires.....	74
4.6 Discussion and summary.....	75
4.7 Experimental methods.....	77
Chapter 5 Metallic Glass Nanostructure-based Multi-material Fibers	79
5.1 Materials selection.....	79
5.1 MG ribbon-based fiber fabrication, characterization and minimal feature size	80
5.2 Sophisticated fiber architecture	86
5.3 Electrical conductivity and electronic application	87
5.4 Nanoscale size effect in crystallization	90
5.5 Discussion and summary.....	94
5.6 Experimental methods.....	97
Chapter 6 Conclusions and outlook	99
Bibliography	103
Curriculum Vitae	111

Chapter 1 Introduction

1.1 The advent of multi-material fibers

Ever since their invention, optical fibers have revolutionized our world through the delivery of internet and telecommunication thanks to ultralow signal loss at near infrared wavelengths. Optical fibers also open a breadth of applications beyond telecommunication, including minimally invasive in situ and in vivo bio-compatible probing and imaging of biological tissues[1], fiber lasers[2], remote strain-, heat- and chemical-sensing[3], nonlinear optics and nanophotonics[4]. The realization of all these applications relies not only on optical waveguide through optical fibers but also on functionalities of other optical components that are outside the fibers, such as laser sources, modulators and photodetectors. From a material perspective, optical fibers are mainly constituted by silica glass although they can also be made of polymers[5]. From a geometry perspective, the architecture of optical fibers is very simple, i.e., a core surrounded by a cladding with a slightly lower refractive index. Today however, several applications will require the integration of different components and devices inside fibers with more sophisticated structures. A new family of multi-material fibers that integrate different materials with disparate optical, electronic, optoelectronic and thermomechanical properties has therefore emerged[6]. These fibers are endowed with complicated architectures and thereby more complex functionalities beyond optical communication.

1.2 Multi-material fiber fabrication approaches

1.2.1 Direct thermal drawing

Hundreds-of-kilometer long optical fibers are typically produced by pulling from a so-called preform at the softening temperature of silica. With the same simple technique, the new family of multi-material fibers is typically fabricated by thermal drawing of a macroscopic preform, which has exactly the same composition and geometry as the final fiber, but is much larger in the transverse direction and shorter in length. The preform can be fabricated via many approaches, for example, thin-film rolling technique for cylindrical fibers[2], extrusion[5], stack-and-draw approach[5], assembling different components together via consolidation in a hot press and additive manufacturing[7]. The preform is then fed into a furnace where multimaterials soften or melt. An external force applied by a capstan pulls the soft preform into fibers, the size of which can be controlled by the drawing temperature of the hottest zone of the furnace, the feeding speed

of the preform, and the drawing tension, as schematically shown in Fig. 1.1. In order to maintain the identical architecture and cross-sectional integrity of the preform at the fiber level, several criteria for co-drawing of different materials with disparate thermomechanical properties are required: i) The cladding encapsulates all other materials and components and supports most of the stress; therefore, it should be amorphous and resist devitrification during the thermal drawing. It must be processed at a relatively high viscosity regime, typically between 10^4 and 10^8 Pa·s, in which the derivative of viscosity with respect to temperature is continuous and small. Hence, the typical cladding materials are glasses and amorphous polymers; iii) when different polymers or glasses are combined into the fibers, they should exhibit compatible viscosity at the drawing temperature to avoid the deformation and delamination of the interface. The processing temperature window (between glass transition and crystallization temperature) should be big enough so that the amorphous material does not crystallize or degrade before it is plastically deformed; iii) when crystalline materials are incorporated into fibers, the melting point of these materials should be lower than the drawing temperature. Crystalline materials therefore flow in a liquid state during drawing and they should be well encapsulated in the preform. Other materials that interface with crystalline materials should not in the liquid state during drawing to avoid the mixture of different materials; iv) all the materials must have relatively similar thermal expansion coefficients at the drawing temperature to avoid cracks and fractures formation and limit the residual stress in fibers.

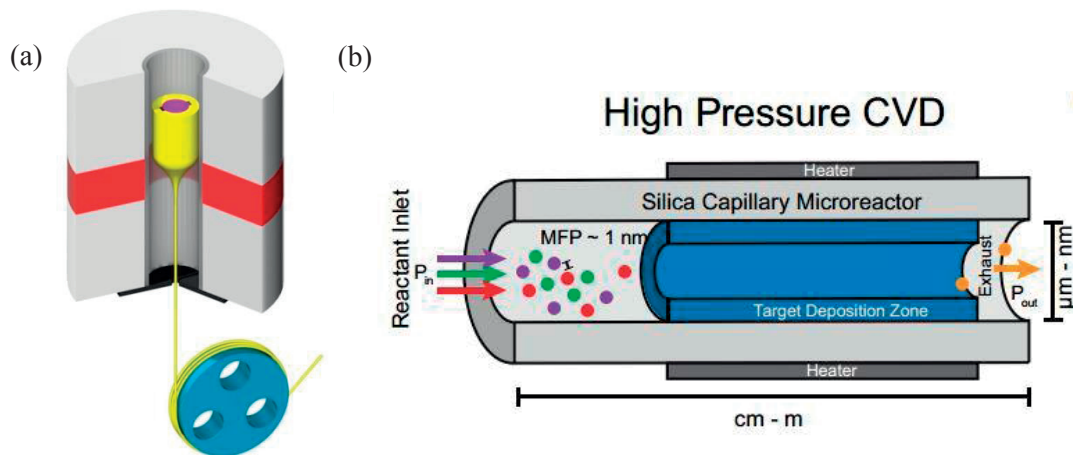


Fig. 1.1 (a) Schematic of preform to fiber thermal drawing[2]; (b) High-pressure chemical vapor deposition of functional materials in optical fibers[2].

1.2.2 High-pressure chemical vapor deposition

Fabrication of multi-material fiber via high-pressure chemical vapor deposition (HPCVD) was first reported in 2006 by John Badding's group[8]. Microstructured optical fibers (MOFs) are first fabricated via a conventional thermal drawing approach, and then a wide range of technologically important metals and semiconductors are deposited within the voids of tens of meters of MOFs by high-pressure microfluidic chemical deposition. Very high pressures (10 to 100 MPa) flow ensures a perfect conformal deposition onto the walls of the long and extremely narrow capillaries of MOFs, eliminating mass-transport constraints and enabling highly uniform coating materials in MOFs. It was shown that metals, single-crystal semiconductors, and polycrystalline elemental or compound semiconductors wires with diameters of microscale down to nanoscale can be easily fabricated. By controlling the processing temperature and the size of the pores in fibers, the morphology, crystallinity and crystallographic orientation of functional materials can be tailored. A key advantage of this fabrication approach is that coaxial homo- and hetero-junctions can be realized by sequentially changing the gas composition during deposition[9]. This technique paves a novel way towards fiber-integrated optoelectronic materials and devices[8].

1.3 Applications of multi-material fibers

1.3.1 Photonic fibers

The first multi-material fiber fabricated by the thermal drawing approach can be traced back to 2002 when B. Temelkuran and his colleagues developed a hollow optical fiber lined with an all-dielectric omnidirectional reflector that consists of multiple alternating layers of a high-refractive-index chalcogenide glass and a low-refractive-index polymer, as shown in Fig. 1.2a. Thanks to the large photonic bandgaps established by the alternating layers, this fiber can efficiently transmit CO₂ laser light at 10.6 μm wavelength with a loss as low as below 1.0 dBm⁻¹ [10]. The breakthrough of this technology directly leads to the commercialized fiber CO₂ laser surgery by OmniGuide Surgical. Almost at the same time, people from the same group reported on fabrication of omnidirectional dielectric mirror fibers by placing 21 layers of alternating refractive index on the outer surface of a polymer core (Fig. 1.2b). These fibers may be weaved into fabrics or cloth (Fig. 1.2c) for radiation barriers and spectral-identity verification, and may also be used as optical filters[11]. The introduction of intentional deviations from periodic multilayers into the photonic bandgaps fibers allows for the creation of optical cavities[12]. When an optical pump guided along the fiber axis excites the gain medium inserted into the

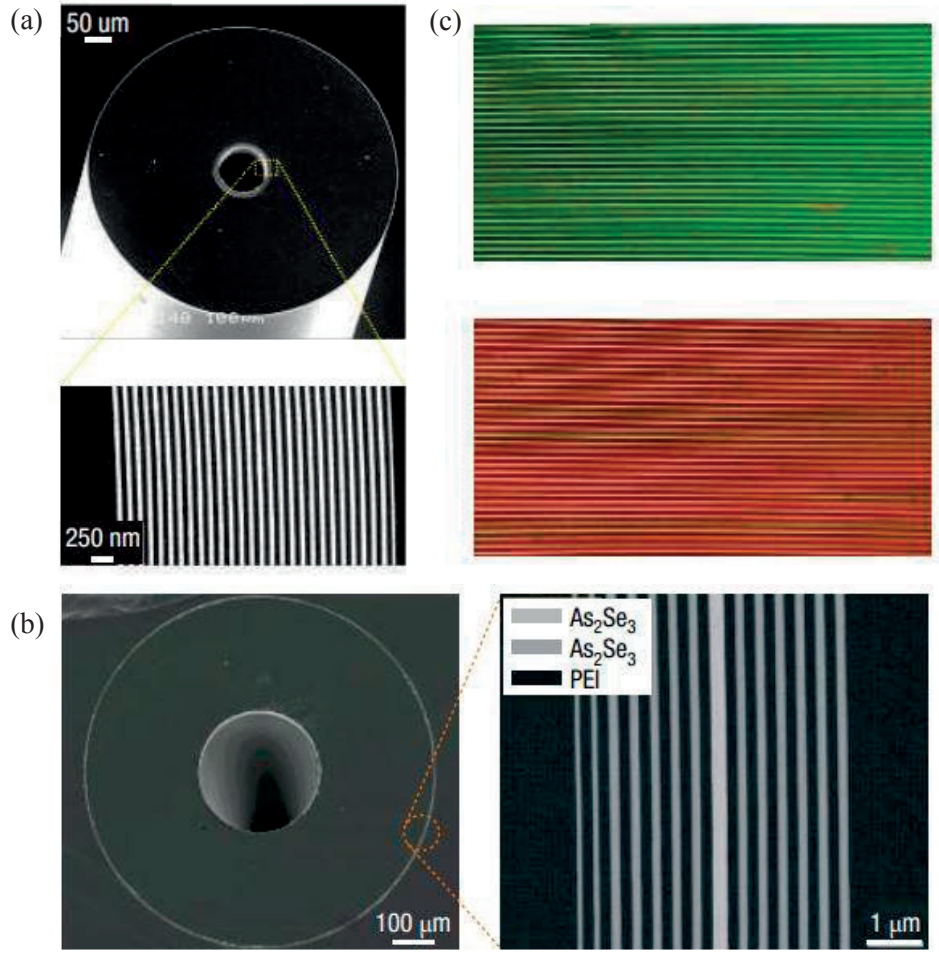


Fig. 1.2 (a) Scanning electron microscope (SEM) micrographs of the cross-section of a hollow-core photonic bandgap fiber[6]; (b) SEM micrographs of the cross-section of an omnidirectional dielectric mirror fiber[6]; (c) Photographs of external reflecting fibers[6].

hollow core of a photonic bandgaps fiber, it provides the longitudinal confinement of the higher-frequency optical pump and enables the creation of laser emission in the radial direction from the fiber surface[13]. This contrasts with conventional fiber lasers that emit only along the fiber axis. Encircling the laser cavity in the fiber core with an array of electrically contacted liquid-crystal microchannels incorporated in the fiber cladding can modulate the polarized wavefront emanating from the fiber core, leading to a laser with a dynamically controlled intensity distribution passing through the full azimuthal angular range[14].

The light guidance in the hollow core of the abovementioned photonic bandgaps fibers is realized by the Bragg reflection mechanism. Exploiting the refractive-index contrast of two

materials in fibers is the classical mechanism for light guidance at the telecommunication wavelengths. This also promotes the development of semiconductor core optical fibers that show promises for infrared power delivery and nonlinear signal processing[9]. The first semiconductor optical fiber was reported by J. Ballato in 2008 when a silicon core, silica glass-clad fiber was fabricated using conventional thermal drawing approach[15]. Hereafter, a wide range of semiconductors, such as Ge[16], SiGe[17] and InSb[18], were incorporated into silica-based optical fibers. These advances have extended the accessible wavelength range and opened up several practical applications[17]. To date, the best fibers exhibit optical loss of 2 dB/cm in the near-infrared and about 4 dB/m in the mid-infrared range and it seems that achieving the loss of 50 dB/km is possible with continued efforts[18]. The optical properties of these fibers can be drastically improved by controlling the phase, compositional segregation, grain size, crystallinity and crystallographic orientation[18][17]. This will be discussed in the “In-fiber fabrication” section of the Introduction.

Although this highly scalable thermal drawing approach allows for simple and robust batch-fabrication of very long lengths of semiconductor optical fibers in a single step, the fibers exhibit a very high numerical aperture (the sine of the maximum angle of an incident ray with respect to the fiber axis, so that the transmitted beam is guided in the core) and thereby a large number of modes that is detrimental to the optical properties. A straightforward way to bypass this problem is to exploit the existing silica photonic crystal fibers with many pores as templates where functional materials are deposited via high-pressure chemical vapor deposition technique[19][20]. Furthermore, many materials (e.g., hydrogenated silicon[21], ZnSe[22], ZnS[23], ZnO[23]) that cannot be directly drawn via thermal drawing approach can be simply deposited via HPCVD, rendering them useful for applications in nonlinear optical fibers, high-speed optical switching, fiber waveguides with very low loss and photovoltaics.

1.3.2 Optoelectronic fibers

The light-guiding mechanism of the optical fibers in 1.3.1 section is either photonic bandgap effects or step index. Here, the refractive-index of semiconductors is exploited to create large photonic bandgaps or total internal reflection. The utilization of another intriguing attribute of semiconductors—electronic band gap as well as the incorporation of metals results in the creation of metal-insulator-semiconductor optoelectronic fiber devices[24]. An amorphous semiconductor core contacted by four metallic microwires and surrounded by a transparent polymer cladding

exhibit photosensitivity along the entire fiber length (Fig. 1.3a). These fibers are both highly flexible and mechanically tough, which allow them to be woven into functional fabric that can identify the location of an illumination point[24]. These flexible fibers can also be woven into an optical array or web—a closed-surface sphere, enabling measuring the amplitude and phase of an electromagnetic field over large areas. Specifically, the direction of an illumination over 4π steradians was first measured via a spherical web made of photodetecting fibers, and then a planar array was employed to measure the intensity distribution using a tomographic algorithm[25]. While localization of illumination points from the space can be realized by a photodetecting mesh structure, another approach is to break the axial symmetry through the construction of a convex electrical potential along the fiber length[26]. The localization of an illumination point along a one-meter photodetecting fiber with a sub-centimeter resolution was achieved. The width of the incoming beam and the photoconductivity could also be extracted[26]. A limitation of these fibers, however, is the challenge of integrating multiple optoelectronic devices into a single fiber. More complicated fiber architecture enables more complex functionalities. F. Sorin and his colleagues then demonstrated the successful integration of eight photodetecting devices (Fig. 1.3b) into a single optoelectronic fiber in which components down to 100 nm were achieved[27]. This unique fiber was able to discriminate the wavelength in the visible range at below 5 nm resolution and measure the angle of incidence down to 4° angular resolution[27]. It was then shown that device performance can be improved by engineering the structures and geometries. In particular, decreasing chalcogenide semiconductor bulk to a thin film configuration (Fig. 1.3c) leads to a significant improvement in sensitivity of the photodetecting device[28]. Moreover, the unique assembly of single fibers into constructs and fabrics not only can localize the illumination point from the space but also can image a complex object with polychromatic light, noninterferometrically and without lenses[27][25]. All abovementioned functionalities are realized by virtue of a photosensitive semiconductor in fibers. Another application for these photosensitive fibers is remote and distributed chemical sensing[29]. Specifically, an in-fiber chemiluminescent semiconductor flanked a hollow core through which chemical vapor can flow was able to detect the chemiluminescent signals from the reaction down to 10 ppb.

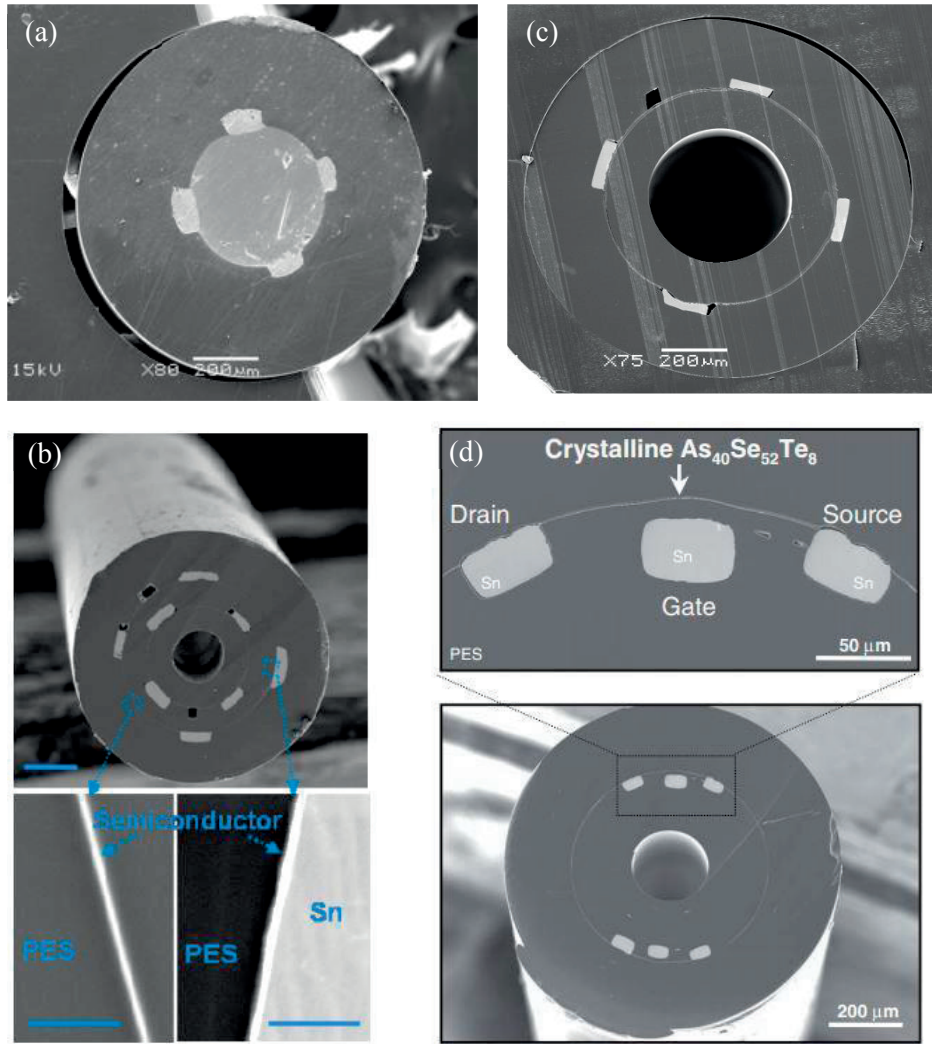


Fig. 1.3 (a) SEM cross-section of a fiber in which a solid semiconductor core contacted by four metallic electrodes[24]; (b) SEM of a dual-ring fiber where the position of the electrodes contacting the inner layer are rotated by 45° with respect to those contacting the outer layer[27] (scale bar, 1 μm); (c) SEM cross-section of a fiber in which a semiconductor thin film contacted by four metallic electrodes[28]; (d) SEM micrograph of a field-effect transistor fiber[30].

Besides these interesting functionalities, the unique combination of metallic source/drain and gate as well as semiconducting thin film created single-fiber field-effect transistors (Fig. 1.3d), opening a new area of fiber-based discrete logic elements capable of digital signal processing[30]. The ability to integrate thermal sensitive semiconductor whose electrical conductivity varies with small changes in temperature into fibers has also enabled the realization of large-contact-area temperature sensing at high spatial resolution[31]. When such thermal-detection elements were

assembled in the vicinity of a hollow-core multilayer cylindrical photonic bandgap fiber core, the electrical signal change is able to tell normal transmission conditions from those with a leakage caused by heat-generated defects on the fiber[32].

The alternative strategy for the monolithic integration of metal and semiconductor in fibers relies on exploiting HPCVD techniques. It allows for the deposition of semiconductors with high-melting points and unique devices (p-n junction, Schottky junction, p-i-n junction) which is very challenging to fabricate by thermal co-drawing technique. The fabrication of Pt/n-Si Schottky junction via HPCVD was first demonstrated. The junction had a barrier height of 0.8 eV and exhibited a 3 dB bandwidth up to 3 GHz at a wavelength of 1,550 nm, enabling high-speed photodetection at telecommunications wavelengths[33]. The quantum efficiency of Schottky photodiodes is, however, relatively low, which makes them unfavorable for photodetecting and photovoltaic applications.

To summarize this part, conventional optoelectronic devices, such as photoconductor, field-effect transistors or photovoltaics cells are for the most part produced using the standard wafer-based processes. Although these techniques are very mature and can provide small-size and low-cost devices, it remains restricted to planar geometries as well as rather small and mechanically rigid substrates. However, the unique combination of metals, insulators and semiconductors into fibers via direct thermal drawing or HPCVD delivers electronic and optoelectronic functionalities over large-area, flexible, soft and stretchable substrates.

1.3.2 In-fiber synthesis and fabrication

Conventional thermal drawing of multi-material fibers allows for geometric scale-down in which the fiber materials and architecture are identical to those in the preform. The ability to allow disparate materials in fibers to physically mix, chemically react and form novel compounds during drawing increases the complexity and functionalities of fiber devices. The first fiber draw synthesis was reported on high-melting point ZnSe formation in situ during low-temperature thermal drawing[34]. It was discovered that drawing a polymer preform integrating a thin layer of Se_{97}S_3 contacted by $\text{Sn}_{85}\text{Zn}_{15}$ metallic electrodes into fibers yielded electrically contacted crystalline ZnSe domains at the interface between the metallic elements and the selenium-based layer. The fiber device exhibited a rectifying behavior, thanks to the large discontinuity in the valence band at the $\text{Se}_{97}\text{S}_3/\text{ZnSe}$ interface. The noise-equivalent power of this device was 1000 times lower than previous multimaterial thin-film photodetecting devices[34]. This reaction,

however, was limited only to the surface of the electrode while the bulk was not utilized. In addition, the other element in the alloyed electrode did not contribute to the chemical reaction. Both of the two fundamental drawbacks restrict high-throughput ZnSe formation[35]. Replacing Zn-based electrode with pure Zn that mechanically broke up during drawing significantly increased the volume of ZnSe. This work also provided direct atomic-level compositional and structural analysis of the ZnSe and experimentally probed the thermodynamics and kinetics of the compound formation. Another chemical reaction during thermal drawing was observed in the high-temperature silica platform. When drawing an aluminium rod clad by a silica tube, the silicon atoms in silica diffused into the aluminium core and formed a high-quality crystalline silicon domain[36].

While the preform serves as a microcrucible for chemical reaction and new materials formation, it also allows one to modify the geometry rather than the composition of materials during thermal drawing. In particular, D.S. Deng and his colleagues first discovered that the initially intact cylindrical thin film shell broke up along the circumferential direction into an ordered array of filaments while uniformity was maintained in the axial direction[37]. This happened when the thickness of the thin film reached a critical value. Highly dense nanofilaments with extremely long lengths can be harvested by dissolving the polymer cladding, which provided an innovative way for mass-fabrication of nanowires. A fluid front instability mechanism was proposed to account for the observed phenomena. The fluid instability was then systematically explored from the perspective of classical Plateau-Rayleigh instability mechanism[38]. The surface tension and viscosity contrast between the core and cladding dependence of instability time scale was elegantly investigated, providing a theoretical guidance to material selection, drawing parameters and structure formation in fibers. Another straightforward way to produce nanowires in fibers is via the iterative thermal drawing approach[39][40]. Fibers obtained from previous draw were embedded in new preforms and were repeatedly drawn, resulting in a continuous size reduction of active materials inside fibers. Semiconducting nanowires with a feature size down to a few nanometers while maintaining axial continuity were produced.

Besides the fabrication of in-fiber nanowires during thermal drawing, the fiber is also a unique platform to fabricate micro- and nano-spheres post-drawing based on Plateau-Rayleigh instability. This capillary instability in multi-material fibers was first observed during tapering of a fiber using a heating setup post-drawing (Fig. 1.4a)[41]. The chalcogenide glass core remained intact at lower temperature due to a large viscosity. As temperature increased, the viscosity decreased

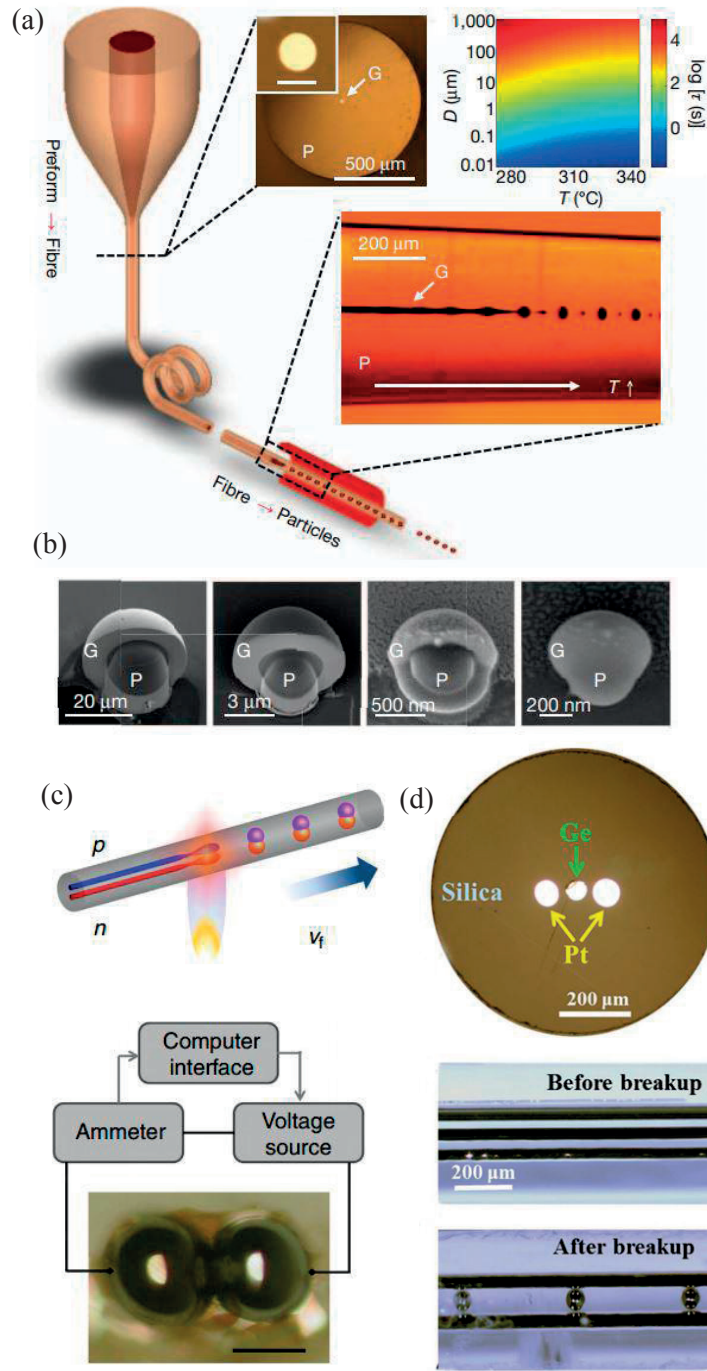


Fig. 1.4 (a) Thermal annealing of the as-drawn fiber results in the breakup of the intact core into spheres[38]; (b) Four differently sized core/shell particles[38]; (c) breakup of a double-core fiber into bispherical clusters, forming p-n junction in fibers[41]; (d) Triple core fiber before and after selective breakup process[42].

and surface tension overcame the viscous force, leading to the growth of perturbation at the surface until spheres were formed. The chalcogenide glass core broke up into a periodic string of size-tunable micro-scale particles embedded along the fiber length[41]. Hereafter, spherical particles with a wide range of diameters: from 2 mm down to 20 nm and spherical systems with complicated structure, such as core-shell particles (Fig. 1.4b) were reported[42] [43] [44]. This in-fiber break-up technology also allows for the fabrication of novel semiconducting sphere-based electronic and optoelectronic devices. When a fiber with dual cores comprised of a p-type and an n-type silicon wire was fed into a flame with axial thermal gradient, both of them broke up and attached with each other into a bispherical silicon p-n junction (Fig. 1.4c)[45]. Selective breakup in which only one domain experiences breakup while the others remain intact during thermal treatment can also be induced in the fiber system, resulting in novel optoelectronic devices (Fig. 1.4d) [46] [47].

The small cross-section and large aspect ratio of the fiber also provide a unique platform to tailor the microstructure of in-fiber semiconductors and to study some fundamental topics in materials science. The sphere formation is associated with solidification in fibers. The cooling rate and temperature gradient can strongly influence the microstructure of the solidified materials, especially in alloy systems. This was shown in $\text{Si}_{0.5}\text{Ge}_{0.5}$ (phase diagram of Si-Ge alloy can be found in Reference [17]) core surrounded by a silica cladding system. Feeding this fiber in a flame locally melted the core and made the cladding soft, leading to the breakup of the semiconductor core into liquid droplets embedded in silica. As the fiber exited the flame, the droplets solidified in a temperature gradient imposed by the flame with a solidification front propagated from the cold side toward the hot side. As the solidification propagates, Ge was rejected to the liquid phase due to a higher solubility of Ge in the liquid state. An increased Ge content in the liquid reduced the melting point. Ultimately, the Ge content in the liquid approached unity and the melting point reached that of pure Ge. This solidification process resulted in Janus particles having a Si-rich lobe and a Ge-rich lobe (Fig. 1.5a)[48]. However, the cooling rate and thermal gradient in the flame system cannot be precisely controlled. A more promising way to realize this is a laser system because laser is able to accurately deliver high-dense energy into confined regions in fibers and also allows one to control the shut-off rate. Very recently, D.A. Coucheron and his colleagues[17] reported the fabrication of large single crystals with uniform composition of a SiGe core of a silica clad fiber fabricated by thermal drawing via

laser-melting approach. The silica glass cladding can serve as an efficient crucible for controlling material microstructure, elemental segregation and crystallographic structure of the core, thereby

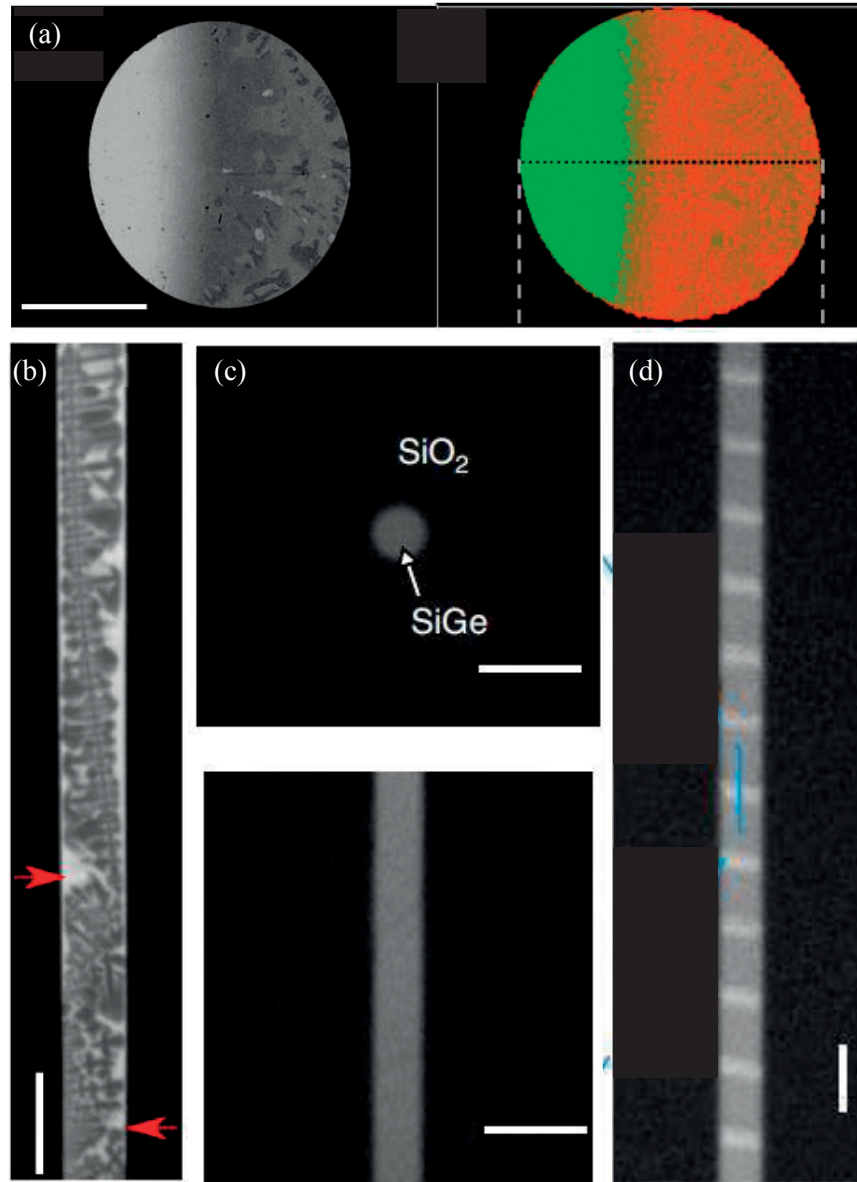


Fig. 1.5 (a) left: SEM backscattered electron image of the cross-section of a $\text{Si}_{0.5}\text{Ge}_{0.5}$ sphere after solidification (scale bar, 50 μm); right: EDS map of the sphere [48]; (b) XCT image of dendritic structures in $\text{Si}_{0.75}\text{Ge}_{0.25}$ core of an as-drawn fiber [48]; (c) XCT image of the cross-section and the side view of a fiber after laser melting [17]; (d) Ge-rich grating formed in the fibre core by periodically interrupting the laser beam. (scale bar, 200 μm for b, c and d) [17]

tailoring the optical properties of the fiber. In particular, they could suppress constitutional undercooling by controlling the translation rate of the laser and therefore allowed the solid/liquid interface to advance with a planar morphology and no microsegregation occurring in the alloy (Fig. 1.5b and c). It is the first time the SiGe alloy, the composition of which determines the bandgap and optical properties, is introduced in a fiber configuration, which opens novel opportunities for fiber based devices. From a fundamental point of view, this scheme provides a novel tool to re-investigate classic microsegregation-free mechanisms (constitutional supercooling principle, the limit of absolute stability and partitionless solidification). The segregation of elements in the alloy system can be overcome, but it can also be utilized to create gradient composition structures in fibers by controlling the power density. A compositional grating comprised of Ge-rich regions and Si-rich regions with the period of 40 μm was demonstrated[17]. Here, the laser used to write the grating is a CO_2 laser that heats the glass cladding while the core is melted via conductive heat. Ultrashort pulse laser have been used to introduce strain within the glass cladding and at the interface between the glass and core. The strained core material exhibited modified refractive index, enabling Bragg grating written into a silicon optical fiber[49].

High-melting point semiconductors, such as Si, Ge, SiGe, waveguides in fiber form bring a large range of scientific and technological impacts. Two approaches have been widely used to the fabrication of such fibers. The first one is HPCVD that affords the unique capability of depositing semiconducting materials with high-purity, void-free and amorphous characteristics. The second one is molten core thermal drawing that leads to polycrystalline semiconductors in fibers. Both of the amorphous and polycrystalline semiconductors-based fibers exhibit high optical loss due to the defects in materials. Therefore, postfabrication treatments are required to tailor the crystallinity and control the grain size. Laser remelting also exhibits powerful capability in this manner to improve the optical transmission. A CO_2 laser was exploited to directly re-melt an as-drawn 12 μm silicon core fiber, resulting in fibers with single crystal cores over the entire scanned region. The optical loss significantly decreases with increasing the cooling rate, leading to a low loss as 2 dB/cm at 1.55 μm , and 1 dB/cm at a wavelength of 2 μm [50]. Both of the cooling rate and the power of the laser affect single crystal formation. X. Ji and his colleagues recently constructed a laser processing diagram that revealed a window within which single silicon crystal can be grown. They showed the creation of single crystal silicon core fibers by laser remelting amorphous silicon deposited in silica fibers by HPCVD. The single crystal fibers,

as long as 5.1 mm, exhibited very low optical loss down to 0.47 dB/cm at the standard telecommunication wavelength and a superior photosensitivity comparable to bulk silicon[51]. They further reported the fabrication of the first small core single crystal Ge fibers, up to 9 mm long, and with optical loss down to 1.33 dB/cm at 2 μm , which is 25 times lower than the lowest loss reported for Ge core optical fibers at this wavelength[52]. These fibers could potentially find applications in low-loss infrared waveguides for imaging spectroscopic endoscope, nonlinear optical devices[53] at the mid-infrared, and can be integrated with in-fiber Si photonic devices for photodetecting at the wavelength of 1.55 μm .

It is worth noting that the first attempt using postfabrication schemes to modify the semiconductor core in silica cladding optical fibers can be dated back to 2011 when J. Ballato's group used rapid photothermal processing to anneal glass-clad silicon optical fibers under an ultrahigh-purity nitrogen environment at 950 °C. The annealed fiber exhibited improved local crystallinity and single crystal with a length of at least 9 mm was reported[54]. Furthermore, the nature of the crystallographic orientation of the core material relative to the fiber axes and the influence of core geometry on the crystallography were investigated[55][56]. While furnace-based thermal annealing is not much favored due to the uncontrolled heating or cooling rate and thermal gradient, it was reported that multi-step annealing of the amorphous silicon core below its melting point deposited in the internal channel of silica fibers via HPCVD allowed for an increase in the polycrystalline grain size and decrease in the defects[57]. A low optical loss of below 1 dB/cm at a wavelength of 2.2 μm was thus realized, much lower than that reported for small core size crystalline silicon fibers and comparable to the loss in many planar semiconductor waveguides. Further reduction in optical loss when optimizing annealing technique can be anticipated[57].

1.4 Challenges in multi-material fibers field

1.4.1 Microstructure control over in-fiber semiconductors

As introduced in the previous sections, the recent ability to position electrically conducting and semiconducting domains at prescribed positions within optical fibers is opening a breadth of novel opportunities for advanced medical and biological probes, flexible smart sensors and imaging systems, nanophotonics, light generation and communication, energy harvesting and advanced textiles. To functionalize optical fibers, a first strategy relies on wafer-based techniques and HPCVD to integrate functional materials at the tip or within a few tens of centimeters of

microstructured silica fibers. An alternative approach exploits the well-established thermal drawing of macroscopic preforms that integrate the desired multi-material architecture. This has the advantage of simplicity and scalability, since the fiber pulling step results in tens of kilometers of fibers that have the same cross-sectional structure as the initial preform. Thus far however, realizing high quality semiconducting materials that can act as high-performance photodetectors using the thermal drawing process remains a challenge. A recent strategy consists in the thermal drawing within silica fibers of high melting point materials such as silicon, germanium or various compounds. The melting and solidification during drawing result however in semiconductors with a highly polycrystalline microstructure, requiring local post-drawing annealing or laser-based steps to engineer a desired microstructure. It is also difficult to integrate electrodes in contact with the semiconducting domains and despite an ingenious and promising method, no device with good optoelectronic properties has been shown. The alternative strategy relies on exploiting the polymer fiber platform. It has several advantages compared to its silica counterpart, including low temperature processing, robust mechanical properties, simple integration of electrodes, and the ability to impart fibers with complex architectures and multiple functionalities. Thus far, however, the post-drawing crystallization schemes applied to semiconducting chalcogenide glasses have resulted in poor control over the microstructure in terms of the phase, grain size, crystallization volume and orientation[58]. From an optical point of view, grain boundary accumulates impurities and is generally detrimental for light transmission. From an electronic point of view, grain boundaries serve as charge carrier recombination centers which generally impair charge transport and limit optoelectronic properties. If the microstructure of the semiconducting element can be controlled to exhibit large grain sizes and ideally single crystal domains between the connecting electrodes, a drastic increase of performance is expected[59].

1.4.2 Development of complex functionalities in fibers

In 1965, Intel cofounder Gordon Moore predicted that transistors were shrinking so fast that the number of them on a microprocessor chip could double every two year or so, which means that the chip's performance will, too. For the past five decades, the chip industry has kept Moore's law alive, rendering more and more powerful computers possible. Likewise, increasing the density of optical, electronic and optoelectronic devices integrated in a single multi-material fiber can deliver a wide range of complex functionalities. A fiber that combines a semiconducting thin film heat-sensing device with a hollow-core PBG transmission component is able to both

deliver high optical power and detect temperature change associated with imminent failure in the PBG[32]. Another striking example is the incorporation of eight distinct functional devices into a single fiber, enabling the extraction of information on the direction, wavelength, and potentially even color of incident radiation over a wide spectral range in the visible regime[27]. Despite these successful achievements, the incorporation of multiple devices into a single fiber still remains a big challenge in the field. This can be attributed to the following three reasons: 1) Differentiating a variety of different stimuli. Optoelectronic fibers that integrate different semiconductors can sense a variety of stimuli, such as light, heat, ultrasound waves, pressure and chemicals. It is possible however that these stimuli simultaneously influence physical properties of one semiconducting component, and different stimuli give rise to the same response. 2) Integration of new materials with novel properties. The requirement on compatible thermophysical properties for different materials limits the type of materials that can be co-drawn and the device architectures that can be fabricated via thermal drawing. The discovery and design of new materials is a straightforward way to solve this problem. 3) Miniaturization of devices. Increasing the density of devices requires that the feature size of devices can be scaled down as small as possible while maintaining their functionality. However, many current fiber components either cannot be drawn into small scale or lose functionalities at small scale.

1.4.3 In-fiber breakup of metallic elements

As discussed in the last section, driving devices towards smaller and smaller scales is required to develop advanced and novel applications for functional fibers. A simple way to achieve this is to repeatedly draw fibers to scale down the size of the components at each iteration. For some semiconductors that can be thermally drawn into fibers in the supercooled liquid region (between T_g and T_x), their feature size can reach tens of nanometers[37][60]. However, metallic components lose their continuity once the size is reduced to microscale due to a capillary instability [61][62]. Replacing the regular metallic elements in multi-material fibers with another conducting element that can be scaled down to nanoscale while maintaining excellent performances such as high electrical conductivity, will lead to the following impacts: 1) Metal-semiconductor-insulator devices can be scaled down to nanoscale. 2) Improvement of the interface between active materials and electrodes and the interface between neighboring building blocks. 3) Formation of homo- and heterojunctions. 4) Novel meta-material based architectures within fibers with resonances in the visible and near infrared frequency ranges.

1.5 Objective and outline of the thesis

The objectives of the thesis are described as follows:

- (1) Fabrication of high-performance optoelectronic fiber devices by controlling the phase, grain size, crystallization volume and crystallographic orientation of semiconductors using post-drawing schemes.
- (2) Incorporation of different functional domains into a single fiber for complex functionalities.
- (3) Integration of new metallic elements (metallic glasses) into multi-material fibers, control the microstructure of in-fiber MGs during drawing and demonstration of their unique applications.

The outline of the thesis is listed as follows:

Chapter 1: I first describe the historical background of the advent of the multi-material fibers. The two typical fabrication methods for multi-material fibers, namely thermal drawing and HPCVD are then introduced. In the section of “Applications of multi-material fibers”, I first review the applications of photonic fibers. A PBG in polymer fibers enable omnidirectional reflection and light guidance at 10.6 μm wavelength at high power. The PBG fiber is also useful for creating laser emission in the radial direction from the fiber surface. The semiconductor fibers exploiting internal total reflection extend the accessible wavelength range and opened up a wide range of practical applications. Then, fibers acting as optoelectronic devices are reviewed. These fibers find applications in photo-sensing, thermal sensing, chemical detecting, lensless imaging, digital signal processing and energy harvesting. The work in geometry and structure dependence of fiber performances is also reviewed. The third application is in-fiber synthesis and fabrication. The fiber core is a unique platform for the synthesis of new materials via chemical reaction, nanowires and micro/nanospheres production, formation of novel devices and junctions, fabrication of large single crystals with uniform composition, writing of Bragg and compositional gratings, modifying electronic structure of semiconductors, investigation of classic phase transition mechanisms as well as modification of microstructure of semiconductors for improved optical, electronic and optoelectronic properties. After the literature review, I state the main challenges of the multi-material field. Finally, I describe the objective and the outline of my PhD thesis.

Chapter 2: We investigate the post-drawing furnace-based and laser-based crystallization schemes of an electrically addressed Se core within a multi-material fiber. We demonstrate that the laser-based approach enables a combination of significantly larger grain size and a better control over the crystallization depth, which allows for orders of magnitude better optoelectronic properties, compared to the furnace-based approach. Thanks to the built-in electrodes, we highlight the key role of grain size and crystallization depth via a systematic study of the interplay between the microstructure and optoelectronic properties. In particular, we established a method to extract the crystallization depth via a nondestructive approach. We then demonstrate that laser treatment allowed us to fabricate a fiber device with larger grains and hence less grain boundaries in the direction of the electric field, resulting in significantly better optoelectronic properties. We also show that the laser-based treatment enables not only the precise location of crystallized domains on the fiber cross-section, or potentially also along its axis, but also to control the crystallization depth inside the material. This depth can be engineered to be of the order of magnitude of the photon penetration depth, hence optimizing light collection and charge extraction, while minimizing dark current, resulting in high sensitivity.

Chapter 3: In contrast with the laser-based approach shown in Chapter 2, the newly designed laser-crystallization scheme here allows us to study the effect of laser power, beam size and exposure time on the microstructure formation. In particular, a multi-step annealing enables the formation of a polycrystalline structure with ultra-large grains, controlled crystallization depth as well as preferentially crystallographic orientation. The EBSD and TEM characterization demonstrates that crystals are preferentially oriented with the basal plane of (001) perpendicular to the direction of the electric field. The fiber device in which the semiconductor is crystallographically aligned exhibits highest optoelectronic performances, featuring high photoresponsivity and photosensitivity. Finally, we will propose some possible mechanisms to explain the microstructure formation.

Chapter 4: We demonstrate for the first time the robust and scalable integration of high quality single crystal semiconducting nanowire-based optoelectronic devices at the tip and along the length of polymer optical fibers. We combine the thermal drawing process with a simple sonochemical nanowire growth mechanism applied to amorphous Se domains. Selenium is an excellent optoelectronic material in its trigonal phase and is used in a myriad of applications. As we show experimentally and via first principles density-functional theory calculations, its trigonal structure exhibits an exacerbated anisotropy in the surface energy of the different crystal planes

in the solvent. This allows us to control the phase and orientation of crystalline nanowires that grow along the desired axis in a simple way, directly in intimate contact with built-in electrodes. The resulting nanowire-based photodetecting devices exhibit an unprecedented combination of excellent optical and optoelectronic properties in terms of light absorption, responsivity, sensitivity and response speed. Moreover, thanks to the polymer fiber platform, the nanowires can be positioned anywhere on the fiber cross-section allowing for the integration of complex and unprecedented functionalities. We demonstrate in particular an architecture with two nanowire-based devices positioned around a step-index optical fiber, allowing us to perform fluorescence imaging using a single multi-functional fiber. Finally, our approach also enables the fabrication of nanowire-based devices along an extended length of flexible fibers, without requiring high-resolution contacting techniques, paving the way towards novel opportunities in flexible optoelectronics and advanced textiles.

Chapter 5: We demonstrate for the first time the integration of metallic glasses (MGs) into multi-material fibers. The selection criteria for co-drawing MG with polymers are given. Using MG ribbon as an example, we demonstrate that the thickness of the MG in fibers can be continuously reduced down to tens of nanometers via iterative thermal drawing. TEM characterization indicates all these in-fiber MGs with varying size remains amorphous after thermal drawing. However, the crystallization-induced breakup happens when the thickness of the MG reaches around 40 nm. It is likely that this fragmentation can be circumvented by exploiting the nanoscale size effect in crystallization. We are also able to fabricate more sophisticated fiber architectures, such as MG-rod based fibers, fiber probe with many MG nanowires inside, fiber metamaterial with alternating layers of MG and polymer, and MG hollow core fiber waveguide. More strikingly, the in-fiber MGs with varying size exhibit the same electrical conductivity as that of the bulk material. To highlight the possible application in electrodes, we will then show a nanowire-based optoelectronic fiber in which MGs acting as high-performance electrodes contact with semiconducting nanowires. This simple size-reduction approach also provides a unique platform for making nanoscale MG samples with high geometric perfection, enabling the investigation on the nanoscale size effect in crystallization via in-situ heating in a TEM. Finally, we will model the capillary instability time of the system to explain why the size of MGs can be repeatedly reduced while keeping continuity along the fiber length without break-up.

Chapter 6: Conclusions and outlook

Chapter 2 Polycrystalline Semiconductor-based Optoelectronic Fibers

In this chapter, I will first describe the fiber materials, the fiber design and the fiber fabrication methods. Then I will show two different approaches for inducing the crystallization of the amorphous semiconductor in the as-drawn optoelectronic fibers. The crystallization methods, structure characterization via SEM, XRD, DSC, EBSD and TEM techniques as well as optoelectronic properties of the devices will be described in detail. After critically analyzing and comparing the two approaches for tailoring the microstructure of in-fiber semiconductor, I will finally discuss the potential applications of these annealed fibers.

2.1 Fiber Fabrication and Characterization

The materials used to make the fiber are polysulfone (PSU) (cladding), conducting carbon-loaded polycarbonate (CPC) and $\text{Sn}_{91}\text{Zn}_9$ (electrodes), and selenium (Se) (semiconductor). In Fig. 2.1a we show the glass transition temperature (T_g) of the two polymers and the melting point (T_m) of Se obtained from Differential Scanning Calorimetry (DSC) 8000 Perkin Elmer measurement. Amorphous PSU and CPC are thermoplastic polymers and can be pulled into fibers above their T_g . The fiber in this chapter was fabricated by the thermal drawing approach. In brief, in a slab we cut out two grooves where CPC and $\text{Sn}_{91}\text{Zn}_9$ electrodes were positioned. Between these two PSU slabs we introduce a thinner one that encapsulates a Se plate. In this way, the Se and $\text{Sn}_{91}\text{Zn}_9$ electrodes are completely encapsulated between the PSU and the CPC, preventing any leakage of molten Se and $\text{Sn}_{91}\text{Zn}_9$ during thermal drawing. Subsequently, the stack was consolidated in vacuum at 215 °C for 30 minutes. The composite structure was then drawn at 285 °C, a temperature above the T_g of PSU and CPC and T_m of Se, in a custom designed draw tower, into a fiber more than 100 m in length[59]. This shows the compatibility of these different materials for thermal co-drawing.

The schematic of the preform to fiber device of the structure described above is shown in Fig. 2.1b. The Se semiconductor core is in intimate contact with the CPC nanocomposite electrodes. The $\text{Sn}_{91}\text{Zn}_9$ eutectic alloy in contact with CPC ensures a good axial conductivity and a straightforward electrical contact to external circuits. The transparent PSU cladding ensures a good encapsulation and mechanical support of the whole assembly. Fig. 2.1c illustrates the scalability of the process where hundreds of meters of flexible and functional light-weight fibers are produced in a single draw. The optical photograph of the fiber cross-section shows that the

rectangular Se domain is sandwiched between CPC electrodes, with shape and aspect ratio unchanged from those of the preform (Fig. 2.1d). The differential scanning calorimetry (DSC) and the diffuse ring diffraction pattern of the selected-area electron diffraction (SAED) from TEM characterization on the Se harvested from the as-drawn fiber indicate that Se is amorphous after drawing (Fig. 2.1e and f). The crystallization temperature is higher than that in the literature[63], which may be due to stress-induced enhancement of the thermal stability of amorphous Se[64].

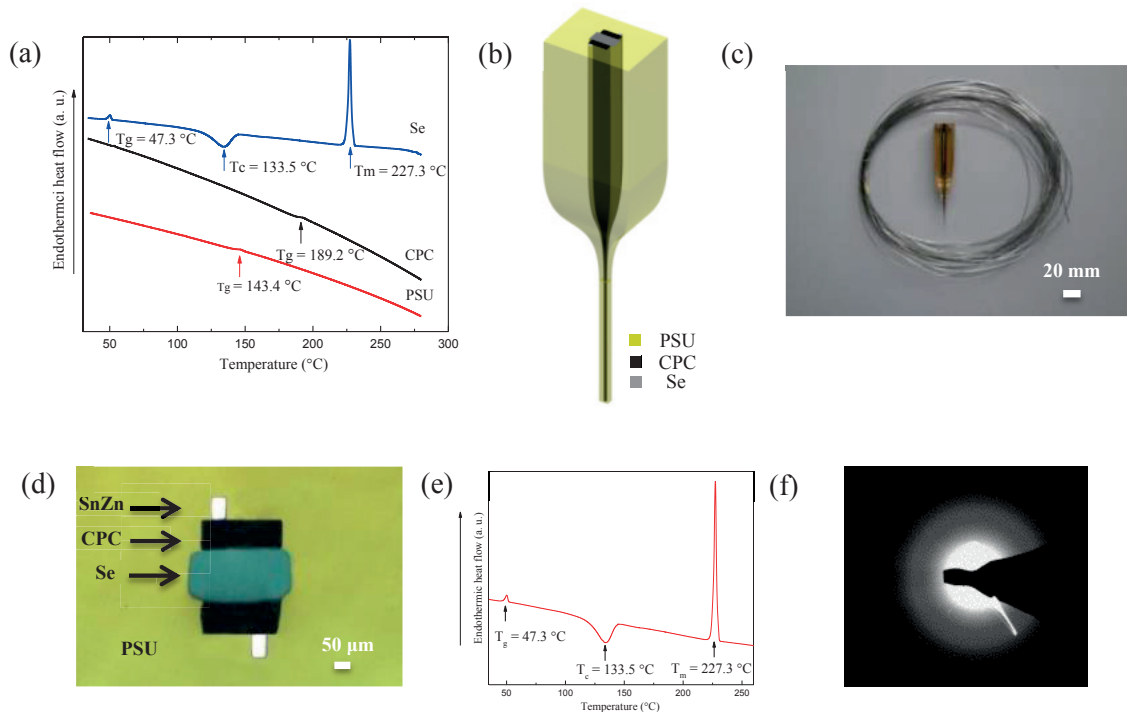


Fig. 2.1 (a) DSC curves of Se, CPC and PSU; (b) Schematic of the fiber drawing process; (c) Photograph of the preform and of drawn fibers of tens of meters showing their robustness and flexibility; (d) Optical photograph of the cross-section of the as-drawn fiber; (e) DSC (heating rate of 10K/min) curve of the Se in the as-drawn fiber; (f) SAED of the Se in the as-drawn fiber.

2.2 Furnace-induced crystallization and characterization

The electrical and optoelectronic properties of an amorphous material are poor due to the disordered structure and abundant defects in the material that result in short carrier lifetime, low carrier mobility and short carrier diffusion length. Even though the carrier density in amorphous Se is increased when the material is under illumination, the abundant defects acting as recombination centers still severely impair charge carrier drift, resulting in a small photocurrent.

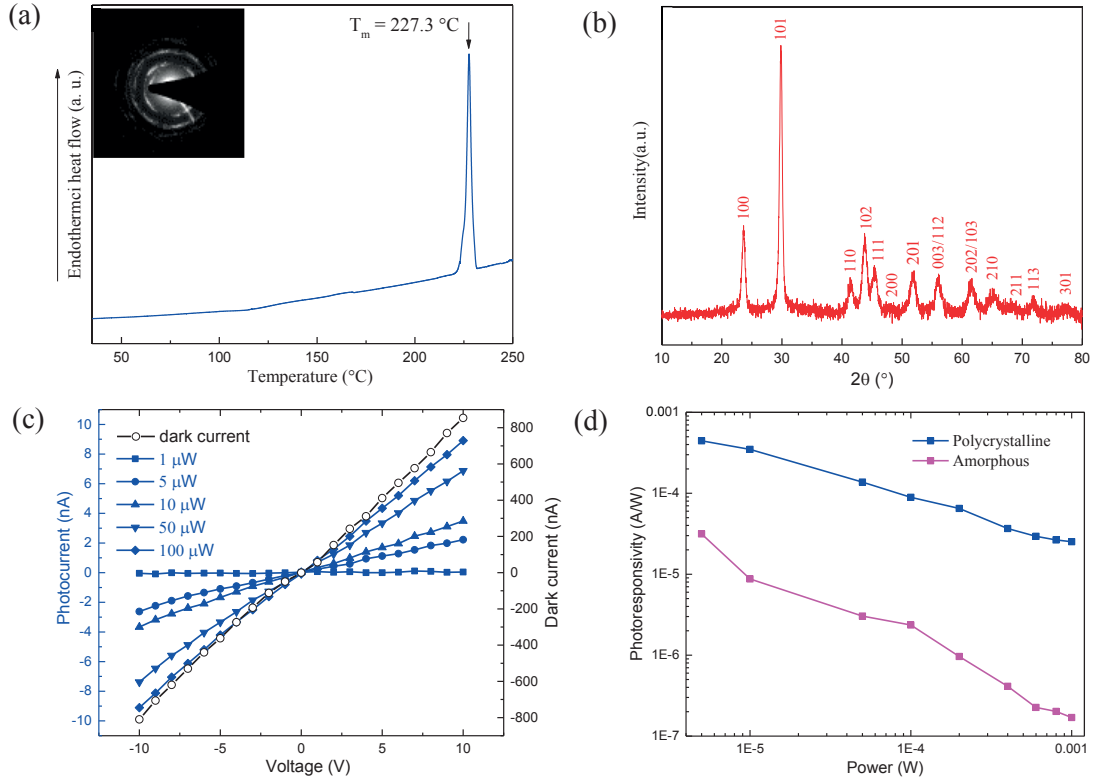


Fig. 2.2 DSC (heating rate of 10K/min) curve and the insert SAED of Se heated on a hot plate; (b) X-ray diffraction of the annealed Se; (c) I-V curves of the device versus light power at $\lambda = 532$ nm; (d) Photoresponsivity of the device versus light power at $\lambda = 532$ nm and the bias of 10 V.

In order to improve the performance of the device, we first subjected the amorphous Se embedded in the fiber to an annealing treatment. To facilitate the characterization of the resulting microstructure, we induced and investigated the crystallization at the fiber tip rather than along the fiber through the cladding. We established a protocol where we heat up the tip of the fiber by placing it vertically on a hot plate at 150 °C, above the crystallization temperature, for 5 minutes. The DSC, SAED as well as X-ray diffraction characterizations on the Se in the annealed fiber prove that Se becomes polycrystalline, as indicated in Fig. 2. 2a and 2. 2b). The SAED and X-ray diffraction can be indexed as the trigonal phase. We then characterized the optoelectronic properties of the annealed fiber by measuring the photocurrent of the device at a bias between -10 and 10 V, under different illumination powers. The linear form of the I-V curve in Fig. 2. 2c reveals a good Ohmic contact between the crystalline Se and the CPC electrodes. The photocurrent (= illuminated current – dark current) at a given voltage is raised by increasing the power of the incident light, as it increases the number of photo-generated carriers. The

photoresponsivity of the annealed fiber device is two to three orders of magnitude higher than the as-drawn fiber in which Se is amorphous, for a wide range of incident powers (Fig. 2. 2 d). However, compared to the dark current, the photocurrent of the in-fiber device remains rather small, as shown in Fig. 2. 2c). Such a large dark current implies a large crystallization depth along the fiber axis which increases the area over which the current density is integrated. A large dark current leads to a low photo-sensitivity ($I_{\text{photocurrent}}/I_{\text{dark}}$) and high noise current of the device.

To assess the region over which crystallization has occurred, we developed a non-destructive method that relies on the local photo-response of the in-fiber device. As the fiber tip is placed on the hot plate, heat diffuses and a temperature gradient is generated along the fiber axis. The Se domain at the fiber tip was heated at a higher temperature ($\sim 150^\circ\text{C}$) compared to the Se domain away from the tip. We assume Se became fully crystalline at the fiber tip and then partially crystalline in the region away from the hot plate. The different photoconductivity of the amorphous and annealed Se domains allows us to extract the crystallization depth of Se along the fiber axis, as we scan it with a laser beam this time along the fiber length. Indeed, thanks to the transparency of PSU cladding, photons can reach the Se core when the fiber is illuminated from its side between the CPC electrodes. The photocurrent generated was then recorded as the laser beam of 3 mm in diameter (CPS532 Laser Diode, Thorlabs. The wavelength is 532 nm and the power is 4.81 mW) was scanning the fiber along its axis with steps of 100 micrometers (minimum step size). Fig. 2.3a shows a schematic of the process, and in Fig. 2.3b we plotted the current versus the position of the right edge of the laser beam (i.e. at 0 mm the beam does not cover the fiber). We can then divide the current measurement in different stages: in stage I, the current increases linearly as the beam illuminates an increasing length of the fully crystallized Se that has the same photo-conductivity. At around 0.9 mm the slope changes because the beam now also illuminates a partially crystallized region, with a lower photoconductivity. As the beam progresses further, the crystalline volume fraction of the partially crystalline part becomes smaller when the position is further away from the fiber tip, leading to a reduced increase rate of current in stage II. Once all the crystalline part is illuminated, the current reaches a maximum. As we continue scanning, the current remains roughly stable in stage III when the amorphous part is being illuminated, as it contributes a very small photocurrent. Subsequently, the current decreases linearly because the fully crystalline part starts to move outside of the beam, as shown in stage IV. The current then reduces with a rate similar to stage I until all the partially crystalline part moves out of the beam (stage V), corresponding to a similar width of fully crystalline part of around 0.9

mm. Finally, the current keeps the same low value when only an amorphous domain intercepts with the beam (stage VI). We can use this curve to extract the length of fully and partially crystalline parts. They correspond to 0.9 mm and 1.3 mm, respectively, for the particular heat treatment performed. The axial length of the amorphous domain in the beam in stage III can be estimated to be 0.7 mm. The total length of the fiber in the beam at the end of stage III is therefore 2.9 mm that matches with the effective beam size of the laser[59].

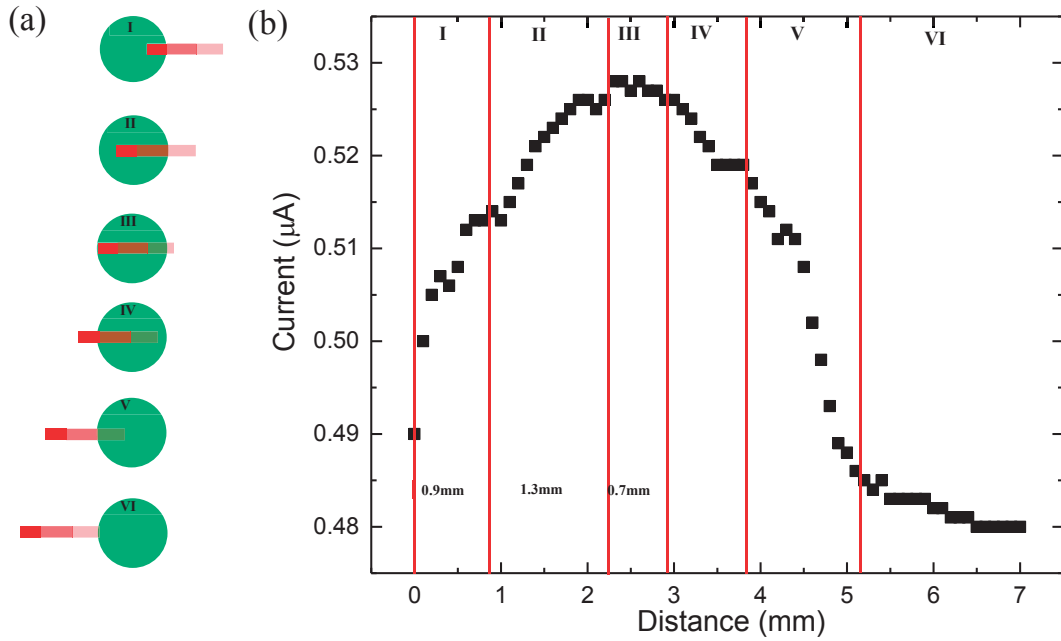


Fig. 2. 3. (a) The schematic of the fiber advancing into the laser beam. The green dot represents the laser beam while the fiber is depicted in red. The dark red is the fully crystallized part (left). The lighter red in the middle represents the partially crystallized section, and the light pink part is the area that remained amorphous; (b) Photocurrent versus the length of the fiber irradiated by the laser beam, as the beam scans the fiber from left to right. The voltage was set to 6 V.

It should be noted that the laser source (CPS532 Laser Diode, Thorlabs) has a built-in collimated system which provides a good uniformity across the 3 mm beam. Even though the photon intensity is not perfectly uniform, the slope of the curve in Stage II when the partially crystalline Se was moved into the beam and the fully crystalline Se was moved towards the center of the beam still decreases. This shows that the decreased current due to the decreased crystalline volume fraction is more significant than the increased current coming from the slightly increased photon intensity. Given the sensitivity of the fiber and the beam profile, the change of

slope that characterizes the transition (indeed blurry) between the fully crystalline and partially crystalline regions can be clearly observed. The resolution can be improved by using a laser beam with uniform photon distribution and small scanning step size.

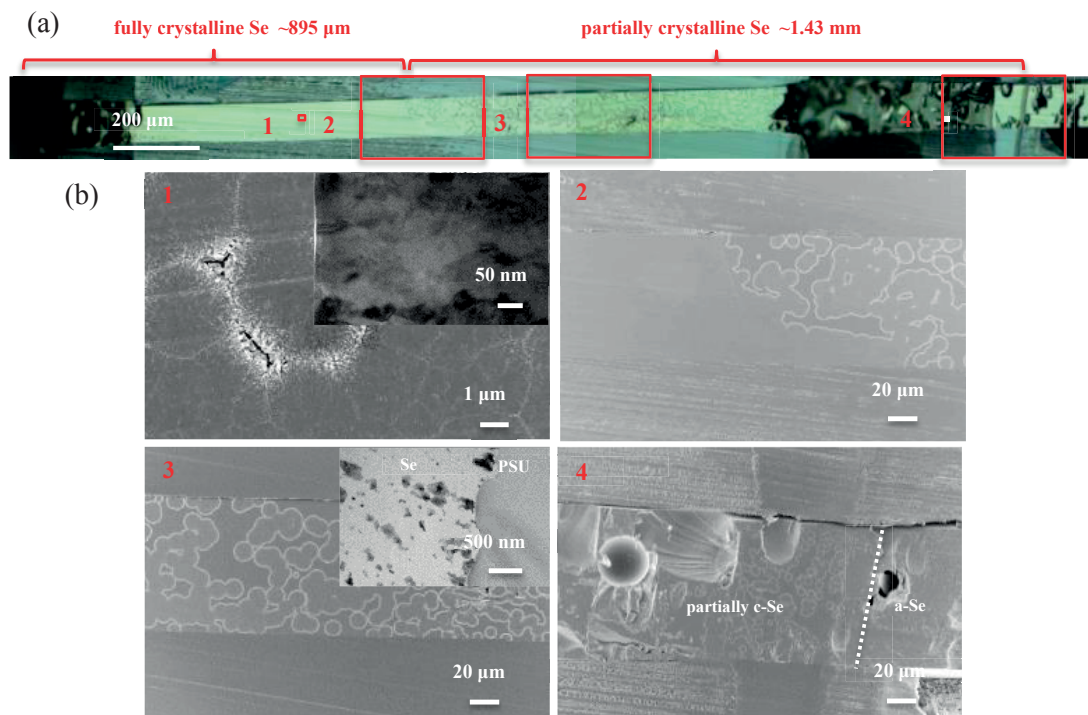


Fig. 2.4. (a) Optical photograph of the longitudinal section of the fiber; (b) SEM micrographs of the regions 1 to 4 in (a). The inserts in Fig. 2.4b-1 and Fig. 2.4b-3 are right field TEM images.

To validate this indirect and non-destructive approach, the fiber was cut in the longitudinal direction by ultramicrotomy. The optical photograph of the longitudinal section of the fiber is shown in Fig. 2.4a. The left and right edges of the sample are not smooth because the force applied on the diamond knife was only uniform in the center of the blade but not on the sides. It is apparent that the crystalline region consists of fully and partially crystalline regions. The SEM image of region 1 (see Fig. 4a) reveals the Se is fully crystalline with the typical spherulite microstructure (composed of many crystals) of crystalline Se (Fig. 2.4b-1). The insert bright field TEM image further demonstrates the crystallinity and indicates the grain size of Se in this region is around 100 nm. Fig. 2.4b-2 and b-3 show the SEM images of region 2 made of both fully and partially crystalline parts, and region 3—partially crystalline part, respectively. The insert bright field TEM image in Fig. 2.4b-3 of the Se in this region indicates Se is partially crystalline and the grain size is tens of nanometers. Region 4 is far away from the fiber tip and the SEM image (Fig.

2.4b-4) shows that Se on the right in this region remains amorphous. We indicated that the Se on the right of the dash line in Fig. 2.4b-4 is amorphous because no spherulite structure was observed in the SEM image. It is difficult to obtain a smooth cut via ultramicrotomy over such a wide length and the part in the amorphous region remains rough. No crystalline feature was observed however beyond the indicated dash line. The grain size of Se in this work agrees well with that of crystalline Se fabricated by a similar approach[65][66]. From this SEM analysis we can extract the lengths of the fully and partially crystalline Se to be 0.89 and 1.43 mm, respectively. This matches well with the values of 0.9 mm and 1.3 mm obtained from the previously described non-destructive method.

2.3 Laser-induced crystallization and characterization

The polycrystalline Se with nanoscale grain size after annealing exhibits an extremely large number of grain boundaries. These grain boundaries can act as charge carrier recombination centers which are detrimental to the electronic and optoelectronic properties of the material[67][68]. To improve the responsivity of the device, a better control over the microstructure with larger grains and potentially single crystal domains between the electrodes is required. For a good device sensitivity, it is also important that the dark current and associated noise be minimal. Ideally, the crystallization depth would be just enough to absorb as much light as possible, that is the order of the penetration depth of the wavelength considered. Beyond this depth, crystalline domains would only participate to noise, which is detrimental to the sensitivity. In other words, the photocurrent remains the same while the dark current can be significantly reduced if the crystallization depth can be controlled to be of the order of the photon penetration depth, giving rise to a high responsivity and sensitivity[28]. Regardless of the temperature and time of annealing, we have observed that the resulting crystallization domains have a microstructure with rather small grains, and a depth hard to control and of the order of several tens of micrometers. We therefore turned to a laser-based approach to induce crystallization, used for Si or Ge materials, but never for Se-rich semiconductors.

The fiber cross-section was illuminated by a laser beam ($\lambda = 490$ nm) with a power of 1.5 mW and a diameter of 160 μm for up to 3 hours. The schematic in Fig. 2.5a shows the annealing scenario. We chose these parameters as they result in a drastically better control over microstructure and performance compared to the furnace-based crystallization scheme described above, highlighting the comparison between the two methods. An in-depth report of the influence

of these various parameters on the resulting microstructure and optoelectronic properties is beyond the scope of the current study. The cross sectional optical photograph in Fig. 2.5b shows that the Se region illuminated by the laser beam is crystalline with many grains, while the region outside the beam remains amorphous. The microstructure was further investigated by EBSD. The corresponding EBSD map of the crystalline Se is shown in Fig. 2.5c, displaying a polycrystalline structure consistent with the optical microscope imaging. The histogram in Fig. 2.5d indicates an average grain size of 4.5 μm in the cross-section that is orders of magnitude larger than the grain size of Se crystallized with the furnace-based approach described above. Fig. 2.5e shows the setting of the reference frame for pole figures in Fig. 2.5f. The projection of pole Z0 is at the center of the reference plane, and X0 and Y0 is on the periphery of the projection. The orientation of basal plane of $\{0001\}$ is parallel to the fiber axis while some of the prismatic planes of $\{10\text{-}10\}$ preferentially orientate perpendicular to the fiber axis.

In order to study the crystallization depth and microstructure along the fiber axis, we used a combination of TEM and electron diffraction technique. We prepared TEM lamella cut out of the fiber in the longitudinal direction with ultramicrotomy, as previously described. The bright field TEM in Fig. 2.6-1 reveals that the crystallization depth is 450 nm at the edge and 700 nm in the center of the crystalline region, which can be explained by the Gaussian-like wave-front of the laser beam. The SAED pattern (Fig. 2.6-2) taken from region A of Fig. 2.6-1 clearly shows a polycrystalline structure with different orientations and the clustered diffraction spots suggest that the grain boundaries are mostly low-angle type; Region B on the other hand only contains a few grains, as indicated by the bright field TEM image in Fig. 2.6-3. Indeed, the SAED pattern taken from region C of Fig. 2.6b-3 shows a large single crystal (Fig. 2.6-4). Using an objective aperture in the back focal plane to collect the diffracted electrons that contribute to the spots of the SAED pattern, as shown by the squares in Fig. 2.6-2, dark field TEM images, formed by diffracted beam 1 to 4, are taken in Fig. 2.6-5-8 which allow us to study the grain size and morphology. It can be seen that the grain size is a few hundreds of nanometers in the fiber axis direction, and the morphology of each grain is irregular. We hence could achieve a microstructure with grains that are large in the direction perpendicular to the electrodes, which reduces the number of grain boundaries, and small in the fiber axis direction, reducing the dark current.

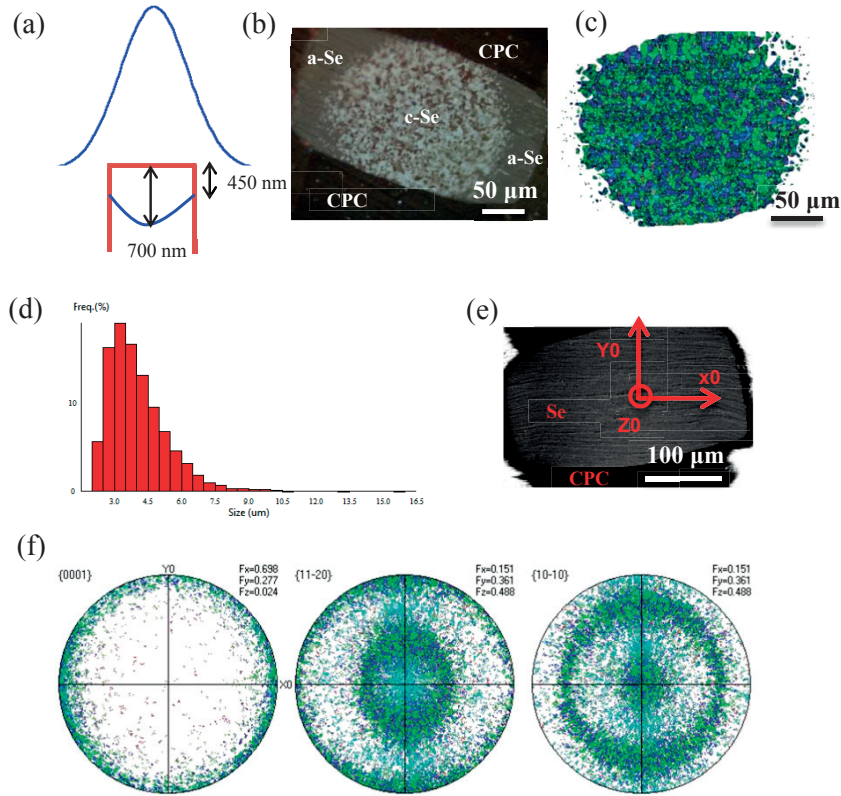


Fig. 2.5. (a) Schematic of laser annealing scenario. The laser beam is described in a Gaussian distribution. The crystallization depth of Se along the fiber axis is also indicated; (b) Cross sectional optical photograph of the fiber heated with laser; (c) The corresponding EBSD map on the crystalline Se in (b) (Here we have chosen a IPFz representation which encodes the angle between the crystallographic c-axis and sample Z-axis (the green and blue colors mean that the c-axis is at 90° with respect to the Z axis, the grains orientates at 0° would be in red, but there are no such grains in the sample)); (d) The histogram of grain size distribution; (e) The reference frame of X0, Y0 and Z0. The projection of pole X0 is at the center of the reference plane, and Y0 and Z0 is on the periphery of the projection; (f) Pole figures of basal plane {0001} and prismatic planes {11-20} and {10-10}.

Such an optimized microstructure with a very small crystallization depth and big grains in the cross-section perpendicular to the electrodes is expected to exhibit improved performances. We then characterized the optoelectronic properties of the device by measuring the current under different powers and at fixed wavelength ($\lambda = 532$ nm), as previously done. In Fig. 2.7 the

photoresponsivity and the ratio I_{ph}/I_{dark} were measured at a bias of 10 V as a function of power, for the two different devices annealed by the hot-plate and the laser. As we anticipated, the fiber crystallized with the laser-based approach exhibits a much higher photoresponsivity in a wide range of powers. The ratio I_{ph}/I_{dark} of the fiber crystallized with the laser beam is several orders of magnitude higher, compared with the fiber crystallized with hot plate. These performances are excellent and compare favorably with reported trigonal Se microtube planar photodetector[69].

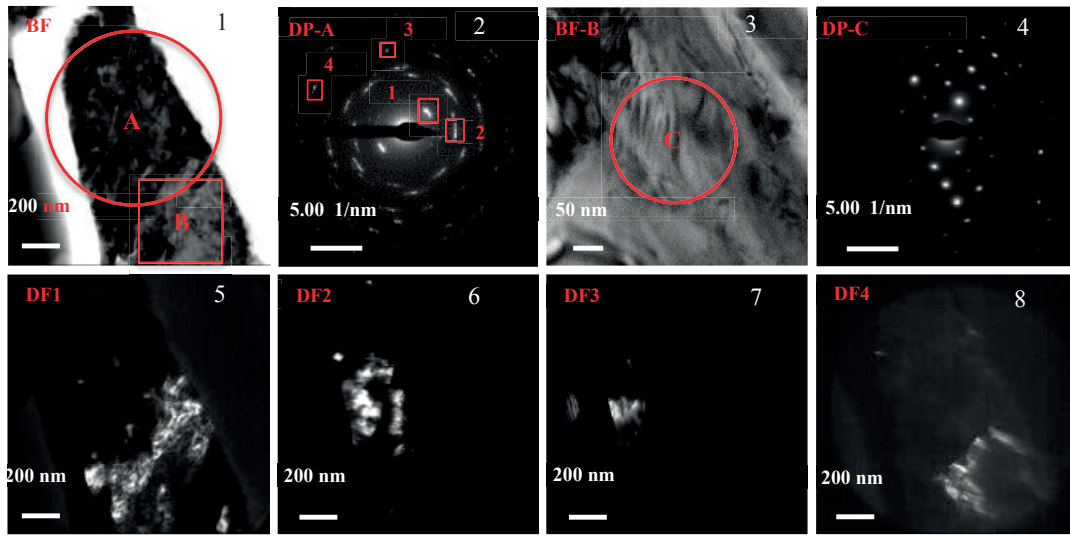


Fig. 2.6. TEM micrographs and SAED patterns of the crystalline Se in the longitudinal section;

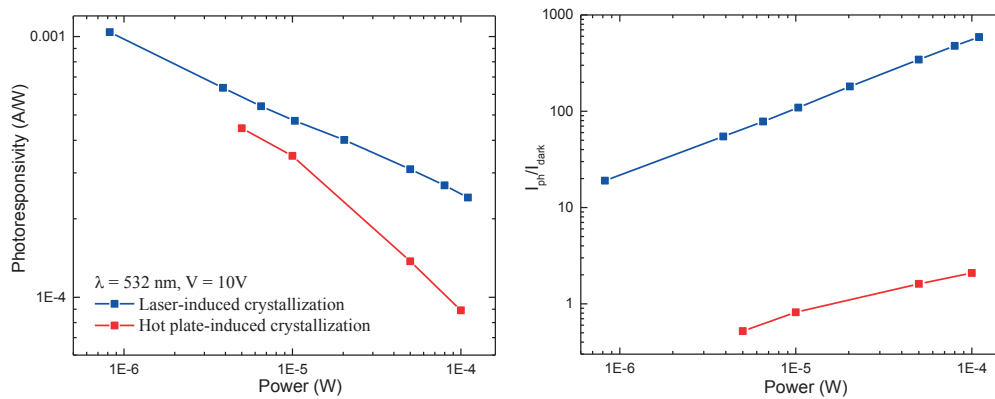


Fig. 2.7 Left: comparison of photoresponsivity of laser-induced crystallization fiber and hot plate-induced crystallization fiber. Right: ratio of I_{ph}/I_{dark} versus power for the same fibers.

2.4 Discussion and summary

In this chapter, we used two different thermal annealing approaches, namely furnace-based and laser-based heat treatment to induce crystallization of amorphous Se core within a multi-material fiber. All the crystallization treatment was performed at the fiber cross-section, which facilitates the characterization of the resulting microstructure, compared to crystallization along the fiber through the cladding. Regarding the furnace-based approach, it was very hard to control the heat distribution, as heat can diffuse over a large distance. This leads to a large crystallization depth along the fiber axis. The annealing temperature was set at 150 °C that is around 50 °C higher than the crystallization temperature of amorphous Se. Such a high temperature may induce the formation of a large number of nuclei and subsequent crystal growth. Regardless of temperature and time, the regular annealing-based method induces a microstructure with nanoscale grains and a large and hard to control crystallization depth. The laser based approach however is able to accurately deliver high-density energy into a confined region of a material. Heat generation during the laser treatment was therefore only limited to a very small depth that is comparable to the photon penetration depth (a few micron), hence optimizing light collection and charge extraction, while minimizing dark current, resulting in high sensitivity. Further work is underway for the systematic study of the effect of laser power, beam size and exposure time on the microstructure formation. Thanks to the built-in electrodes, we also highlight the key role of grain size and crystallization depth via a systematic study of the interplay between the microstructure and optoelectronic properties. In particular, we established a method to extract the crystallization depth via a nondestructive approach. The in-depth understanding of the interplay between the materials microstructure and device performance could open new opportunities for increasingly sophisticated functionalities in fiber devices. Optoelectronic fibers with a functionalized tip can find several applications in highly sensitive remote detection and sensing, optoelectronic probes, minimally invasive in situ and in vivo bio-compatible probing and imaging of biological tissues. The small cross-section and large aspect ratio of the high-performance fiber indeed allows access to remote and confined environments where rigid and planar point photodetector is unable to reach. The laser annealing approach demonstrated here also has the potential to be applied in the longitudinal direction of the fiber by focusing the beam on the active material through the cladding. This would enable the ability to write, at any location along kilometer-long fibers, devices of controlled microstructure and performance. Possible applications can be envisioned in large area, flexible optoelectronics, energy harvesting systems, and advanced fibers and textiles.

2.5 Experimental methods

All the scanning electron microscopy (SEM) samples were coated with 10 nm carbon film. The SEM images were taken with the Zeiss Merlin field emission SEM (Zeiss, Göttingen, Germany) equipped with a GEMINI II column operating at 2.0 kV with a probe current 150 pA. The In-Lens annular detector allowed for high resolution secondary electrons imaging at all magnifications. Transmission electron microscope (TEM) samples were prepared by embedding them in epoxy resin followed by sectioning thin slices (60 nm) using ultramicrotomy (diamond grade) which were transferred on a carbon/Cu grid supports (300 Mesh). The TEM images and selected area electron diffraction (SAED) were taken using talos F200X operating at 200 kV. For the samples subject to differential scanning calorimetry (DSC) and X-ray diffraction characterizations, a ~0.9 mm part from the fiber tip was cut before the surrounding materials—PSU, metal and CPC were dissolved away by N, N-dimethylacetamide. The harvested bulk Se was then grinded into powders for the DSC and XRD characterization. In order to have enough signals, we collected the fully crystalline part from many fiber tips. All the DSC curves were taken using DSC 8000 from Perkin Elmer. The Electron BackScatter Diffraction (EBSD) maps were acquired at 20 kV on a FEG-SEM XLF30 (FEI) equipped with a Nordlys II camera; they were treated with the Aztec software (Oxford Instruments).

To only crystallize the fiber tip, the fiber was placed perpendicularly with respect to the heat source of the hot plate and the laser beam during the annealing processes. The electrical and photoresponse characteristics were measured using a Keithley 6517B under dark and illuminated conditions. The SuperK Extreme from NKT Photonics, with tunable wavelengths between 410 and 830 nm was used as the light sources. The optical laser power was adjusted using an afocal lens system and was measured using a laser power meter (Thorlabs PM 100D). The laser beam used to characterize the optoelectronic properties of the devices was incoming perpendicularly to the fiber cross-section (hence parallel to the fiber axis). The beam size was set to be the same as the size of the larger side of the rectangular Se domain in the fiber cross-section. All measurements were performed in air and at room temperature.

Chapter 3 Controlling the Crystallographic Orientation of Semiconductors in Optoelectronic Fibers

In this chapter, I will introduce the systematic study of laser-induced crystallization on the semiconductor in optoelectronic fibers. In contrast with the laser-based approach shown in chapter 2, the newly designed scheme here allows us to study the effect of laser power, beam size and exposure time on the microstructure formation. I will first show the fiber architecture designed for this work. Subsequently, after studying the effect of laser power and exposure time on the grain size, crystallographic orientation and the optoelectronic performances, I will propose a novel annealing scheme to induce crystallization. The EBSD and TEM characterization demonstrates that crystals are preferentially oriented with the basal plane of (0001) perpendicular to the direction of the electric field. The fiber device in which the semiconductor is crystallographically aligned exhibits highest optoelectronic performances, featuring high photoresponsivity and photosensitivity. Finally, I will propose some possible mechanisms to explain the microstructure formation.

3.1 Fiber Fabrication and Characterization

The size of the semiconductor Se in the fiber (refer to as “precursor fiber”) in Chapter 2 is so large that it requires a laser with high power and long illumination time to induce crystallization. A small semiconducting region in the fiber would allow the heat to diffuse rapidly and efficiently. In addition, charge carriers generated in the semiconductor would have fewer possibilities to be trapped by the defects, for example grain boundaries in a miniature domain during their transport. A straightforward way to reduce the size of the semiconductor in the fiber is to redraw the fiber. The fiber was fabricated via thermal drawing of a cylindrical preform, as schematically shown in Fig. 3.1a. In brief, a hollow PSU tube with surrounding CPC electrodes was wrapped around PSU films via the thin film rolling technique. The assembly was then consolidated in vacuum at 270 °C for 30 minutes. Two pockets were cut to place the precursor fibers. More PSU films were wrapped around the structure to protect the inner part of the preform before a second consolidation was performed. A similar procedure was applied to the preform to add the SnZn electrodes. Finally, the preform was drawn into tens of meters of fibers at 270 °C. The optical micrograph of the fiber cross-section (Fig. 3.1b-middle) shows that the fiber preserves the original cross-section of the preform, but the distance between two CPC electrodes in the fiber has been reduced to $\sim 15\ \mu\text{m}$ (zoom-in optical micrographs in Fig. 3.1b) from $\sim 150\ \mu\text{m}$ of the

electrode distance in the precursor fiber. The Se intimately interfaces with CPC electrodes. Electron microscopy characterization indicates that the Se in the as-drawn fiber exhibits an amorphous structure (Fig. 4.10, Chapter 4).

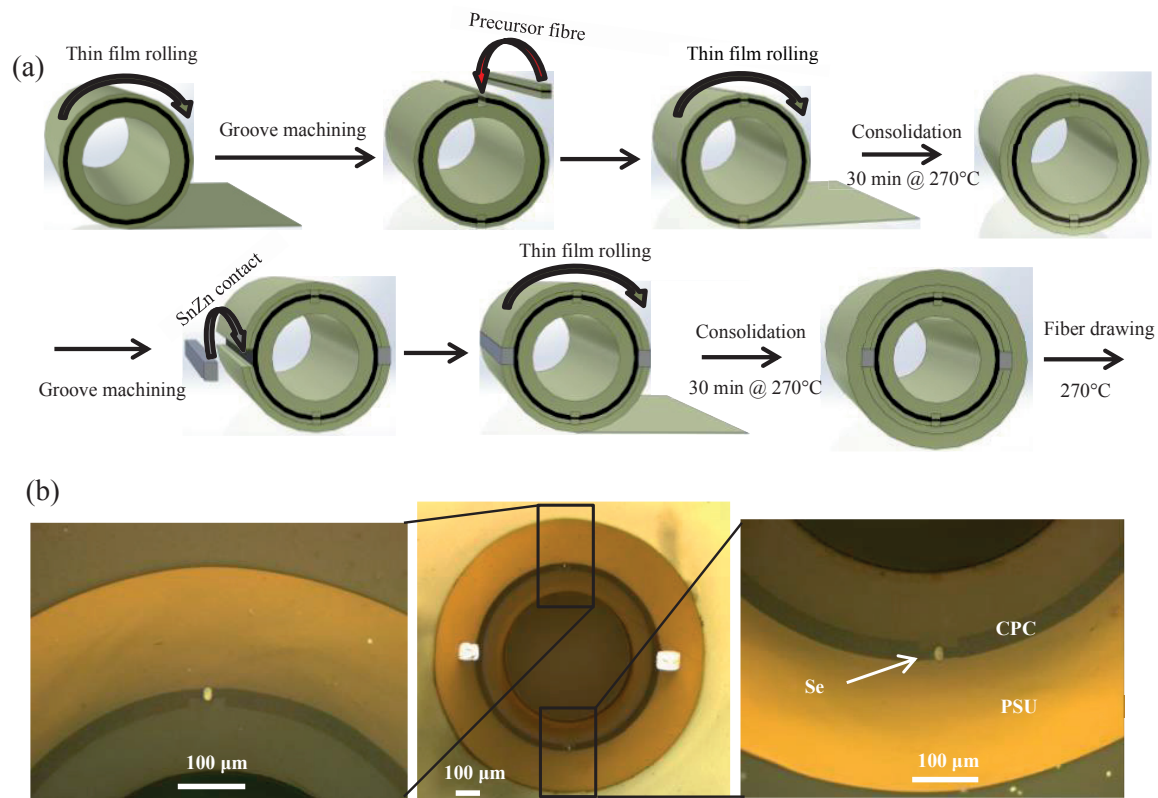


Fig. 3.1. (a) Fabrication steps of making the fiber; (b) middle: optical micrograph of the fiber cross-section; left and right: zoom-in optical micrographs of the two Se regions.

3.2 Crystallization strategy, crystallographic and performance characterization

The fiber tip was first polished with a mechanical approach using increasingly fine SiC papers (down to 4000 grade) before it was treated with the laser beam ($\lambda = 532$ nm). The fiber was placed perpendicularly with respect to the laser beam during the annealing processes. The beam size was around 30 μm, so that it could cover the whole Se region. The power of the laser was set at 600 μW. The whole process is shown in Fig. 3.2a. The fiber (refer to as fiber No1) was first kept in the dark environment for a while until the dark current reached a stable value. Subsequently, the laser was switched on to anneal the amorphous Se. The current thus increases slightly under this illumination due to an increased number of photon-induced charge carriers in the material. When the Se region is illuminated for longer time, the heat generated by photon

absorption will induce the formation of crystals in the amorphous matrix. This would improve the electrical conductivity of the material. Thus the current starts to increase slowly from the 50th s onwards. At the 100th s, the current begins to increase abruptly because the whole amorphous matrix starts to transform into crystalline phase. The laser beam is turned off when the current reaches 300 nA. The current immediately goes down and stabilizes at 0.41 nA that is slightly higher than the dark current (0.11 nA) before the fiber was treated with the laser beam.

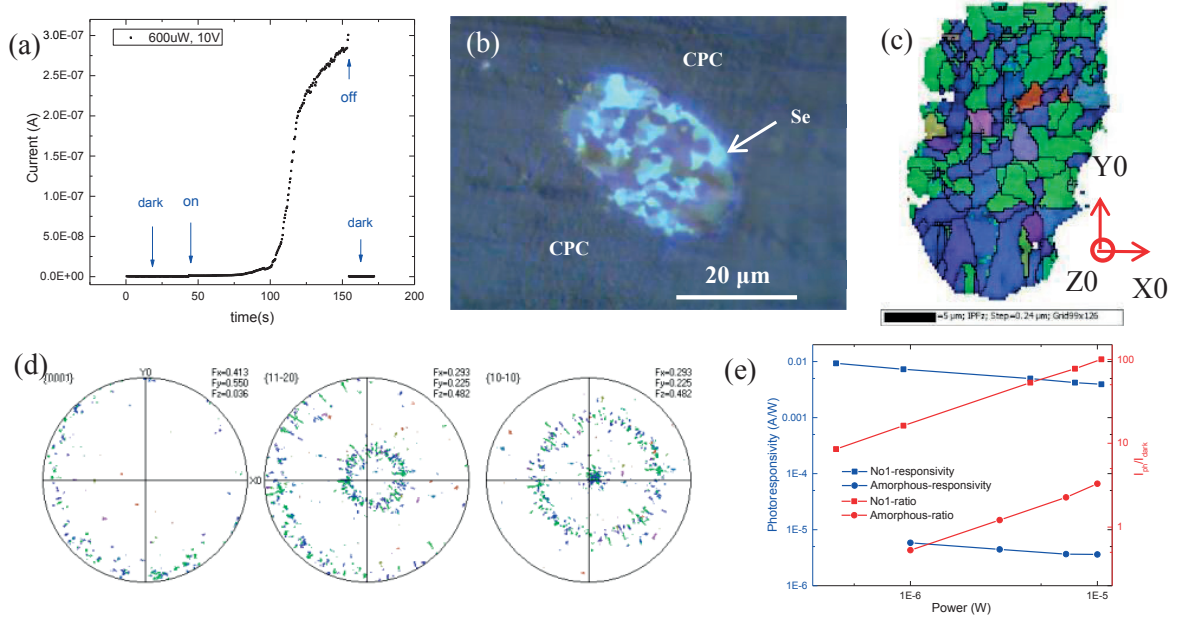


Fig. 3.2. (a) Annealing process for sample No1; (b) Optical micrograph of the fiber cross-section after the laser treatment; (c) The corresponding EBSD map on the crystalline Se in (b). The reference frames for the pole figure are indicated here. (d) Pole figures of the direction normal to the basal plane {0001} and the direction normal to prismatic planes {11-20} and {10-10}; (e) Comparison of photoresponsivity and I_{ph}/I_{dark} ratio of the as-drawn fiber and the annealed fiber as a function of power of the illumination.

The cross sectional optical micrograph in Fig. 3.2b shows that the Se region illuminated by the laser beam is crystalline with many grains. The different colors shown in different grains in the micrograph indicates that grains with different crystallographic orientation reflect light differently. The corresponding EBSD map of the crystalline Se is shown in Fig. 3.2c, displaying a polycrystalline structure consistent with the optical microscope imaging. The size of these grains is below 5 μm. The insert in Fig. 3.2c shows the setting of the reference frame for pole figures in

Fig. 3.2d. The X0 is normal to the CPC electrodes plane while the Z0 is parallel to the fiber axis. Therefore, the projection of pole Z0 is at the center of the reference plane, and X0 and Y0 is on the periphery of the projection. As shown from the pole figures (Fig. 3.2d), the orientation of basal planes {0001} is parallel to the fiber axis while some prismatic planes {10-10} preferentially orientate perpendicular to the fiber axis. It should be noted that the fiber tip was not polished after laser treatment for optical microscopy and EBSD characterization.

The optoelectronic properties of the fiber device obtained by measuring the current under illumination with different powers at a fixed wavelength ($\lambda = 532$ nm) is shown in Fig. 3.2e. Both the photoresponsivity and the photosensitivity (I_{ph}/I_{dark}) of the annealed fiber are improved by several orders of magnitude, compared to the as-drawn fiber in which Se remains amorphous. In addition, the annealed fiber is very sensitive to a weak power down to a few hundred nW while the as-drawn fiber can only sense light when the power is above 1 μ W.

The optoelectronic properties of the device would be enhanced if the density of grain boundaries in the polycrystalline domain could be reduced. Since the crystal growth rate depends strongly on temperature, we then exploited a laser beam with higher power to anneal the second fiber sample (refer to as sample No2). The power was increased to 1 mW. The whole treatment process is very similar as that of sample No1, as shown in Fig. 3.3a. The cross sectional optical micrograph shows that the amorphous Se becomes crystalline with many grains (Fig. 3.3b). The corresponding EBSD map of the crystalline Se displays a polycrystalline structure consistent with the optical microscope imaging (Fig. 3.3c) and the average grain size is bigger than that of sample No1. The crystallographic orientation (Fig. 3.3d) obtained from EBSD characterization is the same as that of sample No1, namely the orientation of basal planes {0001} is parallel to the fiber axis while some prismatic planes {10-10} preferentially orientate perpendicular to the fiber axis. The annealing time for sample No2 is around 104 s. A longer growth time would potentially allow a crystal to grow bigger. We hence prolong the annealing time to 172 s (Fig. 3.4a) for the next sample (refer to as sample No3). The optical micrograph and EBSD mapping show the grain size increases slightly (Fig. 3.4b and c), compared to the sample No2. The orientation of basal planes {0001} is parallel to the fiber axis, and some prismatic planes {10-10} preferentially orientate perpendicular to the fiber axis. A longer annealing time would also increase the crystallization volume that determines the dark current of the device, even though it can enlarge the grain size in the polycrystalline domain. Fig. 3.5a compares the dark current of the as-drawn

sample before the laser annealing and sample No1, 2, and 3 after the laser treatment. As we expected, sample No2 treated with a higher power

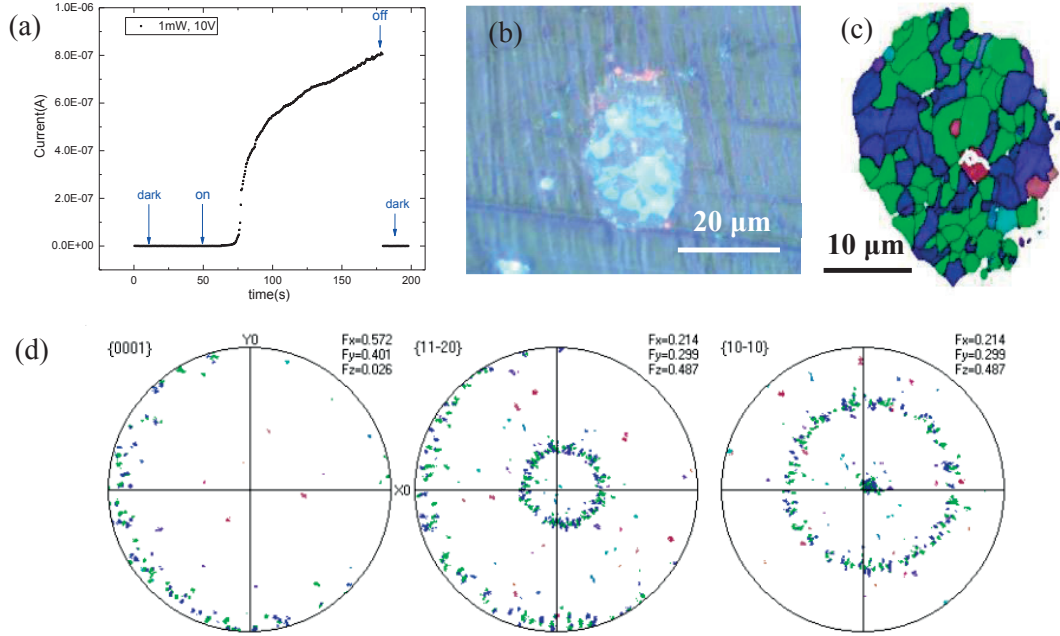


Fig. 3.3 (a) Annealing process for sample No2; (b) Optical micrograph of the cross-section of the annealed fiber; (c) The corresponding EBSD map on the crystalline Se in (b); (d) Pole figures of the directions normal to {0001}, {11-20} and {10-10} planes.

exhibits a higher dark current compared to sample No1 treated with a lower power, though the annealing time for No2 is a few seconds less than that of No1. Sample No3 treated with a higher power and longer time gives rise to the highest dark current. Compared to sample No1, the photoresponsivity of sample No2 and No3 is improved by several orders of magnitude (Fig. 3.5b) due to the increased crystalline volume and reduced number of grain boundaries. In contrast with No1, both No2 and No3 exhibit much higher photosensitivity. However, the I_{ph}/I_{dark} ratio of No 3 is lower than that of No2 (Fig. 3.5b). The higher sensitivity of No 2 arises from the lower dark current. Increasing crystalline volume results in an improved photoresponsivity when the crystallization depth is below the photon penetration depth, but a large crystalline domain also enlarges the dark current, thereby impairing the photosensitivity of the device. We also characterized the respond speed of sample No3. Fig. 3.5c shows the response characteristics of the device to pulses of light irradiation switched at a frequency of 100 Hz and bias of 10 V under

different illumination intensities. A typical rise time of 0.44-0.45 ms and decay time of 0.47-0.50 ms were measured. The response speed only varies slightly with respect to the bias at fixed illumination intensity and frequency, as shown in Fig. 3.5d. The response speed of the device is comparable to or even higher than that of many wafer-based nanoscale devices[69][70][71][72][73].

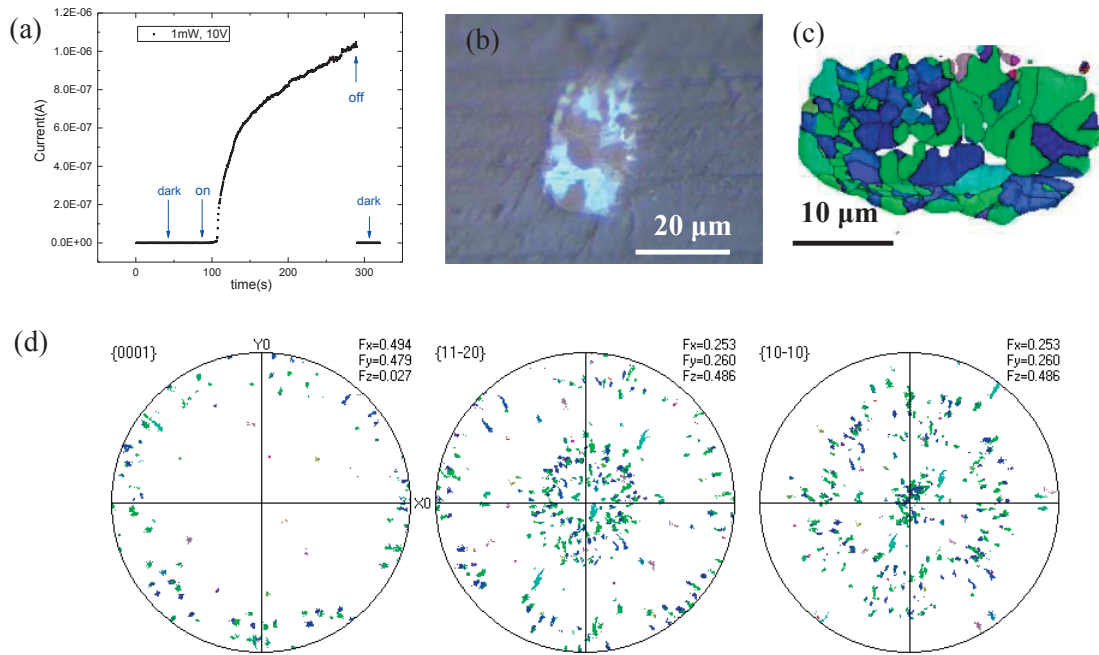


Fig. 3.4 (a) Annealing process for sample No3; (b) Optical micrograph of the cross-section of the annealed fiber; (c) The corresponding EBSD map on the crystalline Se in (b); (d) Pole figures of the directions normal to {0001}, {11-20} and {10-10} planes.

The effect of increasing the illumination power on enlarging the grain size is more pronounced than that of prolonging the annealing time, as demonstrated by the above study. We then further increased the illumination power to 2.3 mW to anneal the fiber for 30s (refer to as sample No4). Longer annealing time leads to a high dark current, indicating a significant crystallization depth. The optical micrograph (Fig. 3.6a) and the EBSD map (Fig. 3.6b) show that the average grain size is only slightly bigger than that of No3. The sample also exhibits roughly the same crystallographic orientation as the previous samples.

Temperature not only influences the kinetics of crystal growth but also strongly determines the nucleation rate. A low temperature gives rise to a low nucleation rate for the system. If we induce

nucleation at a relatively lower temperature and then drive the growth at a relative higher temperature, then we would potentially obtain a polycrystalline structure with a lower number of grains with larger sizes. In order to verify this assumption, we designed a novel annealing process

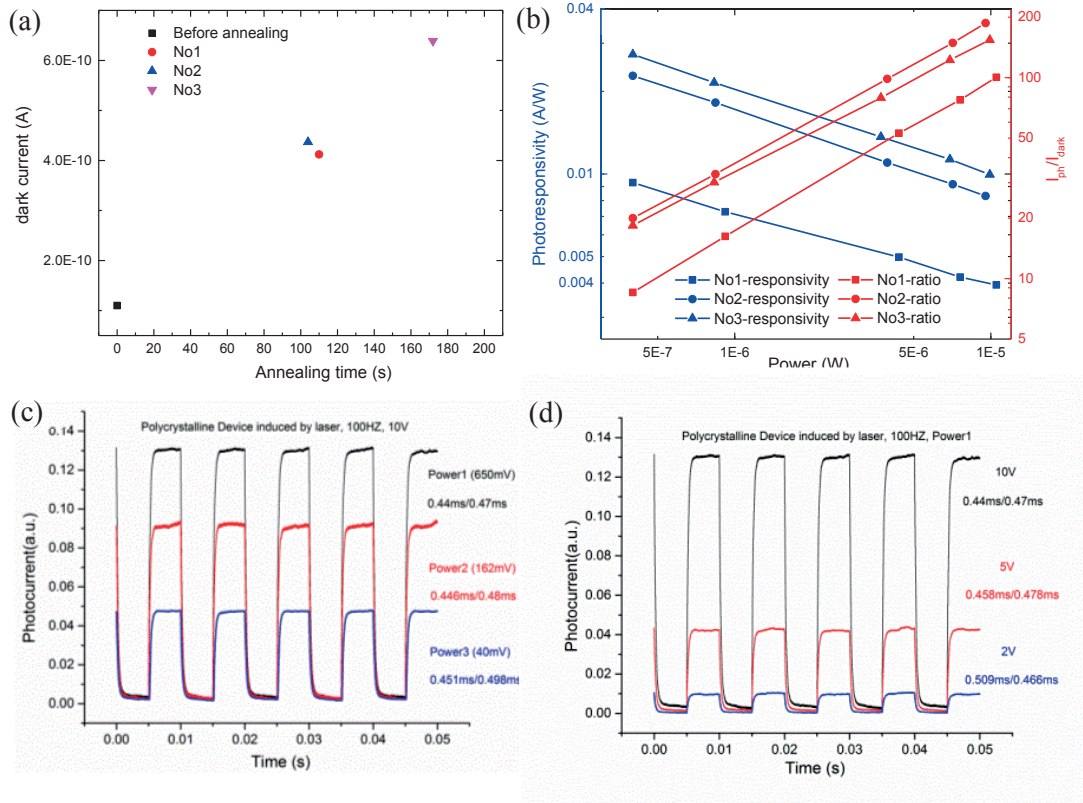


Fig. 3.5 (a) Dark current of the as-drawn sample before the laser treatment, and of sample No1, 2 and 3 after the laser treatment; (b) Comparison of photoresponsivity and I_{ph}/I_{dark} ratio of the annealed sample No1, 2 and 3 as a function of illumination power; (c) Response characteristics of the sample No 3 as a function of illumination intensity at the frequency of 100 Hz and the bias of 10 V. Power1 and Power2 and Power3 are 3.2E-3, 0.8E-3, 0.2E-3 $\mu W/\mu m^2$, respectively; (d): Response characteristics as a function of the bias under 3.2E-3 $\mu W/\mu m^2$ illumination and at the frequency of 100 Hz. Time for the current increasing from 10 % to 90 % of the peak value or vice versa is used for calculating the rise and fall time, respectively.

to induce crystallization on sample No5, namely we anneal the fiber many times with an increasing illumination power. As shown in Fig. 3.7a, the Se domain in the fiber was first annealed by a laser with the power of 200 μW . The in-situ recorded current from -10 V to 10 V

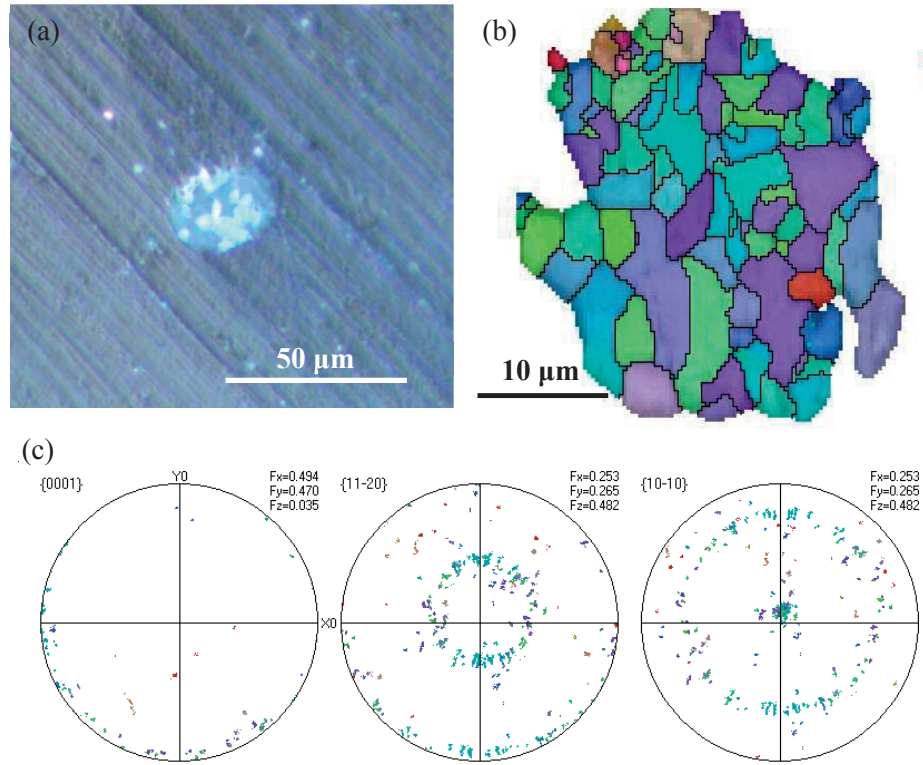


Fig. 3.6 (a) Optical micrograph of the cross-section of the annealed fiber No4. The illuminated power is 2.3 mW; (b) The corresponding EBSD map on the crystalline Se in (a); (c) Pole figures of the directions normal to {0001}, {11-20} and {10-10} planes.

remains as small as the current of as-drawn fiber, indicating no obvious crystallization formation in the amorphous Se. Then the power of the illumination was switched to 500 μW . The current still remain rather small between -10 V to 3 V. Subsequently, the current starts to increase rapidly at 4 V, indicating remarkable crystallization formation in the amorphous matrix. Finally, we applied the power of 800 μW to continue annealing the sample. It should be noted that the power of the illumination was increased to a higher power from a lower power with a ramp. The current was not recorded during the ramping process. The EBSD map of the annealed Se domain in the fiber is shown in Fig. 3.7b. It can be clearly observed that there are only a few grains in the polycrystalline structure and the average grain size reaches around 10 μm . The Kikuchi pattern in Fig. 3.7c can be indexed as trigonal phase. Impressively, the pole figure in Fig. 3.7d d illustrates that all crystals marked in green and blue in Fig. 3.7b are preferentially oriented with the basal plane of (0001) perpendicular to the direction of the electric field (in order to monitor crystallization evolution during the annealing, a bias is applied between CPC electrodes. The

electric field is therefore created during annealing). We also annealed another sample separately with the power of 200, 500 and 800 μW at a fixed voltage of 10 V. The annealing time at each annealing step was set 90 s. This treatment gave rise to the same microstructure characteristic.

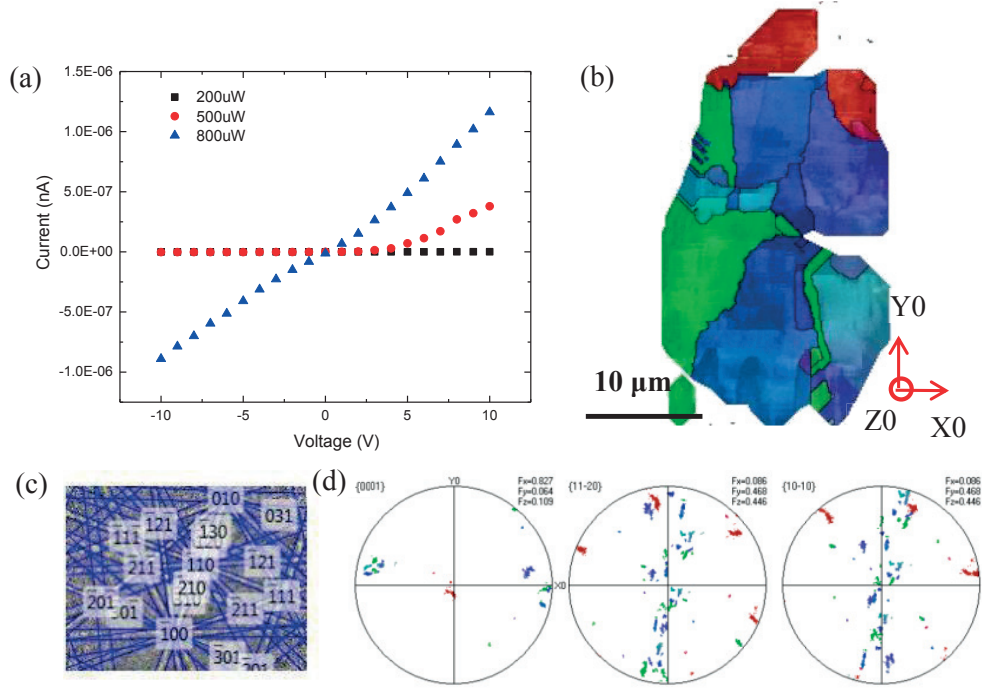


Fig. 3.7 (a) Annealing process for sample No 5. Current was in-situ recorded from -10 V to 10 V when the sample was annealed with different illumination powers; (b) EBSD map of the Se region after the laser treatment. The reference frames for the pole figure are indicated here; (c) Kikuchi patterns of the annealed fiber and its index; (d) Pole figures of the directions normal to {0001}, {11-20} and {10-10} planes.

We then prepared TEM lamella cut out of the fiber from the longitudinal direction, i.e., the fiber axis with ultramicrotomy to study the microstructure and the crystallization depth. The bright-field TEM image (Fig. 3.8a) taken from the middle region of the lamella clearly reveals a polycrystalline structure in the longitudinal section of the crystalline Se domain. The high-magnification TEM image in Fig. 3.8b shows that grain size is a few hundred nanometers that is much smaller than that of the cross-section (Fig. 3.7b). The crystallization depth in the middle region is around 1.1 μm while the depth is around 570 nm at the edge of the crystalline Se (Fig. 3.8c). This is because the power intensity of the laser beam in the center is higher than that at the

edge. The SAED pattern of the selected area marked by the red circle in Fig. 3.8c reveals there are only a few grains in the region, as shown in Fig. 3.8d.

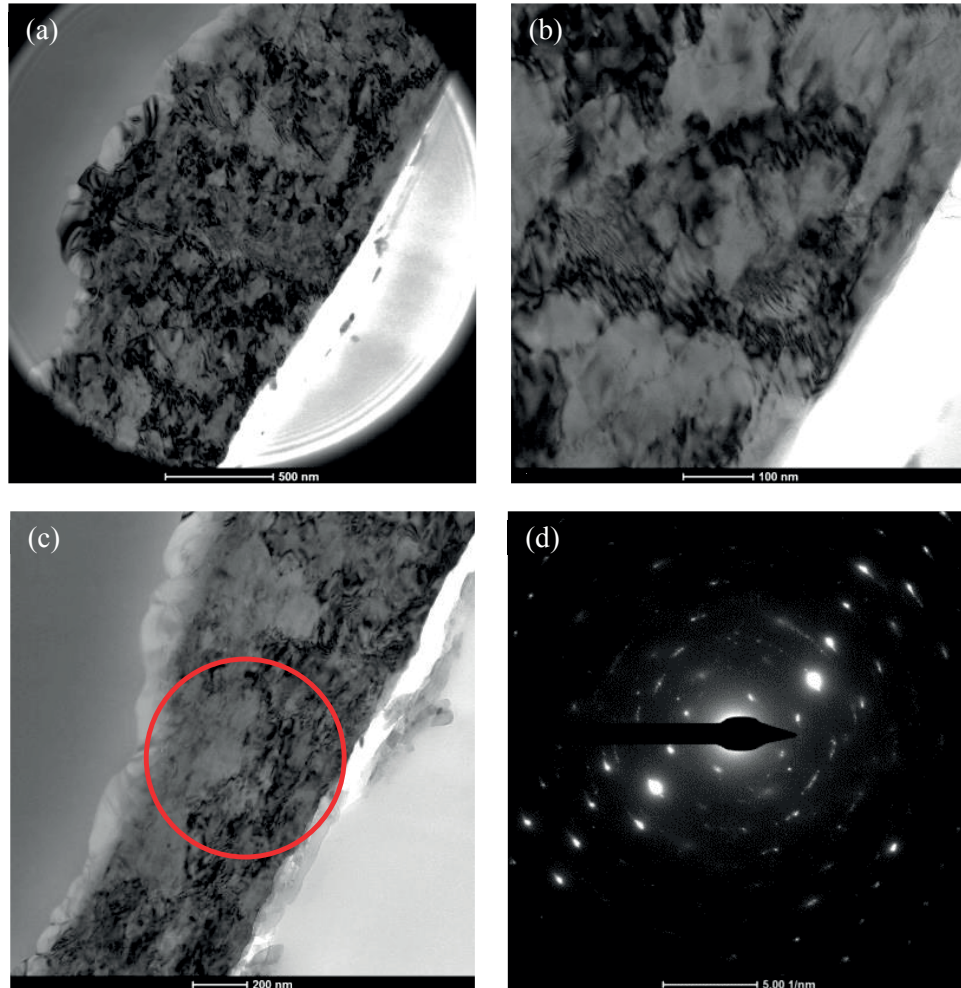


Fig. 3.8 (a) Bright-field TEM image of one middle part of the longitudinal section of the annealed fiber No5; (b) High-magnification bright-field TEM image; (c) Bright-field TEM image of one side part of the longitudinal section. The region from which the SAED pattern in Fig. 3.9d is taken is marked in a red circle; (d) SAED pattern of the region in Fig. 3.9d.

The EBSD characterization in Fig. 3.7d shows the preferential growth of the crystals at the fiber cross-section. In order to study the crystallographic orientation of the crystals in the longitudinal direction, we performed electron diffraction on four different regions in the longitudinal section of the crystalline Se, as indicated by the red circles in Fig. 3.9 (a, b, c and d). All the four selected regions with the diameter of 150 nm exhibit single crystal structure and the

same orientation with the basal plane of (0001) parallel to the CPC plane, revealing the same crystallographic orientation as that of the grains on the fiber cross-section.

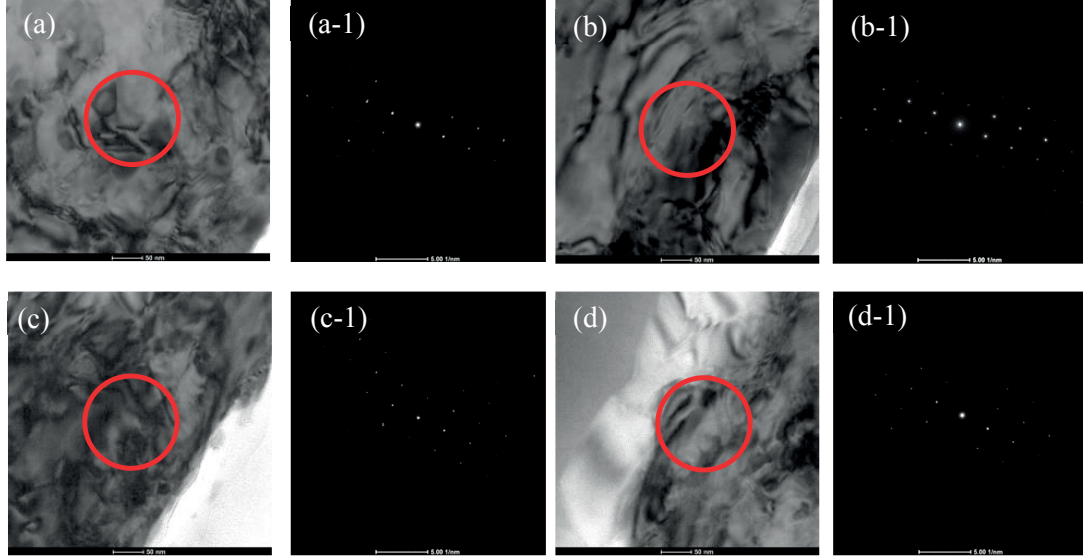


Fig. 3.9 (a, b and c) Bright-field TEM images of the region1, 2 and 3 in the longitudinal section of the annealed fiber; (a-1, b-1, and c-1) The corresponding SAED patterns of the marked region in a, b, and c.

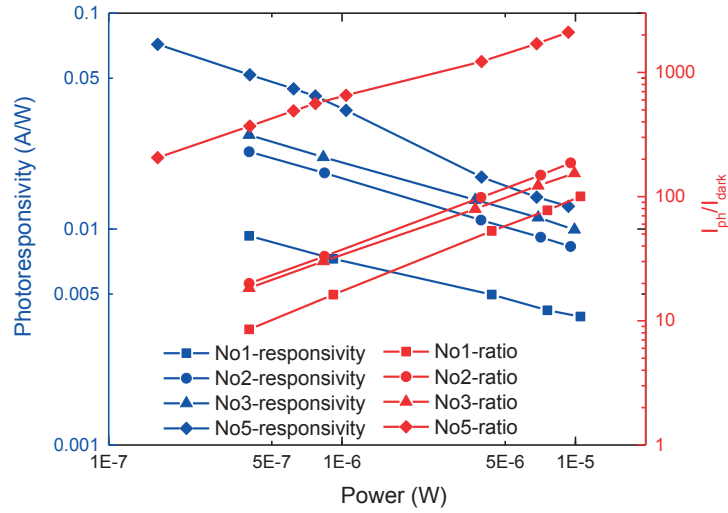


Fig. 3.10 Comparison of photoresponsivity and I_{ph}/I_{dark} ratio of the annealed samples No1, 2, 3 and 5 as a function of illumination power at the wavelength of 532 nm and the bias of 10 V.

Such an optimized microstructure with a very small crystallization depth, big grains in the cross-section perpendicular to the electrodes and grains with basal planes perpendicular to the

electric field direction is expected to exhibit superior optoelectronic performances. We then compare the photoresponsivity and the photosensitivity (I_{ph}/I_{dark}) of the sample No5 with previous samples as a function of illumination power at the wavelength of 532 nm and the bias of 10 V (Fig. 3.10). As we anticipated, these two figures of merits are several orders of magnitude higher than that of sample No1, 2 and 3. The photoresponsivity reaches 0.1 A/W at lower power and the sensitivity reaches 2000 at the power of 10 μ W. These performances are much more superior, compared to many wafer-based nanoscale devices fabricated in the clean room.

We then demonstrate that this laser annealing approach can not only induce crystallization at the fiber tip but also is can be applied in the longitudinal direction of the fiber. Thanks to the transparency of the PSU cladding, the laser beam can pass through it and be focused on the Se region at the fiber side, as schematically shown in Fig. 3.11a. We then used two annealing processes to treat two fibers. One was annealed with a constant illumination power (2.6 mW) and the other fiber was annealed with multi-step illumination (2 mW to 2.25 mW to 2.5 mW), as indicated in Fig. 3.11b. The optical micrograph of the side view of the fiber (Fig. 3.11c) shows that the annealed region exhibits different contrast from that of amorphous regions. We then studied the optoelectronic properties of the annealed region by focusing the light on it through the PSU cladding. Fig. 3.11d compares the photoresponsivity and photosensitivity (I_{ph}/I_{dark}) of the two samples as function of illumination power. Both of the two figures of merits of the two devices are lower than that of the previous devices in which crystallization was induced at the fiber tip. This can be due to the following reasons: i) the laser beam was not exactly focused on the Se region during the annealing process, as shown in the schematic of Fig. 3.12a, leading to a lower illumination intensity; ii) even if the laser beam can be exactly focused on the Se, the fiber could be rotated with respect to it, so that the real power that contributes to the annealing is lower (Fig. 3.12b); iii) the PSU cladding reflects and absorbs some photons during the characterization, so the real power that reach the Se region is lower than the applied power; iv) the illumination power and illumination time are not optimized. Because of these possible scenarios, the performance of sample1 that was treated with a single annealing step is higher than that of sample2 that was treated with a multi-step. Nevertheless, the preliminary results demonstrate that this laser annealing approach is also able to write high-performance photodetectors at any location along the fiber length. The crystallization depth of Se in this configuration is under investigation.

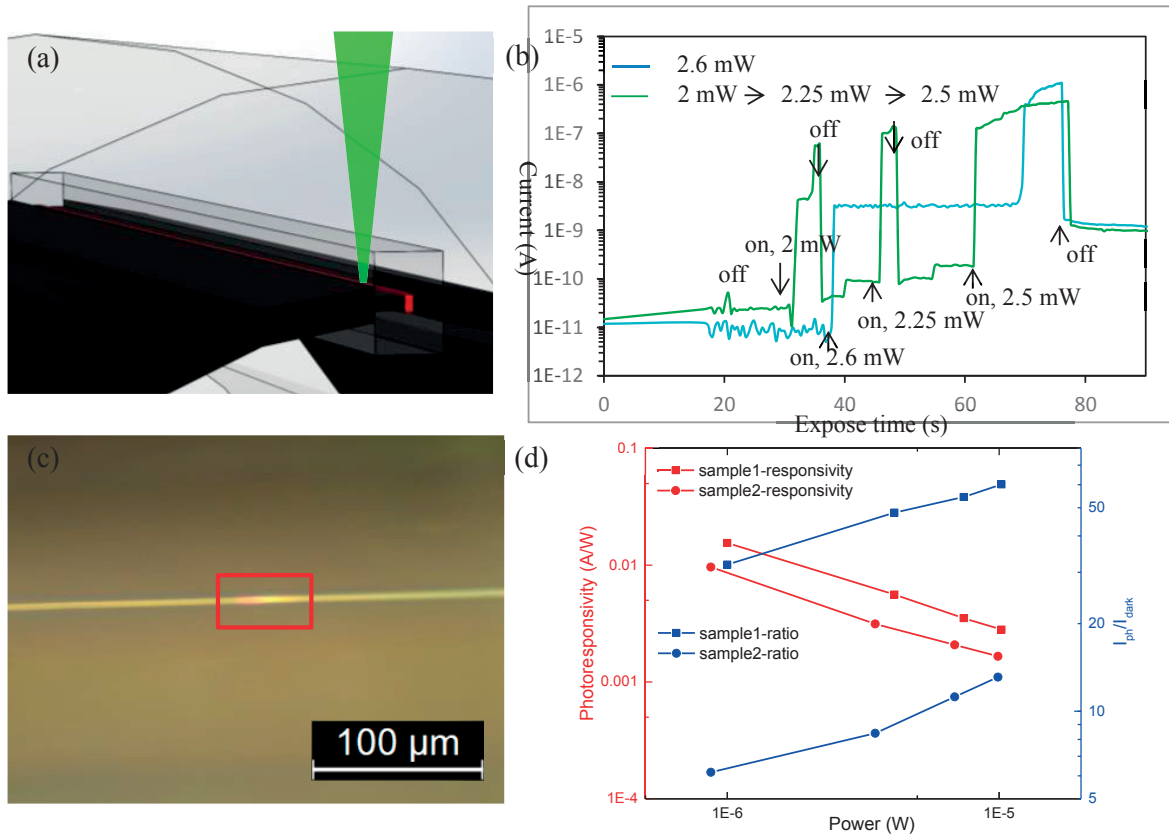


Fig. 3.11 (a) Schematic of the laser annealing approach applied on the fiber side; (b) Annealing processes for sample1 and sample2. The power was fixed at 2.6 mW for treating sample1 whereas the sample2 was first annealed with 2 mW then 2.25 mW followed by 2.5 mW. The wavelength of the incident light is 532 nm and the bias is 10 V; (c) Optical micrograph of the fiber side. The annealed region was marked with a red square; (d) Comparison of photoresponsivity and I_{ph}/I_{dark} ratio of the two annealed samples as a function of illumination power at the wavelength of 532 nm and the bias of 10 V.

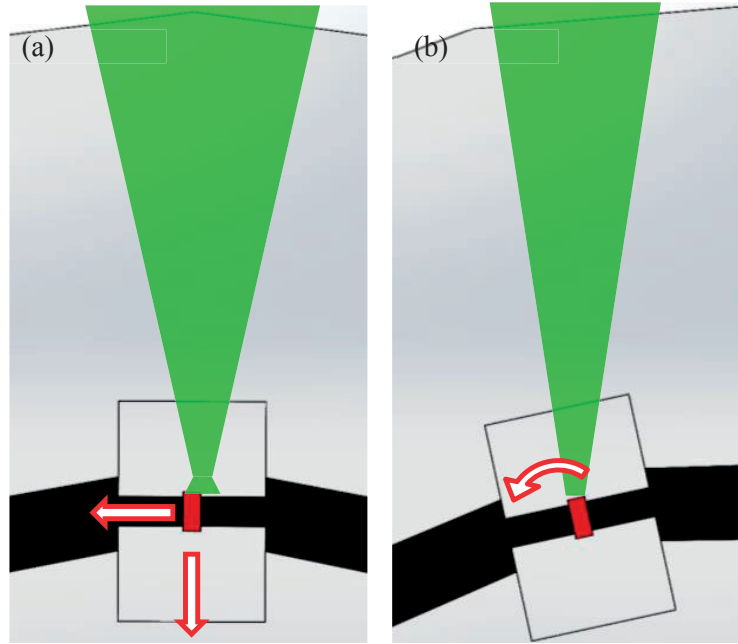


Fig. 3.12 Schematic of the laser beam with respect to the position of the Se region in the fiber during the annealing process. (a) laser beam is not well focused on the Se; (b) fiber is rotated with respect to the laser beam, leading to less power illuminated on the Se.

3.3 Discussion and summary

Phase transformation requires two processes, namely nucleation and crystal growth. The classical nucleation theory stemmed from the work of Volmer and Weber, Becker and Doring, and Frekel is the most common theoretical model to describe nucleation of a phase transition[74]. The free energy change associated with the nucleation process in a solid system consists of the following three contributions: i) the creation of a new phase with a volume of V in an amorphous matrix will cause a reduction of a volume free energy of $V\Delta G_v$; ii) the creation of an interface with an area A will lead to an increase of free energy of $A\gamma$; iii) the transformed volume during nucleation does not fit perfectly into the space occupied by the matrix, which gives rise to a misfit strain energy ΔG_s per unit volume of the new phase. Considering all these terms gives the total free energy change as

$$\Delta G = -V\Delta G_v + A\gamma + V\Delta G_s \quad (2.1)$$

If γ is treated as an orientation-independent constant and the cluster is assumed as spherical with a radius of curvature r , the equation 2.1 becomes

$$\Delta G = -\frac{4}{3}\pi r^3(\Delta G_v - \Delta G_s) + 4\pi r^2\gamma \quad (2.2)$$

Differentiation of Equation 2.1 yields

$$r^* = \frac{2\gamma}{\Delta G_v - \Delta G_s} \quad (2.3)$$

$$\Delta G^* = \frac{16\pi\gamma^3}{3(\Delta G_v - \Delta G_s)^2} \quad (2.4)$$

r^* is called critical nucleus size and is associated with a maximum excess free energy. If $r < r^*$ it is energetically favorable for clusters to disappear, whereas when $r > r^*$ the total free energy of the system reduces if clusters grow.

Denote the density of atoms in the amorphous matrix as n_0 , and density of clusters of radius r in equilibrium with the matrix as n_r . Since nucleation is a thermally activated process, the energy of atoms follows a Maxwell-Boltzmann distribution. The density of spherical clusters of radius r can be expressed by

$$n_r = n_0 \exp\left(-\frac{\Delta Gr}{kT}\right) \quad (2.5)$$

where ΔGr is the excess free energy associated with the cluster, i.e., equation 2.2, and k is Boltzmann's constant.

The density of clusters that reach the critical size can be obtained from equation 2.5 as

$$n_r^* = n_0 \exp\left(-\frac{\Delta G^*}{kT}\right) \text{ clusters m}^{-3} \quad (2.6)$$

A nucleus of critical size r^* will grow if one more atom is added. If this happens with a frequency f_0 , the homogeneous nucleation rate will be given by

$$N_{\text{hom}} = f_0 n_0 \exp\left(-\frac{\Delta G^*}{kT}\right) \text{ nuclei m}^{-3} \text{ s}^{-1} \quad (2.7)$$

where f_0 is associated with a frequency with which an atom from the matrix attaches with a critical nucleus. This frequency depends on the vibration frequency of the atoms, the activation energy for diffusion in the matrix, and the surface area of the critical nuclei. Considering activation energy for atom migration as ΔG_m , f_0 can be formulated as

$$f_0 = w \exp\left(-\frac{\Delta G_m}{kT}\right) \quad (2.8)$$

The nucleation rate will therefore be written as

$$N_{\text{hom}} = w n_0 \exp\left(-\frac{\Delta G^*}{kT}\right) \exp\left(-\frac{\Delta G_m}{kT}\right) \quad (2.9)$$

The first exponential term represents the thermodynamic driving force for crystallization while the second exponential term is a kinetic contribution.

Once the size of a cluster is bigger than the critical nucleus size, the nucleus starts to grow as long as the external driving force is provided. Fig. 3.13 shows the four configurations of different boundaries curvatures. It is assumed that the angle at the boundary junction in equilibrium state is 120° . Therefore, the boundary of a grain that has six boundaries is planar and the grain is metastable. If the number of boundaries of a grain is less than six, each boundary must be concave inwards. These grains will shrink and eventually disappear. On the contrary, grains with more than six boundaries will grow. The overall effect of such boundaries migration is to reduce the number of grain boundaries that are high-energy regions, thereby reducing the total energy of the system. The grain boundary migration rate can be written as:

$$v = \alpha M \frac{2\gamma}{\bar{D}} \quad (2.10)$$

where α is a proportionality constant of the order of unity, M is the boundary mobility and \bar{D} is the mean grain diameter.

This equation indicates that the grain growth rate is inversely proportional to the mean grain diameter and increases with increasing temperature owing to increased boundary mobility.

Sample No2 and 3 annealed with the power of 1 mW exhibit larger grains, compared to sample No1 annealed with the power of 0.6 mW. Even though the number of nuclei in sample No2 and 3 is higher than that of sample No1 according to the classical nucleation theory, the grain growth rate in sample No2 and 3 is also higher than that in sample No1. Many grains in sample No2 and 3 eventually disappear during the annealing process, exhibiting higher mean grain diameter. The annealing time for sample No3 is longer than that of sample No2, but the mean grain size of the former is just slightly bigger than that of the latter. This is first because a big grain has a slow growth rate according to the equation 2.10. Secondly, the growth rate is inversely proportional to the square root of growth time, namely $v \propto \sqrt{D/t}$ where D is the diffusion coefficient (diffusion of Se atoms between the amorphous state and the crystalline state) and t is the growth time. The grain size of sample No4 can be bigger due to a higher illumination power (2.3 mW) if we apply the same annealing time as that of sample No3. However, such a high power is able to generate intense heat that can rapidly cause a high-volume crystallization region, leading to a high dark current and low sensitivity. The multi-step annealing approach applied to sample No5 exhibits the biggest grains, which can also be explained by the above nucleation and growth theory. When the sample is annealed with a relatively weaker power, namely 0.3 and 0.5 mW, nucleation dominates during the crystallization and the number of nuclei is few due to a low annealing temperature. When a high power is used to continue to anneal the sample, grain growth dominates and leads to the formation of big grains.

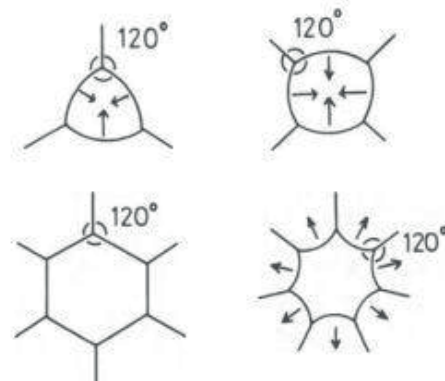


Fig. 3.13 Two-dimensional grain boundary configurations. The arrows indicate the directions boundaries migrate during grain growth.

Strikingly, crystals in sample No5 are preferentially oriented with the basal plane of (0001) perpendicular to the direction of the electric field (parallel to the CPC planes). The heterogeneous

nucleation and the newly developed heterogeneous nucleation associated with anisotropy by A. Mariaux and M. Rappaz[75] can provide insight into this issue, which will be discussed below.

Nucleation in solids is always heterogeneous instead of homogeneous. Non-equilibrium defects in a material such as vacancies, dislocations, grain boundaries, stacking faults, impurities and free surfaces are possible nucleation sites. The presence of these defects increases the free energy of a material. If the formation of a nucleus results in the destruction of a defect, some free energy ΔGd will be released thereby decreasing the activation energy barrier. The equation describing free energy change of the system is

$$\Delta G = -V\Delta Gv + A\gamma + V\Delta Gs - \Delta Gd \quad (2.11)$$

For both homogeneous and heterogeneous nucleation theories, the interfacial energy is assumed to be isotropic. In many cases, the anisotropy of interfacial energy between solid/liquid, solid/solid and solid-substrate however cannot be neglected. Anisotropy therefore favors particular orientation of the nucleus on the substrate[75]. In this case, the equivalent to equation 2.11 becomes

$$\Delta G_{het} = -V\Delta Gv + \int_{A_{sl}} \gamma_{sl}(\vec{n}_{sl})dA - \Delta\gamma \int_{A_{fs}} dA \quad (2.12)$$

where A_{sl} is the solid-liquid interface area and A_{fs} is the solid-substrate interface area. \vec{n}_{sl} the unit vector normal to the solid-liquid interface. $\Delta\gamma$ is defined as $\Delta\gamma = \gamma_{lf} - \gamma_{fs}$, as shown in the following schematic (Fig. 3.14).

According to classical heterogeneous nucleation theory, the activation energy barrier for heterogeneous nucleation is given by

$$\frac{\Delta G_{het}}{\Delta G_{hom}} = \frac{V_{het}}{V_{hom}} = f\left(\Delta\gamma/\gamma_{sl}^o, \vec{n}_{fs}\right) \quad (2.13)$$

where the ratio f is a shape factor and depends only on the wetting conditions ($\Delta\gamma/\gamma_{sl}^o$) and the orientation \vec{n}_{fs} of the substrate.

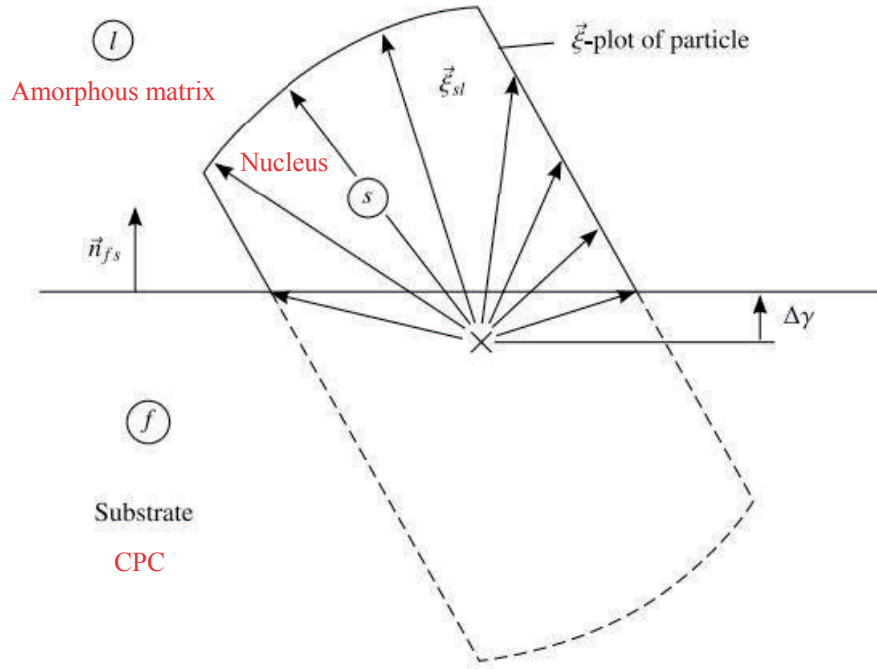


Fig. 3.14 Anisotropic particle on a flat surface[75]. l, s, f denote liquid, solid and foreign substrate, respectively. This model can also be applied to our system, so l, s, f denote amorphous matrix, solid nucleus and CPC electrode, respectively.

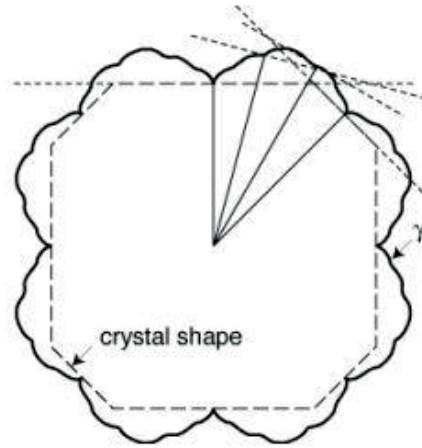


Fig. 3.15 Example of Wulff construction.

Therefore, f is dependent on the orientation of the nucleus on the substrate, which results in a lower nucleation energy for some orientation thereby favoring nucleation with these orientations[75].

The volume of a homogeneous nucleus can be obtained based on equation 2.3. The volume of a heterogeneous nucleus can be obtained by numerical integration of $V_{het}(\Delta\gamma/\gamma_{sl}^o, \alpha)$, where α is the angle between a crystallographic axis and the normal to the substrate \vec{n}_{fs} . In order to get $V_{het}(\Delta\gamma/\gamma_{sl}^o, \alpha)$, we should know the equilibrium shape of a nucleus. The equilibrium shape of a crystal is obtained by γ -plot and Wulff construction[76]. To begin, the variation of γ with surface orientation is plotted by constructing a surface about an origin such that the free energy of any plane is equal to the distance between the origin and the tangent line of the point of the plane. This tangent line is called Wulff plane (Fig. 3.15). For an isolated crystal bounded by several planes A_1, A_2 , etc. with energies γ_1, γ_2 , etc. The equilibrium shape is defined when the sum of $A_i\gamma_i$ is a minimum. The equilibrium shape is then simply the inner envelope of all such planes[76].

Taking zinc for example, the activation energy barrier is smaller when $\alpha = 0^\circ$ than that when $\alpha = 60^\circ$ for a wetting angle $\theta = 60^\circ$, as shown in Fig. 3.16 (a and b). In this case, nuclei are preferentially oriented with the c axis parallel to \vec{n}_{fs} . When the wetting angle is $\theta = 120^\circ$ (Fig. 3.16 (c and d)), nuclei are preferentially oriented with the c axis with a 60° with respect to \vec{n}_{fs} . Fig. 3.16e illustrates the ratio of the Gibbs free energies associated with heterogeneous and homogeneous nuclei, as a function of the wetting condition, for different orientations, which highlights that nucleation is favored for some orientation and hindered for others. This newly extended nucleation model sheds new light into the nucleation mechanism of Se system in the fiber. The preferential orientation of crystals with the basal plane of (0001) parallel to the CPC planes in sample No5 observed by EBSD and TEM characterization can be rationalized in terms of the above nucleation mechanism, namely nucleation on CPC electrodes is energetically favored when the (0001) plane of nuclei is parallel to the CPC planes.

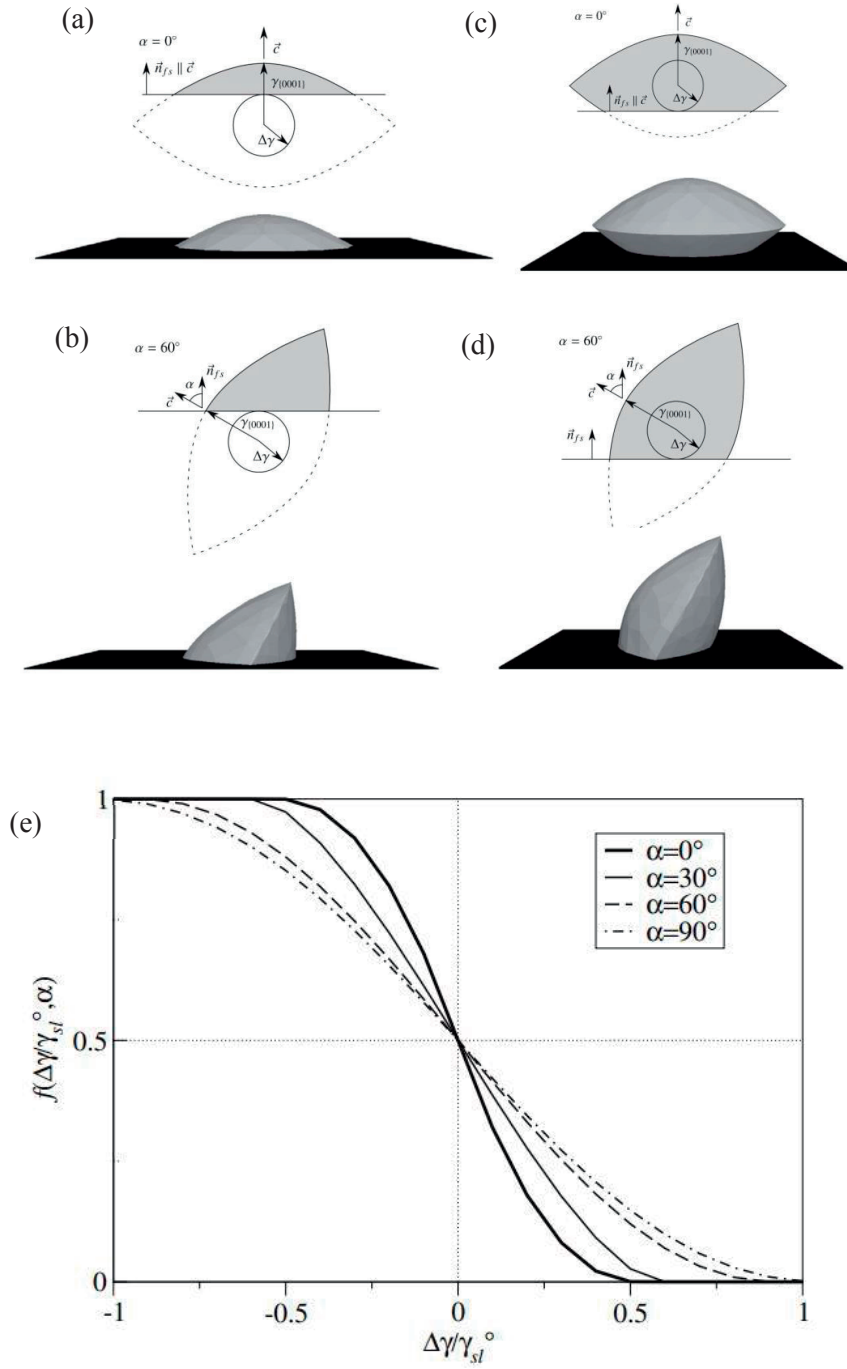


Fig. 3.16 shape of zinc nuclei on a flat substrate for different orientations and wetting conditions: (a and b) $\Delta\gamma = 0.5\gamma_{sl}^0$ and (c and d) $\Delta\gamma = -0.5\gamma_{sl}^0$; (e) ratio of the Gibbs free energies associated with heterogeneous and homogeneous nuclei, as a function of the wetting condition, for different orientations[75].

Finally, we discuss why the specific crystal orientation in sample N°5 induces a better optoelectronic response. As a trigonal phase, Se consists of a spiral chain of atoms with three atoms per turn. Atoms in each chain form a hexagonal network. The bonds between atoms on the same chain are covalent while cohesion between the chains is ascribed to weaker van der Waals forces. The preferential orientation of (0001) plane shown in Fig. 3.17 implies that (0001) plane is normal to the electric field direction when a bias is applied on the device. The electrons can easily transport along the chains due to the covalent bonding between the atoms. The high charge carrier mobility leads to a superior optoelectronic properties of sample No5.

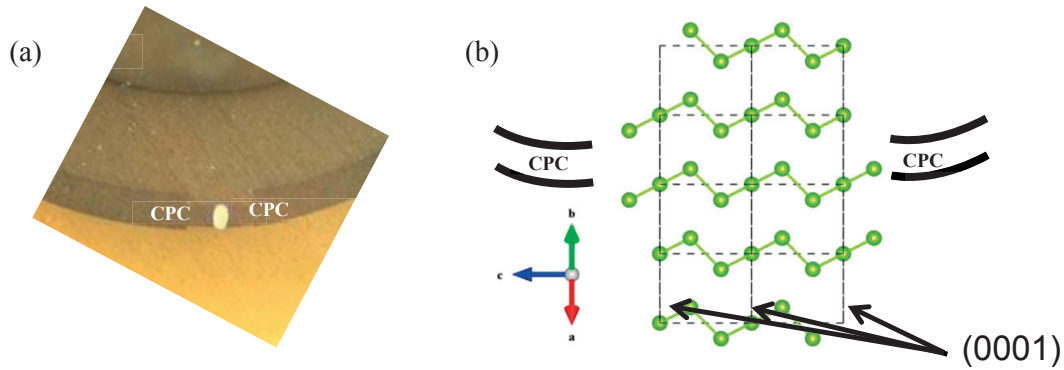


Fig. 3.17 (a) Optical micrograph of the Se region; (b) Schematic of the orientation of (0001) planes with respect to CPC electrodes.

In summary, we developed a laser-annealing approach to induce crystallization on the Se in optoelectronic fibers. The effect of laser illumination power and exposure time on microstructure formation, namely grain size, crystallographic orientation and crystallization depth was investigated. The multi-step annealing approach enables preferential orientation of crystals with the basal plane of (0001) perpendicular to the direction of the electric field that is created when a bias is applied between the CPC electrodes for optoelectronic characterization, which results in extraordinary optoelectronic properties. The microstructure formation can be understood by the extended heterogeneous nucleation theory that considers the anisotropy of the interfacial energy. The laser-annealing approach can not only induce crystallization at the fiber tip but can also have the potential to write high-performance detectors at any position along kilometer-long fibers. This

approach is also applicable to control the microstructure formation in other in-fiber semiconductors.

3.4 Experimental methods

The Electron BackScatter Diffraction (EBSD) maps were acquired at 20 kV on a FEG-SEM XLF30 (FEI) equipped with a Nordlys II camera; they were treated with the Aztec software (Oxford Instruments).

Transmission electron microscope (TEM) samples were prepared by embedding them in epoxy resin followed by sectioning thin slices (60 nm) using ultramicrotomy (diamond grade) which were transferred on a carbon/Cu grid supports (300 Mesh). The TEM images and selected area electron diffraction (SAED) were taken using talos F200X operating at 80 kV.

The fiber cross-section was placed perpendicular to the laser beam when inducing crystallization at the fiber tip while the fiber axis was amounted perpendicular to the laser beam to induce crystallization at the fiber side. The electrical and photoresponse characteristics were measured using a Keithley 6517B under dark and illuminated conditions. The SuperK Extreme from NKT Photonics, with tunable power was used as the light sources to anneal the fiber and to characterize the annealed fiber. The optical laser power was adjusted using an afocal lens system and was measured using a laser power meter (Thorlabs PM 100D). The laser beam used to characterize the optoelectronic properties of the devices was incoming perpendicularly to the fiber cross-section (hence parallel to the fiber axis) or the crystallization position at the fiber lateral side. The beam size was set to be the same as the size of the larger side of the rectangular Se domain in the fiber cross-section. Time resolved responses of the devices were measured using a pulsed LED with the frequency of 100 HZ, and an oscilloscope was used to monitor the variation of current with time. All measurements were performed in air and at room temperature.

Chapter 4 Monocrystalline Semiconductor Nanowire-based Optoelectronic Fibers

In this chapter, I will introduce, for the first time, a simple and robust integration of high-quality single crystal semiconducting nanowire-based optoelectronic devices at the fiber tip and along the fiber length. This approach contrasts with annealing-based techniques traditionally used thus far in semiconductor fibers. It consists in two steps: first, a multi-material optoelectronic fiber that integrate semiconductor Se, conducting nanocomposite CPC and PSU cladding was fabricated by thermal drawing approach. Then, a solution-based approach was applied at the fiber tip to induce single crystal nanowires formation. I will show the structure characterization using SEM and TEM. In order to further gain insight into the nanowire formation mechanism, first principles density-functional theory calculations was employed to simulate the interfacial energies of crystallographic planes. After studying the optoelectronic properties of the nanowire-based device at the fiber tip, I will show a hybrid fiber that exhibits a unique combination of optical guidance and high photosensitivity. This novel platform was used to demonstrate an all-fiber-integrated fluorescence imaging system. Finally, I will show that this simple approach can not only be applied at the fiber tip, but also is compatible to the integration of nanowires into devices along the fiber length. The optoelectronic properties at any position along the fiber length are on par with the nanowire-based device at the fiber tip.

4.1 Fiber Fabrication and Characterization

The architecture of the first fiber (later referred to as the “precursor fiber”) in this chapter is similar as the fiber in the chapter 2. The fibers were fabricated via the thermal drawing of a macroscopic preform, as schematically illustrated in Figure 4.1(a). The preform is composed of a rectangular Se core that is intimately sandwiched by CPC nanocomposite electrodes and run along the entire the fiber length. This assembly is encapsulated within PSU cladding, a thermoplastic that supports the drawing stress and protects the inner materials of the fiber. The preform was consolidated in a hot press at 215 °C for 30 minutes before it was drawn at 285 °C, a temperature above the glass transition temperature of PSU and CPC and the melting point of Se, into a fiber more than 100 m in length. The optical micrograph of the fiber cross-section in Fig. 4.1b shows the square Se domain is in intimate contact with CPC electrodes within an architecture that is an exact scaled down version of the initial preform. The width of Se core, i.e., the distance between the CPC electrodes is roughly 150 μm . X-ray diffraction as well as selected-

area electron diffraction (SAED) from transmission electron microscope (TEM) characterization on the Se harvested from the as-drawn fiber indicates that Se is amorphous, as shown in Fig. 4.1(c).

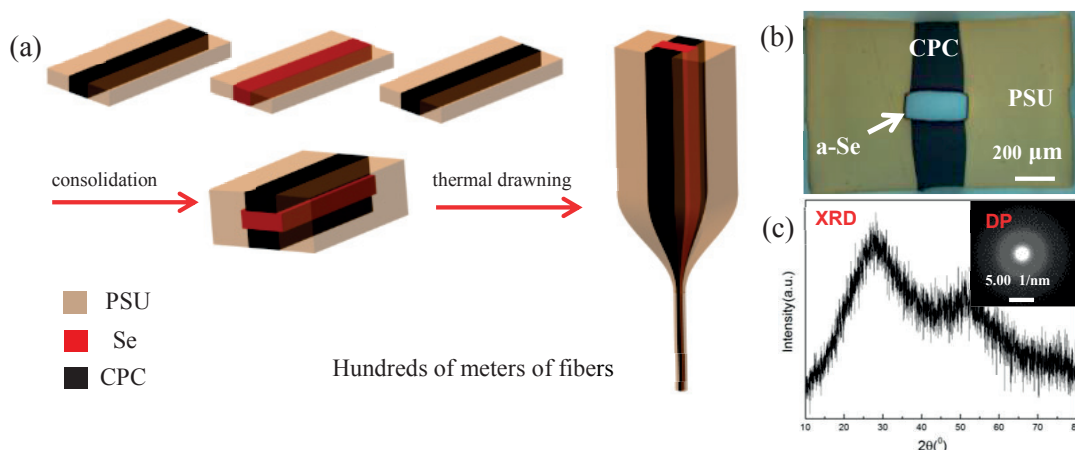


Fig. 4.1. (a) Schematic of preform and fibers fabrication; (b) optical micrograph of the fiber cross-section; (c) XRD and SAED of the Se in the as-drawn fiber.

4.2 Nanowire synthesis and growth mechanism

As discussed in the chapter 2, the optoelectronic properties of amorphous material are poor. A powerful method to tailor the microstructure and enhance optoelectronic properties is via the growth of well-oriented semiconducting nanowires. Compared to the counterpart polycrystalline semiconducting bulk, semiconducting nanowires exhibit high light absorption, efficient charge extraction, high photoconductive gain and high photosensitivity due to the large surface-to-volume ratio and reduced dimension of the detecting area[77]. However, the growth of nanowires has not been exploited in the frame of fiber-integrated devices. The reasons for this are two-fold: first, conventional fabrication procedures of semiconducting nanowires in the clean room, namely bottom-up and top-down approaches are very complex and are mostly suitable for planar and rigid substrates; secondly, the integration of nanowires into devices relies on high-resolution patterning technique that is incompatible with the thermal drawing process and the small cross-section and large aspect ratio of the fiber. Here we bypass these limitations and demonstrate for the first time the integration of single crystal semiconducting nanowire-based optoelectronic devices at the fiber tip and along the length of polymer fibers by a very simple and scalable approach. The whole fabrication process is schematically shown in Fig 4.2a. The fiber tip was first polished using silicon carbide paper to get a smooth surface and to ensure a good interface

between the amorphous Se and the CPC electrodes. The fiber tip was then sonicated in distilled water for 1 minute to clean the cross-section and to induce nucleation in the amorphous Se matrix that is due to intense local heating and high pressure produced by the cavitation effect[78]. Subsequently, the fiber tip was soaked in 1-propanol that can dissolve amorphous Se[79] for 5 days at ambient condition without any elevated temperature. Fig. 4.2b shows a high dense array of Se nanowires grow between the CPC electrodes. The magnified SEM image in Fig. 4.2(c) reveals that the diameter of the nanowire is around 200 nm. The nanowire mesh intimately interfaces with the CPC electrode, as shown in Fig. 4.2d.

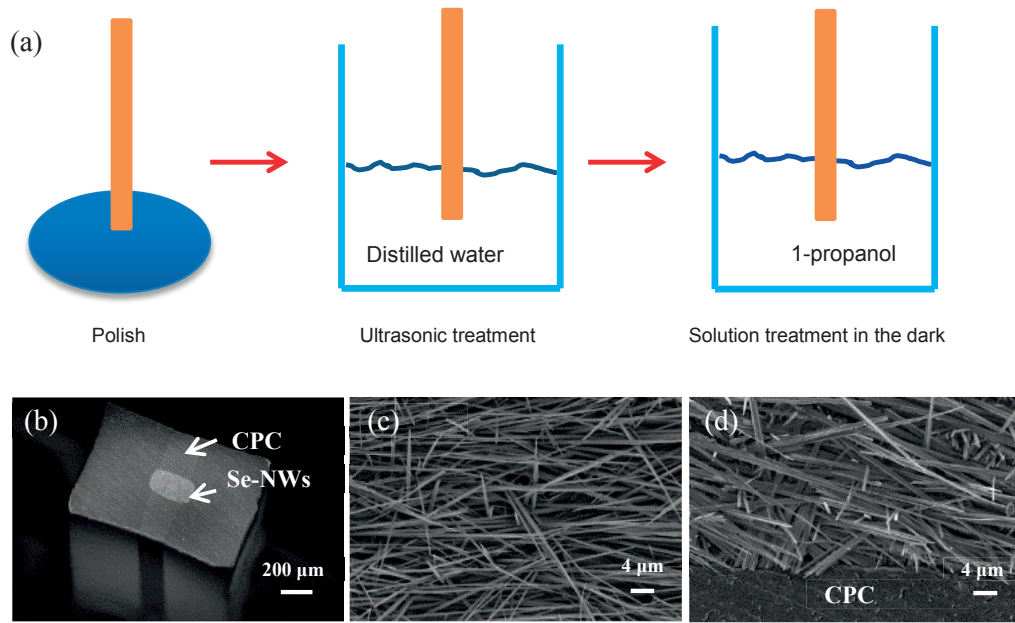


Fig. 4.2. (a) schematic of Se nanowire synthesis process; (b) SEM micrograph of the fiber tip; (c) high magnification SEM micrograph of the Se nanowire mesh; (d) SEM micrograph of the interface between the CPC and Se nanowires.

Se nanowires have been widely fabricated from amorphous nanoparticle seeds obtained by the reduction of Se-based compounds via a hydrothermal approach[80][40]. Here we found that Se nanowires can be easily synthesized from amorphous bulk at room temperature. The SEM micrograph of Fig. 4.3a clearly shows that nanowires grow from the nuclei formed in the amorphous matrix. In order to understand the growth mechanism of the nanowires, we first performed electron microscope characterization on the crystallographic structure of the nanowires. As shown in Fig. 4.3(c), the SAED of a typical nanowire (Fig. 4.3b) obtained by focusing the electron beam along the $[10\bar{1}0]$ zone axis indicates that the nanowire preferentially

grow along the $[0001]$ direction. This pattern can be indexed as trigonal phase. The lattice constants calculated from the pattern ($a = 0.432$ nm, $c = 0.493$ nm) correspond well to those of Se trigonal phase ($a = 0.436$ nm, $c = 0.495$ nm)[81]. A series of diffraction patterns taken from different regions of an individual nanowire were essentially the same, it could be concluded that the nanowires synthesized using the present procedure were monocrystalline in structure. A high-resolution TEM image (HRTEM) in Fig. 4.3d taken from the nanowire shows a fringe spacing (~ 0.5 nm) that agrees well with the separation between the (0001) lattice planes, which confirms the nanowires are single crystals and grow along the $[0001]$ direction. The preferred crystallographic orientation and one-dimensional geometric morphology characteristic of the nanowires may be caused by its highly anisotropic structure of trigonal Se.

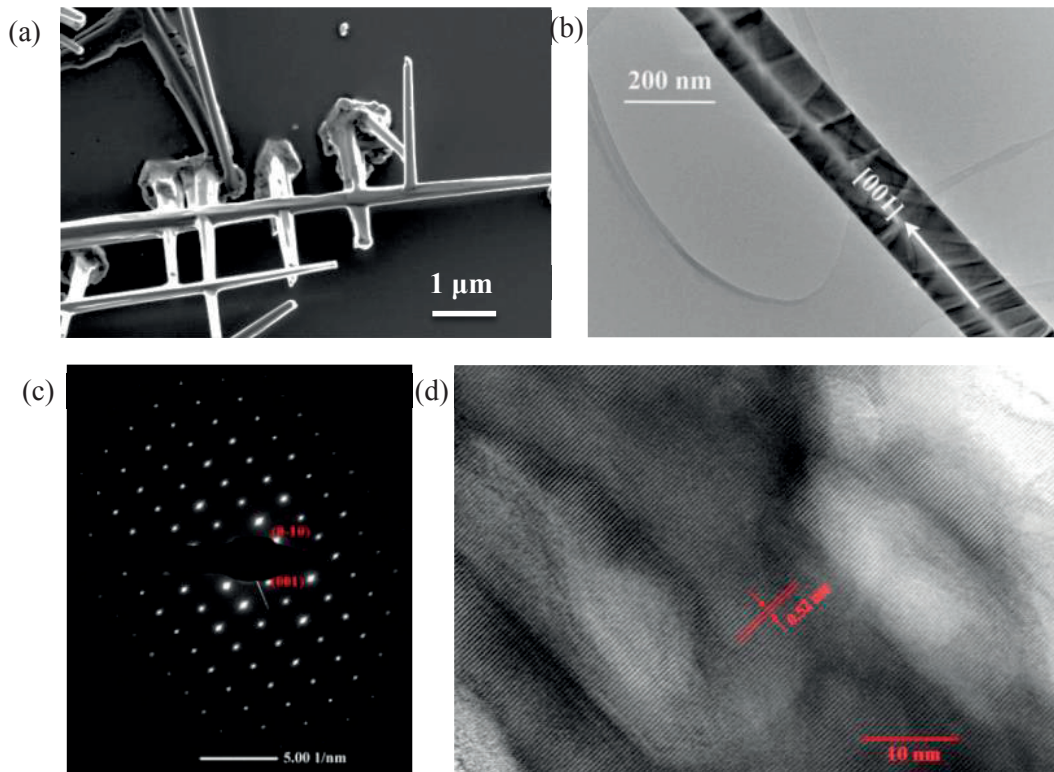


Fig. 4.3. (a) SEM micrograph of Se nanowires growing from amorphous bulk matrix. The sample was soaked in 1-propanol for 12 hours; (b) Bright-field TEM image of a single nanowire; (c) SAED pattern of the nanowire in (b); (d) HRTEM image of a single nanowire obtained from the fiber cross-section that was soaked in 1-propanol for 5 days.

In order to further gain insight into the formation mechanism of these nanowires, we then performed first principles density-functional theory calculations using the PBE exchange

correlation functional and many body van der Waals scheme (MBD)[82][83]. All theoretical calculations were run with the FHI-aims program[84], which is an all electron, numeric atom center basis set electronic structure code. Relativistic effects in our calculations were taken into account through the atomic zeroth order regular approximation (ZORA) method[85]. All numbers reported correspond to FHI-aims tight settings for basis sets, grids, and other numerical parameters. Relaxations were performed for all structures until forces were lower than 0.002 eV/Å. We first calculated the lattice constant of bulk Se, which was determined by varying the $a(=b)$ and c parameters of the unit cell (3 atoms per unit cell forming helical chains, isomorphic to Tellurium), and maintaining the angles at $\alpha = \beta = 90^\circ$ and $\gamma = 120^\circ$. We then performed Murnaghan fits to the calculated points. The values thus obtained were compared experimental data at $T = 77$ K and $T = 300$ K taken from Ref[81], as shown in Table 4.1. Our calculations show a slight overestimation of c and slight underestimation of a with respect to experiment (of the order of 2-3%). However it is important to notice that with rising temperatures, a tends to expand while c tends to shrink, such that our numbers would be in closer agreement with an experimental lattice constants at 0 K. The deviations we observe are also consistent with values reported for the PBE functional[86].

Table 4.1 Lattice constants of bulk Se in this work and experimental data. All values are in Ångstrom.

	PBE+MBD	Exp. (77 K)	Exp. (300K)
a	4.22	4.30	4.37
c	5.11	4.98	4.95

To study whether the anisotropy of the surface energy can provide a thermodynamic drive force for the nanowire growth, we calculated the surface energies of the typical prismatic planes and basal plane. Given the crystal structure and space group of the selenium crystal (P3121), the shape of the crystal particle involves two distinct surfaces, namely the (01-10) surface and the (01-1-1) surface. The first does not break covalent bonds (prismatic plane) while the latter does. We thus calculated the surface energies of the (01-10) surface and the (01-1-1) surfaces, as well as the surface energy of the basal plane (0001) for comparison, since this plane is the one which breaks most covalent bonds and is thus a limiting case. The surface energies of solid/vacuum were calculated as

$$\gamma_s = \frac{1}{2A_s}(E_s - NE_{bulk}) \quad (4.1)$$

where A_s is the area of the surface, s is the orientation of (01-10), (01-1-1) and (0001), E_s is the total energy of the supercell, N is the number of the atoms in each calculation, and E_{bulk} is the bulk energy per atom. In order to allow for reconstruction, especially for the surfaces that cut through covalent bonds, we have considered large surface areas and all calculations included at least 6 layers. The surface energies we thus obtained are $\gamma(01-10) = 0.009$, $\gamma(01-1-1) = 0.027$ and $\gamma(0001) = 0.039$ eV/Å² (Figure 4.4b). We used a 6x6x1 k-point mesh, which we found to be converged for the cell sizes we considered. Given the surface energies for the PBE+MBD functional, we calculated the optimum ch/ah ratio for the crystal (Fig. 4.4 a) by calculating its full surface area and volume as a function of ch and ah and subsequently minimizing the overall surface energy for a fixed volume

$$\frac{ch}{ah} = \frac{\gamma(01\bar{1}\bar{1})}{\gamma(01\bar{1}0)} \sqrt{4f^2 + 3} \quad (4.2)$$

where $f = 0.9517$ is a geometric factor that depends on the angle between the pyramidal planes. Given the values of the surface energies we calculated (see main text) we thus find $ch/ah = 7.7$, predicting an elongated equilibrium shape that is consistent with the habit of native selenium.

We then roughly estimated the work of adhesion by computing the binding energy E of one 1-propanol molecule on a given surface (Fig. 4.4c), and its contact area with that surface. We calculated the binding energy of 1-propanol with the PBE+MBD method on the different Se surfaces, exploring a few orientations of the molecule. After relaxation, the oxygen atom always tended to be closer to the surface. Binding energies were found to vary depending on orientation. Since we did not do a full orientational scan for all surfaces, and molecules in a solvent would exhibit different orientations with respect to the surface, we assume a conservative error of 25% as our uncertainties in the binding energies. We calculated the binding energies to be $E_{01-10} = -0.30 \pm 0.08$ eV, $E_{01-1-1} = -0.57 \pm 0.15$ eV and $E_{0001} = -0.28 \pm 0.07$ eV. The contact area of the propanol molecule was estimated to be between 27 and 37 Å² given the geometry of the molecule and the vdW radii of its constituent atoms. We thus take this number to be approximately $A = 32$ Å² for all surfaces. We compute $\gamma_s^{prop} = \gamma_s + \gamma_{prop} - E/A$, where we estimate the work of adhesion through the binding energy E s of a single molecule of 1-propanol and its contact area with the

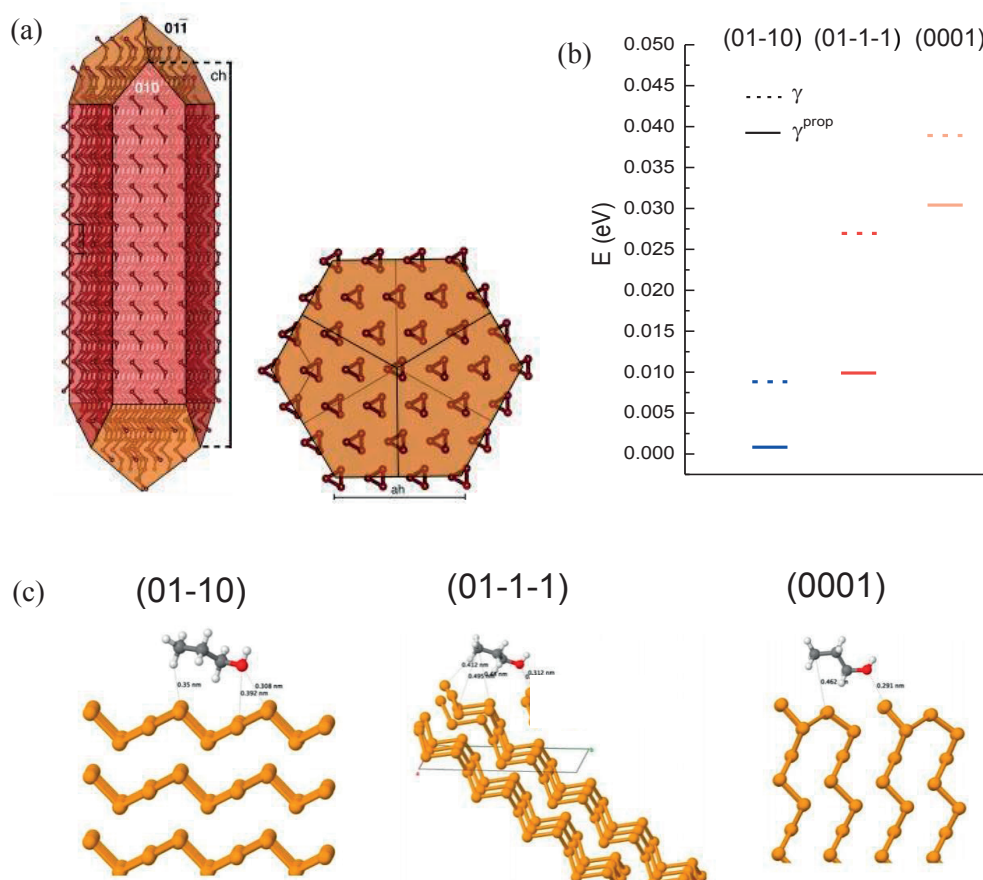


Fig. 4.4. (a) Se crystal shape and definition of ah and ch parameters; (b) surface free energies of (01-10), (01-1-1) and (0001) planes of crystals in contact with 1-propanol molecules or not; (c) one 1-propanol molecule attaching with (01-10), (01-1-1) and (0001) planes.

surface. This (crude) approximation amounts at assuming that the main contribution to the work of adhesion is due to the interaction between the first layer of molecules in propanol and the selenium surface, and that any other long-range interaction, as well as entropic and enthalpic penalties associated with the structuring of the liquid near the surface, cancel out. With these estimations and error bars, we calculate the interfacial free energy between selenium and propanol to be 0.0010 ± 0.0006 , 0.0102 ± 0.0030 , 0.0314 ± 0.0092 eV/Å² for (01-10), (01-1-1), and (0001) respectively (Fig. 4.4b), resulting in a predicted aspect ratio ch/ah of the crystals of about 24. This higher anisotropy due to the effect of solvent would cause a tendency for crystals to grow in the direction of trigonal axis more readily than in any other direction. Since the crystal faces would grow at rates proportional to their respective surface energies from the thermodynamic point of view, this large difference in surface free energy between basal and

prismatic planes results in a strong tendency for the crystals to grow into high aspect ratio nanowires. On the basis of *ab initio* modeling and supported by electron microscope characterization, we can hence propose the following mechanism for nanowire growth in our system: (i) sonication induces and accelerates the nucleation due to the enhanced mobility of Se atoms; (ii) Se atoms dissolved in the solvent are more energetically favored to attach to crystalline nuclei; (iii) nuclei readily grow into high aspect ratio nanowires with trigonal phase along the [001] direction because the solvent exacerbates the anisotropy of surface free energy of prismatic and basal planes; (iv) nanowires grow at the expense of the amorphous matrix[58].

4.3 Optical and optoelectronic characterization on the precursor fiber

Next we investigated the optical response of the nanowire network by measuring the optical absorption and reflection spectra in the visible and near infrared range. Doing such a characterization at the fiber level is impossible because the amorphous Se underneath of the Se nanowire mesh would absorb all incident light. An alternative approach is to synthesize a nanowire mesh with the same thickness as the mesh at the fiber tip on microscope slides and to evaluate its optical absorption. Therefore, we deposited a certain amount of amorphous Se thin film on glass slides before it was treated via the same solution-based approach that was used to grow nanowires at the fiber tip. As shown in Fig. 4.5a, a $\sim 2.9\ \mu\text{m}$ amorphous film does not completely transform into nanowires in 5 or 10 days' soaking in 1-propanol, and the thickness of the remaining Se is $\sim 2.4\ \mu\text{m}$ for both of them. The transmission and reflectance of the nanowires were measured by an integrating sphere between 400 and 830 nm. The absorbance and reflectance for this composite structure is $\sim 90\%$ and $\sim 10\%$, respectively, between 400 and 630 nm, which drastically contrasts with flat amorphous Se films (Fig. 4.6). A combination of anti-reflection effect and light trapping in the disordered nanowire structure accounts for this remarkable property. To differentiate absorption between the grown nanowire and in the underlying amorphous film, it is necessary to synthesize a Se nanowire network without a residual amorphous layer. We therefore deposited thinner Se films on microscope slides to allow them to completely transform into nanowires. Fig. 4.5b shows that a $\sim 240\ \text{nm}$ amorphous film completely transforms into nanowires, but the corresponding absorbance (Fig. 4.6) is lower than that of the $\sim 2.9\ \mu\text{m}$ film in Fig. 4.5a. We then deposited thicker film on the glass. Fig. 4.5 c shows a $\sim 430\ \text{nm}$ amorphous film completely grows into nanowires and the absorbance is almost the same compared to the $\sim 2.9\ \mu\text{m}$ sample between 400 and 630 nm, indicating that optical absorption happens in the nanowire network alone in this wavelength range. We can then assume

that fiber-integrated nanowire meshes have a depth of around 500 nm and that absorption is very strong, above 90% in the visible.

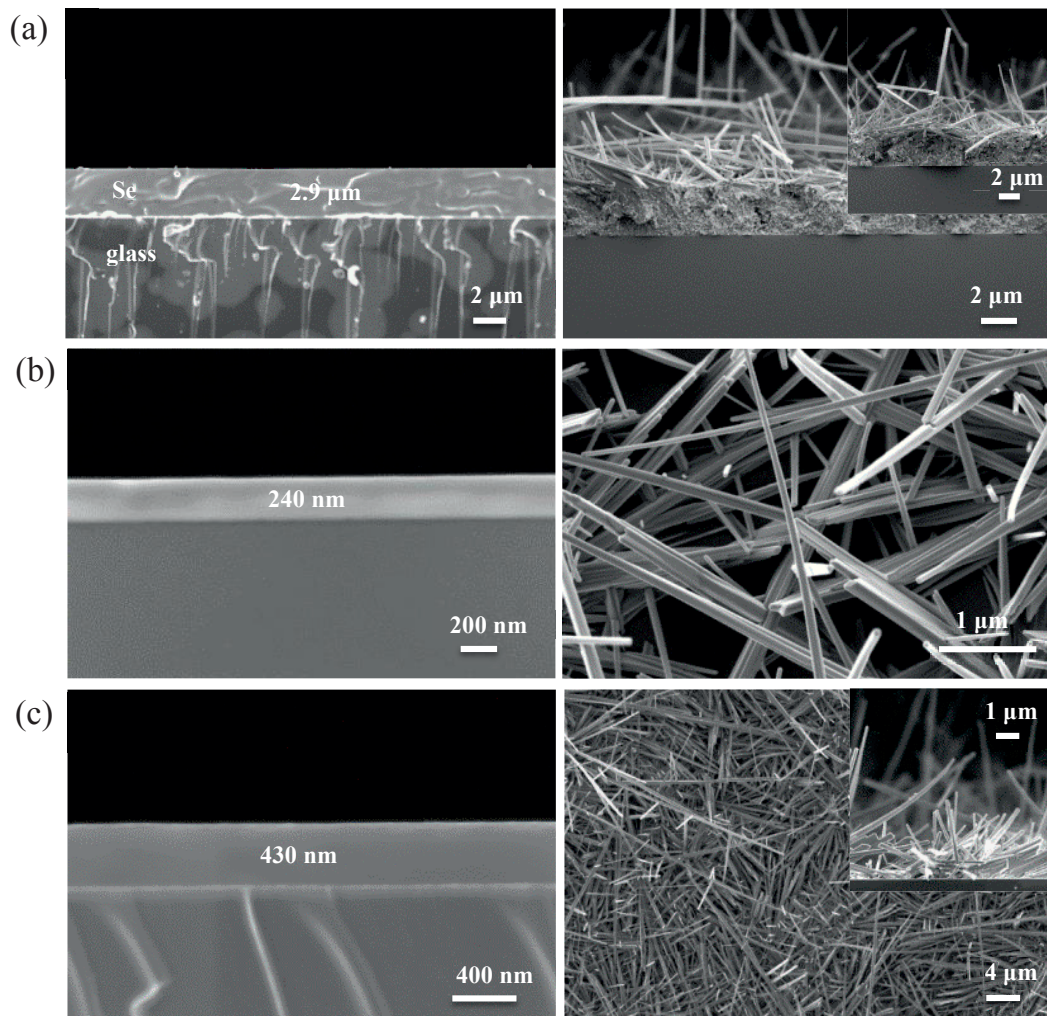


Fig. 4.5. (a) left: SEM cross-section micrograph of a $\sim 2.9 \mu\text{m}$ amorphous film deposited on a microscope slide; right: SEM top view micrograph of its nanowires formation after the sample was soaked in 1-propanol for 5 days and 10 days (insert); (b) left: SEM cross-section micrograph of a $\sim 240 \text{ nm}$ amorphous film; right: SEM top view micrograph of its nanowire growth; (c) left: SEM cross-section micrograph of a $\sim 430 \text{ nm}$ amorphous film; right: SEM top view micrograph of its nanowire growth and the insert is the SEM cross-section micrograph.

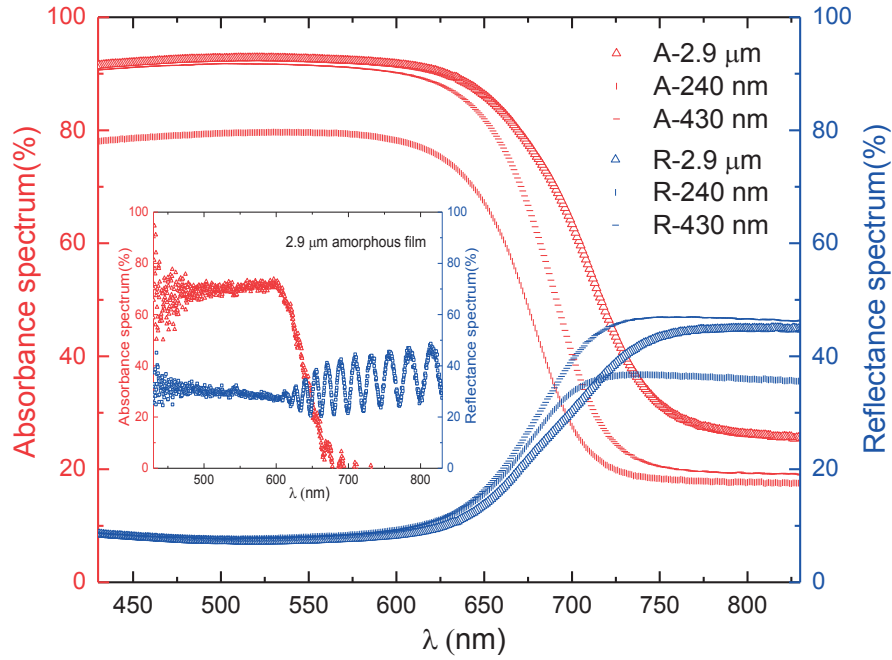


Fig. 4.6. Visible-infrared absorbance and reflectance spectra of three samples described in Fig. 4.5 as well as 2.9 μm amorphous Se film.

Such a thin photoconductive domain is promising as it exhibits low dark current and associated noise, while can provide excellent responsivity. We then characterized the optoelectronic properties of the fiber-embedded semiconducting nanowires shown in Fig. 4.2b, using a supercontinuum-based set up that can provide laser with a wide range of wavelengths. The photocurrent ($I_{\text{ph}} = I_{\text{illuminated}} - I_{\text{dark}}$) was measured for varying wavelengths of illumination, and at different powers. Fig. 4.7a shows the I-V curves of the device irradiated with light power varying from 0 to 100 μW at 532 nm. The conductivity increases by a factor of about 300 from the dark to the illuminated value at 100 μW and 10V. The illumination power-dependent photocurrents under different voltages are plotted in the insert of Fig. 4.7a. The dependence of photocurrent on light power can be fitted to a simple power law dependence, $I = C_1 \times P^{C_2}$, where C_1 and C_2 are frequency dependent constants. For $\lambda = 532$ nm, fitting the curves gives C_2 of 0.486, 0.483 and 0.496 for 2, 5, and 10V, respectively. The non-integer power-law dependence of photocurrent on light power as observed here indicates a complex electron-hole generation, trapping and recombination process by recombination centers and traps. The photoconductance of the device is sensitive to the excitation wavelength, as indicated in Fig. 4.7b. A cut-off wavelength of ca. 729 nm that corresponds to a band gap of the nanowire network of 1.70 eV is observed, which

indicates the photosensitivity of the device is rather low for wavelengths longer than 729 nm. The photocurrent decreases when the wavelength increases after the peaking value is because the energy of photons is not high enough to excite the electrons in the valance band to the conduction band. On the other hand, the photocurrent starts to decrease gradually with decreasing wavelength after reaching a maximum at 590 nm. Since the photocurrent at each wavelength was measured at a constant light power, the photon density decreases as the wavelength decreases. Consequently the photo-induced carrier concentration decreases. At very short wavelength photons with high energies can only penetrate on the surface of nanowire where the recombination rate for carrier is much higher than in the bulk. Therefore carriers combine before they can be collected, and thereby generates a very small photocurrent.

The response of the photodetecting fiber device to switching frequency indicates its capability to respond a fast-varying optical excitation, which in in particular important for optical-switch applications. Fig. 4.8a shows the response characteristics of the nanowire-based fiber device to pulses of light irradiation switched at a frequency of 1000 Hz (left), 500 Hz (middle) and 100 Hz (right) when the bias and light intensity is 20 V and $1.6\text{E-}3 \mu\text{W}/\mu\text{m}^2$, respectively. It is apparent that the device can work with excellent reproducibility and stability in a wide frequency range. Even when the switching frequency reaches to 1000 Hz, the $(I_{\text{max}}-I_{\text{min}})/I_{\text{max}}$ of the device is above 80%, demonstrating a high-performance functionality of the device at high frequency.

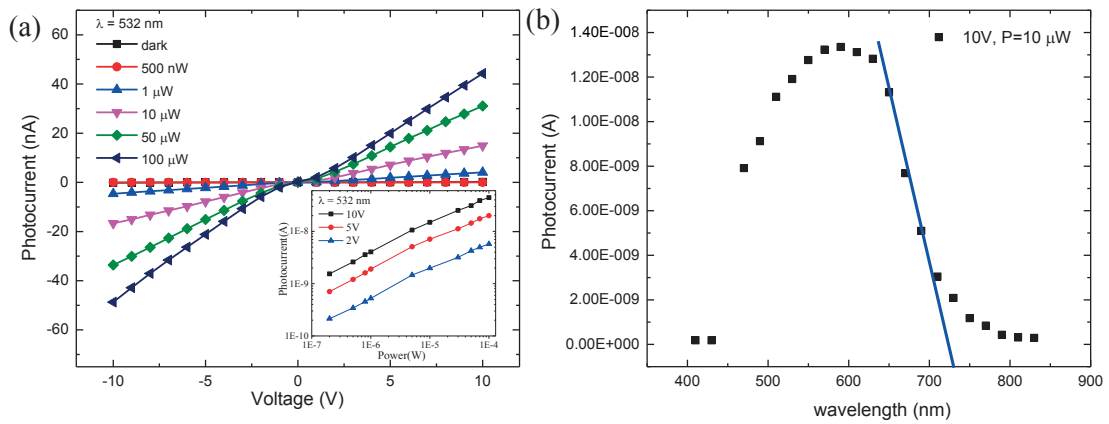


Fig. 4.7 (a) I-V curves of the device versus light power at $\lambda = 532 \text{ nm}$ and the inserted one is photocurrent as a function of power at $\lambda = 532 \text{ nm}$ under different bias voltages; (b) Spectral response of the device at the bias of 10V under 10 μW .

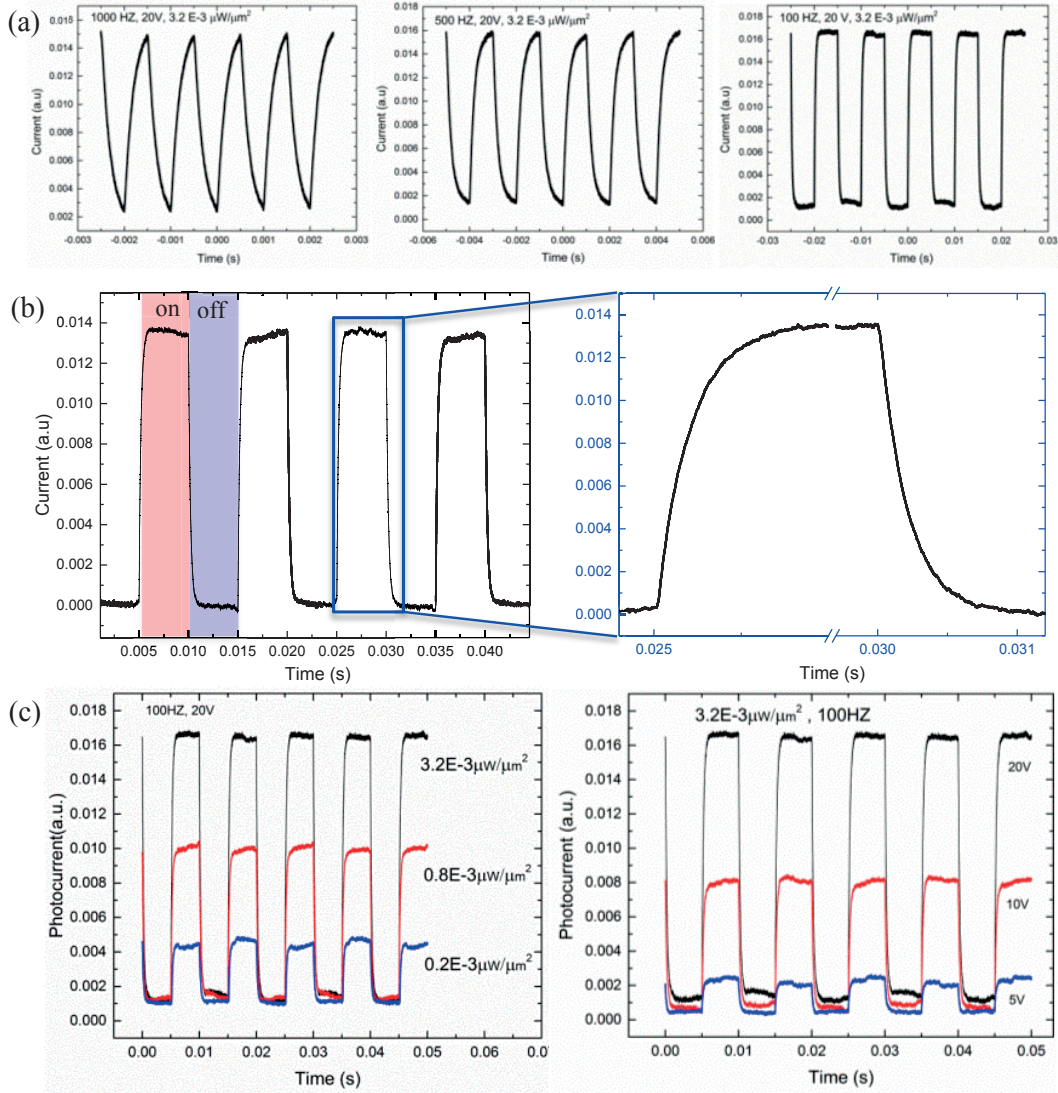


Fig. 4.8. (a) Response characteristics of the nanowire-based fiber device to pulses of light irradiation switched at a frequency of 1000 Hz (left), 500 Hz (middle) and 100 Hz (right) and at 20 V and under $3.2 \text{ E-}3 \text{ } \mu\text{W}/\mu\text{m}^2$ illumination; (b) Photo-switching characteristics of the fiber device under alternating dark and light illumination at the frequency of 100 Hz. The light wavelength and intensity are 520 nm and $1.6 \text{ E-}3 \text{ } \mu\text{W}/\mu\text{m}^2$, respectively. The right panel shows an enlarged view of the temporal current response during on-off illumination switching. Time for the current increasing from 10 % to 90 % of the peak value or vice versa is used for calculating the rise and fall time, respectively; (c) left: response characteristics as a function of illumination intensity at the frequency of 100 Hz and the bias of 20 V; (right): response characteristics as a function of the bias under $3.2 \text{ E-}3 \text{ } \mu\text{W}/\mu\text{m}^2$ illumination and at the frequency of 100 Hz.

Table 4.2 Output characteristics of several recent nanoscale photodetectors. R is the responsivity of the device, VSD is the source-to-drain voltage bias. While a direct and rigorous comparison is not possible since it depends on several parameters (geometry, contacts, power level, bias etc.), the values we give below are an indication that the Se-NW form excellent devices with a combination of high responsivity and fast response speed.

Reference	Material	Configuration	R (A/W)	I_{ph}/I_{dark}	Rise time (ms)	Decay time (ms)	Light source (nm)	V _{SD} (V)
This work	Se	Nanowires	0.058	420	0.00550 (at 2V)	0.00748 (at 2V)	532	10
Advanced Functional Materials [69]	Se	Single Microtube	0.019	32	0.32	23.02	610	5
Advanced Functional Materials [70]	CdSe	Single Nanoribbon			0.639- 11.22	5.68- 34.52	650	
Advanced Materials [71]	Perovskite- graphene	Stacked	1		87	540	520	0.1
Nano Letter [72]	CH ₃ NH ₃ PbI ₃	Nanowire	0.005		0.35	0.25	633	1
Journal of Materials Chemistry C [87]	Sb ₂ Se ₃	Nanowires		150	200	1200		10
Advanced Materials [73]	ZnSe	Horizontal nanowires		1000	70	20	405	30
Small [88]	Graphene		0.0001	1			532	0.1

To determine the response speed of the device, we measured the rise in photocurrent upon turning on the laser light and its decay after removing the incident light under the frequency of 100 Hz, giving a typical rise time of $\tau_{rise} = 0.395$ ms and $\tau_{decay} = 0.445$ ms for the applied voltage of 20 V (Fig. 4.8b), where the rising and falling parts of the curves can be fitted using a single

exponential function. The variation of the rise and decay time with respect to illumination intensity and the bias is negligible, as shown in Fig. 4.8c. The ON-OFF switching behavior was preserved over multiple cycles, indicating the robustness and reproducibility of our devices. The fast rise time in this study is similar to the corresponding values observed in single Se microtube, but the decay time is 50 times faster than their device[69]. Moreover, our device responds much faster than many other nanoscale devices, like perovskite nanowire, perovskite-graphene, ZnSe horizontal nanowires, CdSe single nanoribbon, Sb₂Se₃ nanowires and etc. (Table 4.2). To determine the sensitivity of the device, we measured the noise in the dark (the standard deviation of the current fluctuations around I_{dark}), giving a noise-equivalent power of 3.12 nWHz^{-1/2} for $V = 10\text{V}$, $\lambda = 532\text{ nm}$ and a bandwidth of 1 Hz, which is on par with in-fiber devices demonstrated so far.

4.4 Hybrid fiber making, characterization and application

It is known that interconnections between nanowires impeded charge collection, thereby impairing optical and optoelectronic properties of the device[89]. A simple way to improve device performance would be to decrease the distance between the two electrodes down to the typical length of the nanowires, so that charge carriers could potentially transport along a single nanowire. A straightforward way to realize this is to redraw the precursor fiber. An intriguing feature of thermal drawing approach is that it not only can integrate different building materials into kilometers of fiber devices by a single continuous process, but also can it realize sophisticated fiber architecture with complex functionality. We therefore fabricated the second multi-material fiber (refer to hybrid fiber) that integrates an optical waveguide surrounded by conducting electrodes in contact with two precursor fibers. Fig. 4.9a shows a schematic of thermally drawing of the hybrid preform. The optical waveguide structure consists of poly(methyl methacrylate) (PMMA) and polycarbonate (PC) that have slightly different refractive index. Two Se-based precursor fibers were placed between the conducting CPC ring electrodes in order to redraw them into more miniature yet powerful devices. Two eutectic alloy SnZn electrodes were contacting with CPC, which ensures a good axial electrical conductivity and straightforward electrical contact. More details about this hybrid preform and fiber making can be found in Experimental Methods. The fiber preserves the original cross-section uniformly along tens of meters, as shown in the optical photograph in Fig. 4.9b. The high magnification optical photograph of one of the redrawn Se detectors in Fig. 4.9c depicts the Se is intimately contact with CPC electrodes and the size of it is reduced to $\sim 15\text{ }\mu\text{m}$. Again, the amorphous state

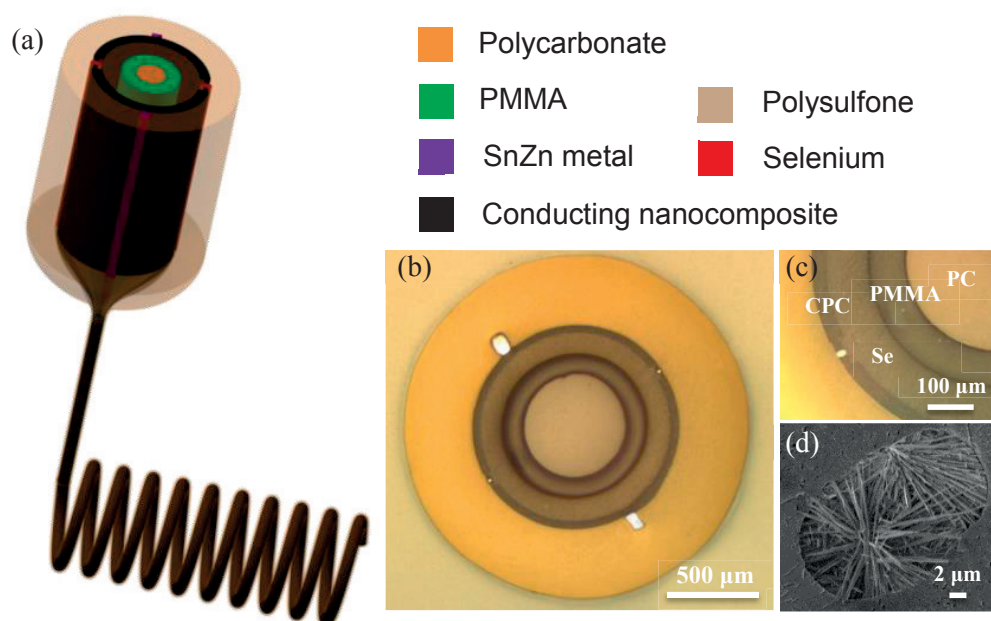


Fig. 4.9. (a) Schematic of the thermal drawing of a hybrid fiber; (b) Optical photograph of the cross-section of the fiber; (c) High magnification photograph of the redrawn Se region; (d) SEM micrograph of Se nanowires grown between the CPC electrodes.

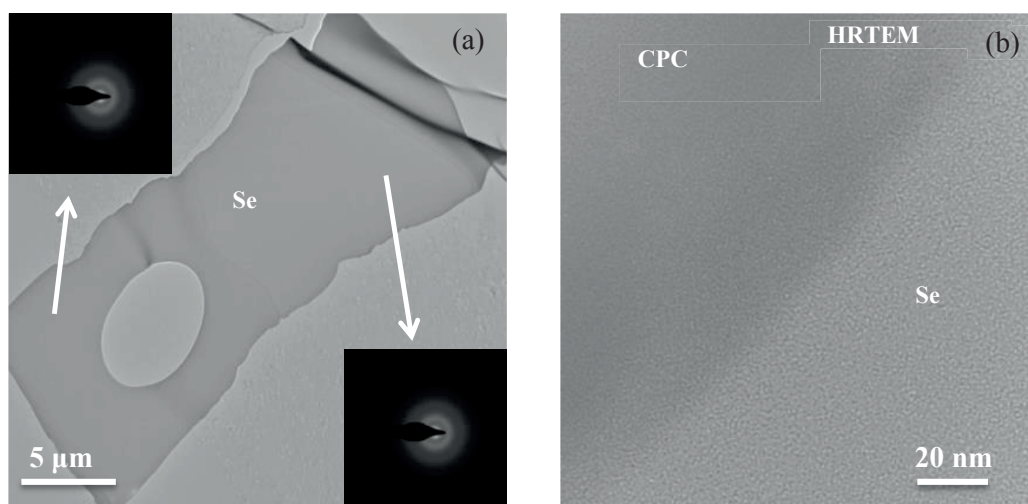


Fig. 4.10. (a) TEM bright-field image of the as-redrawn Se in the hybrid fiber. The insert two images are SAED from two different regions; (b) HRTEM image at the interface between Se and CPC.

of Se in the as-drawn fiber was proved by SAED and HRTEM (Fig. 4.10). The HRTEM further highlights the good interface between CPC and Se. The same solution-based approach employed on the precursor fiber was applied to the hybrid fiber tip, yielding a highly dense array Se nanowire at the fiber tip (Fig. 4.9d). The depth of nanowire mesh is estimated to be around 500 nm (Fig. 4.5).

We then characterize the optoelectronic properties of the hybrid by measuring the current under different power illumination at fixed voltage ($V = 10\text{ V}$) and under monochromatic illumination ($\lambda = 532\text{ nm}$). In order to explore the optoelectronic performance of the hybrid device, two figures of merits, namely photoresponsivity and $I_{\text{ph}}/I_{\text{dark}}$ were characterized as a function of power. As shown in Fig. 4.11 a and b, we compare the photoresponsivity and the ratio $I_{\text{ph}}/I_{\text{dark}}$ measured as a function of power, for the precursor and hybrid fibers before and after nanowire growth. As expected, the as-drawn devices in which the Se remains amorphous exhibit a much lower response, the ones in the hybrid fiber benefiting from the higher electric field due to the reduced electrode distance. As we anticipated, the performance of the nanowire-based hybrid fiber is significantly improved. Specifically, the responsivity reaches 0.06 A/W at a power of 200 nW which is almost an order of magnitude better compared to the previous fiber. It reaches 0.1 A/W at lower powers, which is comparable or even higher than previously reported for in-fiber photodetectors[28][27][33][46]. The $I_{\text{ph}}/I_{\text{dark}}$ ratio also significantly increases, and we measured a noise-equivalent power of $76\text{ pWHz}^{-1/2}$ for $V = 10\text{ V}$, $\lambda = 532\text{ nm}$ and a bandwidth of 1 Hz , an order of magnitude better than for the best reported in-fiber photoconductors[29][28][27][46]. This good optical response comes also with a faster response speed compared to the precursor fiber, with a measured rise time of $5.5\text{ }\mu\text{s}$ and a decay time of $7.4\text{ }\mu\text{s}$ at the applied voltage of 2 V (Fig. 4.11c), on par with the best reported value for thermally drawn fibers[46] and several orders of magnitude faster than for other nanoscale devices (Table 4.2). Combining excellent sensitivity and fast response speed is unprecedented for thermally drawn in-fiber devices, and makes them comparable to some commercial planar photodetectors, opening great opportunities for optoelectronic fibers[58].

The unique combination of efficient optical guidance and high sensitivity capable of nW-level optical power detection endowed for the hybrid fibers allows us to use them as one of the components in a fluorescence imaging system. As shown in the schematic of Fig. 4.11d, when the incident light guided by the optical waveguide core of the hybrid fiber is illuminated on a

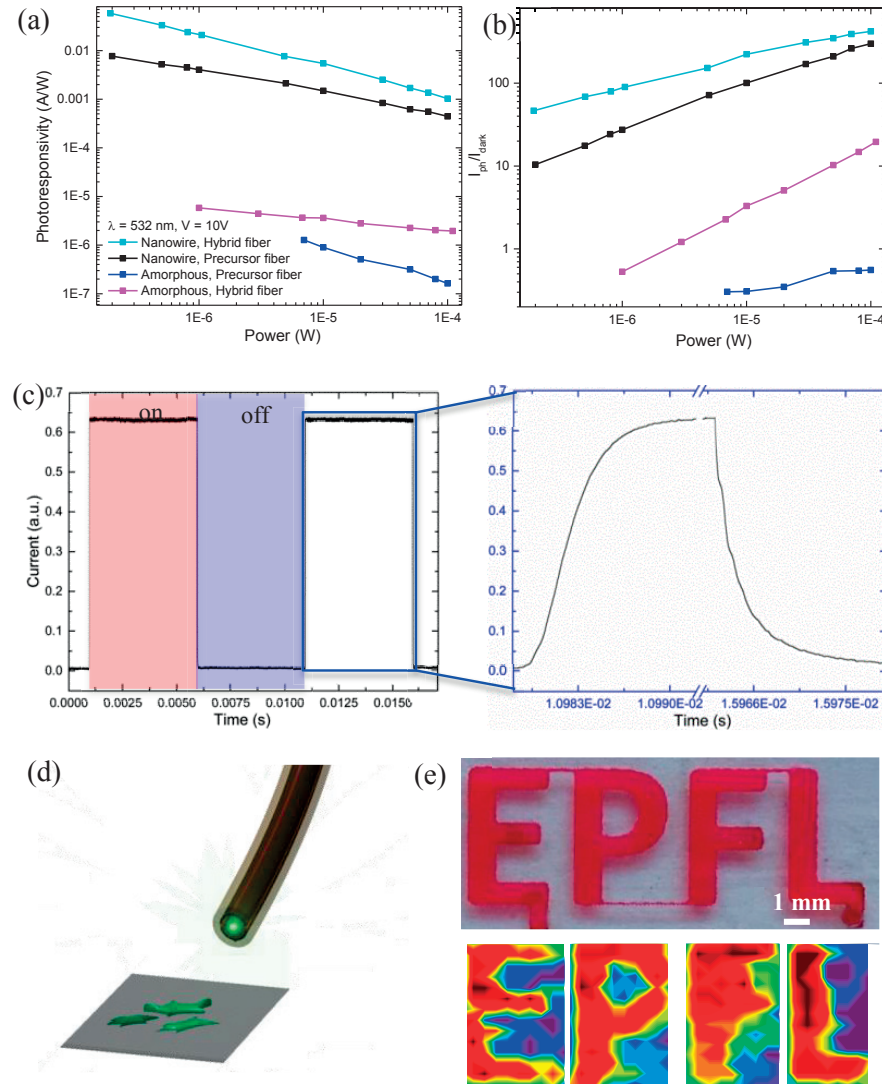


Fig. 4. 11. (a) Comparison of photoresponsivity of amorphous-based and nanowire-based precursor and hybrid fibers; (b) Comparison of ratio I_{ph}/I_{dark} versus power for the same fibers; (c) Photo-switching characteristics of the hybrid fiber device under alternating dark and light illumination at the frequency of 100 Hz. The light wavelength and intensity are 520 nm and $1.6E-3 \mu\text{W}/\mu\text{m}^2$, respectively. The right panel shows an enlarged view of the temporal current response during on-off illumination switching. Time for the current increasing from 10 % to 90 % of the peak value or vice versa is used for calculating the rise and fall time, respectively; (d) Schematic of the fluorescence imaging system; (e) Top: photograph of the “EPFL” logo filled with dye-Rhodamine B dissolved in ethanol (captured with a Vidicon camera); bottom: fluorescent image obtained with the hybrid fiber device.

fluorescent substance, the emission signal can be highly efficiently collected by the nanowire-based detector at the fiber tip, instead of collecting the signal by an optical fibre to be guided to a photodetector at a distal end in the conventional system. By scanning the “EPFL” microfluidic channel filled with Rhodamine B-based solution (Fig. 4. 11e-top) via the hybrid fiber at the incident light of 500-nm wavelength, we recorded the photocurrent at each pixel generated by the 570-nm emission light thanks to the highly photon-sensitive attribute of the nanowire-based device at the fiber tip and can therefore image the logo accurately (Fig. 4. 11e-bottom) based on the variation of current, paving the way towards increasingly complex functional fibers and optical probes.

4.5 Large-area integration of nanowires

An intriguing feature of thermally drawn fibers is the scalability of the approach and their capability of functionalize large surfaces. We then demonstrate our approach not only can be applied at the fiber tip, but also is amenable to the growth of high performance optoelectronic nanowires along the fiber length at arbitrary positions. Fig. 4.12a shows the schematic of thermal drawing of the fiber architecture for nanowire formation along the fiber length. We first embedded a Se domain sandwiched between two CPC electrodes within a PSU plate. This assembly was covered by a sacrificial carbon black filled polyethylene (CPE) layer to ensure encapsulation during the draw (green layer in Fig. 4.12a). The preform was made in the hot press at 220°C. After drawing at 260 °C, thanks to the weak adhesion of the CPE layer on PSU and Se, it could be simply detached via a straightforward mechanical peeling-off process, leaving extended length of fiber with an exposed amorphous Se domain (Fig. 4.12b). Using the same solution-based approach described above, Se nanowires can grow along the fiber length at any prescribed position. A series of optical micrographs are shown in Fig. 4.12c-bottom to highlight a 0.55-cm region of a 15 cm nanowire-based optoelectronic fiber where the Se-NW mesh has grown uniformly. The high magnification SEM micrograph at a typical interface between nanowires and CPC electrodes clearly illustrates how nanowires intimately connect with electrodes. In Fig. 4.12d we show the photoresponsivity at a 15 microWatt power at a wavelength of 532 nm and under a 10V bias versus position of illumination. Clearly, the response is stable along the fiber length highlighting the uniform growth of the nanowire that could be achieved potentially along kilometer of fiber length. Note also that the values of the responsivity are on par with the NW-based devices grown on the fiber tip of the precursor fiber. This simple and

efficient scheme enables ultra-large scale integration nanowires into high-performance optoelectronic devices.

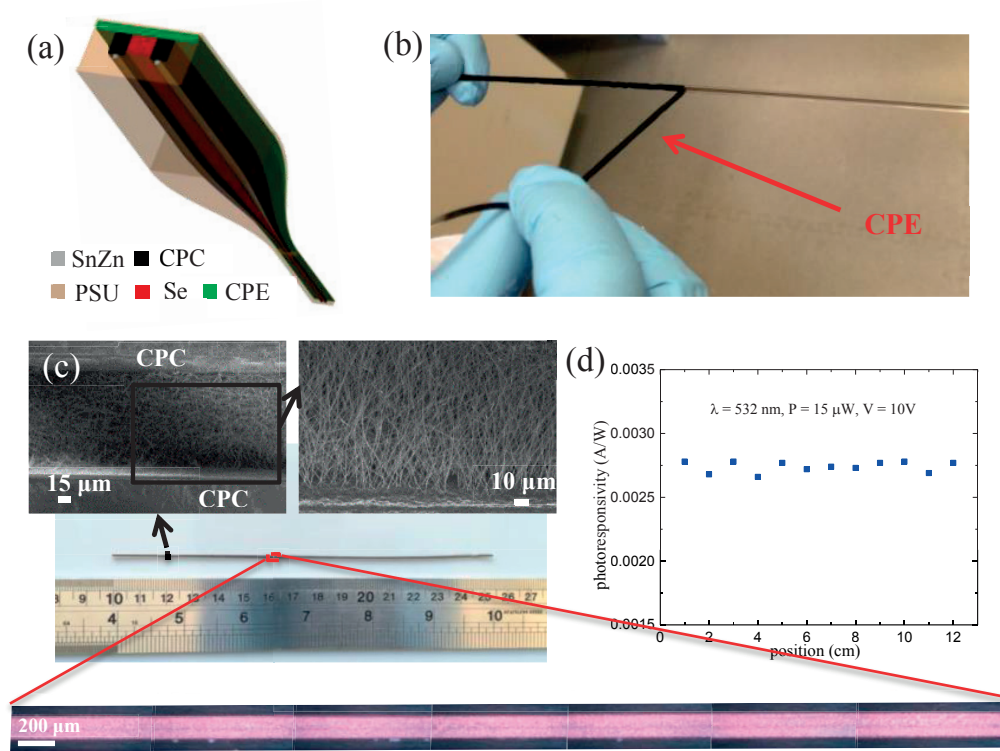


Fig. 4. 12. (a) Schematic of the thermal drawing of a fiber for Se nanowires growth along the fiber length; (b) A photograph of peeling off the sacrificial polymer on the Se; (c) Photograph of a 15 cm-fiber (middle), optical micrograph highlighting the Se nanowire growth in a 1 cm length of the fiber and SEM micrographs showing the Se nanowire mesh and its interface with a CPC electrode; (d) Photoresponsivity of 12 positions in the 15 cm-fiber.

4.6 Discussion and summary

An important field of research in flexible electronics, advanced fiber probes, and smart textiles, is the integration of efficient optoelectronic devices within the unconventional substrate of thin polymer fibers. Since conventional 2D techniques to fabricate semiconductor based devices are not compatible with the fiber size and geometry, it has been very difficult to integrate efficient semiconductor based devices within thin circular fibers. In this chapter we demonstrated the growth of high quality semiconducting nanowires at the tip and along the entire length of polymer fibers via engineering the interfacial energies of the crystal planes in the solvent–1-

propanol. Note that other solvents such as ethanol can also induce this effect. The interfacial energies of crystal planes might vary with the effect of different solvents, resulting in different morphologies of the nanowires. The optical, electrical and optoelectronic performances of the device can hence be optimized. In addition, the soaking time of the fiber in the solvent plays an important role in determining the properties of the device. The depth of the nanowire mesh is very low if the immersion time is not long enough. In this case, the photocurrent is low because photons can penetrate into the bulk amorphous Se that makes little contribution to the optoelectronic performance. When the soaking time reaches 5 days, the nanowire mesh reaches the maximum depth (around 500 nm). More soaking time does not change the nanowire mesh depth. With such an optimal depth, the device exhibits the best photon response (~90% absorbance and ~10% reflectance) as well as the combination of the highest photocurrent and high photosensitivity (I_{ph}/I_{dark} ratio), for the wavelength used in this work.

The interface between the nanowires and the electrodes is critical to the performance of the device. In our system, the nanowires simultaneously interface with the built-in electrodes when they are growing. Given the high photoresponsivity obtained, we can assume a high-quality contact formed that enables both good charge injection and extraction at the interface. The linear I-V curve implies a good ohmic contact between nanowires and electrodes that is very critical to the device photodetecting application because the presence of a Schottky barrier is detrimental to charge injection. On the other hand, our approach could also be amenable to Schottky junction integration by replacing CPC electrodes with other electrodes toward energy harvesting application.

The growth mechanism of nanowires from amorphous bulk in the chemical solvent was elucidated via electron microscope technique as well as first-principle simulations. Miniaturizing the device enhances the optoelectronic performance, featuring high photoresponsivity and photosensitivity, low dark currents, low noise-equivalent power and ultrafast response speed. Most strikingly, this new approach facilitates high throughput and ultra-large area integration of selenium nanowires into devices without the need for complex contacting procedure in the cleaning room, demonstrated by the growth of high performance optoelectronic nanowire-based devices along the fiber length. Furthermore, we have demonstrated the unique capability of our hybrid fiber for fluorescent imaging based on single fiber exhibiting simultaneous efficient optical guidance and superior optoelectronic performance. Possible further applications of this newly designed fiber structure may include remote optical communication systems, detection of

weak signals and in formerly unreachable areas, and optoelectronic probes, minimally invasive in situ and in vivo bio-compatible probing and imaging of biological tissues, as well as large area, flexible optoelectronics and energy harvesting systems.

4.7 Experimental methods

All the SEM samples were coated with 10 nm carbon film. The SEM images were taken with the Zeiss Merlin field emission SEM (Zeiss, Göttingen, Germany) equipped with a GEMINI II column operating at 2.0 kV with a probe current 150 pA. The In-Lens annular detector allowed for high resolution secondary electrons imaging at all magnifications. Transmission electron microscope (TEM) samples were prepared by embedding them in epoxy resin followed by sectioning thin slices (60 nm) using ultramicrotomy (diamond grade) which were transferred on a carbon/Cu grid supports (300 Mesh). The TEM images and selected area electron diffraction (SAED) were taken using talos F200X operating at 200 kV.

The electrical and photoresponse characteristics of the two types of devices were measured using a Keithley 6517B under dark and illuminated conditions. SuperK Extreme (S/N: 14390105) from NKT Photonics having different wavelengths between 410 and 830 nm and optical powers were utilized as light sources. The optical laser power was adjusted using an afocal lens system and was measured using a laser power meter (Thorlabs PM 100D). Time resolved responses of the devices were measured using a pulsed LED with the frequency of 100 HZ, and an oscilloscope was used to monitor the variation of current with time. All measurements were performed in air and at room temperature.

The microfluidic “EPFL” logo channel was fabricated in poly(dimethyl siloxane) (PDMS) using standard soft lithography. Dye-Rhodamine B (Sigma)/ethanol solution (concentration: 0.07 mg dissolved in 5 mL ethanol) was injected into the channel. We used this concentration is because emitted light from this dye solution generates the highest photocurrent detected by the nanowire-based device. A ~10 cm hybrid fiber was used to guide the incident light generated from the SuperK Extreme (S/N: 14390105). The fiber was mounted in a configuration in which the fiber axis having 30 ° with the horizontal surface of the PDMS channel. Most of the reflected incident light from the dye solution can therefore be avoided to be detected by the fiber. The incident laser was set at 500-nm wavelength. The emitted light from the dye solution was 570-nm wavelength which is the excitation peak of dye-Rhodamine B in ethanol.

Chapter 5 Metallic Glass Nanostructure-based Multi-material Fibers

In this chapter, I will first describe the motivation of replacing regular conductors in optoelectronic fibers with metallic glasses (MGs). Then the criteria of selecting MGs for co-drawing them with polymer claddings will be discussed. Subsequently, I will first use MG ribbons as an example to demonstrate that the thickness of the MG in fibers can be continuously reduced down to tens of nanometers via iterative thermal drawing. TEM characterization indicates all these in-fiber MGs with varying size remains amorphous after thermal process. However, the crystallization-induced breakup happens when the thickness of the MG reaches around 40 nm. It is likely that this fragmentation can be circumvented by exploiting the nanoscale size effect in crystallization.

Beyond using MGs as electrodes, this approach can also allow us to fabricate more sophisticated fiber architectures, such as MG-rod based fibers, fiber probe with many MG nanowires inside, fiber metamaterial with an alternating structure of MG and PEI, and MG hollow core fiber waveguide. More strikingly, the in-fiber MGs with varying size exhibit the same electrical conductivity as that of the raw material. I will then show a nanowire-based optoelectronic fiber in which MGs acting as high-performance electrodes contact with semiconducting nanowires. This simple approach also provides a unique platform for making nanoscale MG samples with high geometric perfection, enabling the investigation on the nanoscale size effect in crystallization via in-situ heating in a TEM. Finally, I will model the capillary instability time of the system to explain why the size of MGs can be repeatedly reduced while keeping continuity along the fiber length without break-up.

5.1 Materials selection

As demonstrated in Chapter 4, reducing bulk materials into nanoscale wires and miniaturizing in-fiber active domain can significantly improve the performances of the device. A simple way to minimize the fiber size is to redraw previous fibers. However, a big challenge when redrawing the fiber is that the conductive component either becomes less conductive or breaks up into small sections. Concerning the former, commercial carbon loaded nanocomposites maintains continuity but loses the percolation network during iterative drawing. Concerning the latter, regular metals in fiber would break up due to the Plateau-Rayleigh instability when the size is reduced to a

critical value. Achieving sub-micron metallic wires in fibers via thermal drawing remains a big challenge so far. Then the question is how to obtain continuous nanoscale conductor in fiber while maintaining the functionalities? This motivates us to replace metallic conductor and conducting nanocomposites with an alternative material. Metallic glass is a good choice due to three reasons: (i) metallic glasses can be thermally processed in the supercooled liquid region because of the low viscosity; (ii) metallic glasses may be stretched into nano-size because the superplasticity in the supercooled liquid region that allows a thermal flow behavior similar to polymers; (iii) metallic glasses still owns a good electrical conductivity at small scale and are not susceptible to oxidation. For example, the electrical resistivity of nano Pd-based metallic glass film is $10^{-5} \Omega \text{ cm}$ [90]. Among all existing metallic glasses alloys, Pt_{57.5}Cu_{14.7}Ni_{5.3}P_{22.5} is very promising to co-draw with thermoplastic polymers owing to the following reasons:

1. Compared to other compositions, this alloy is more sluggish with a long crystallization time in the supercooled liquid region. Early work shows that the crystallization time is very long, for example it is roughly 3500 s at 260 °C[91]. This time is sufficiently long enough for the polymers to be drawn into fibers at the same temperature before the MG crystallizes.
2. The glass transition temperature ($T_g = 230^\circ\text{C}$ $\Delta T = 75^\circ\text{C}$)[91] is comparable with the T_g of polymers. The high ΔT provides a big processing window where the glass and polymers become soft simultaneously.
3. The viscosity of this alloy is compatible with that of polymers. The viscosity is around 10^7 Pa s at 260 °C[91], the same order of magnitude with the viscosity of polymers at the same processing temperature.
4. It exhibits a very good superplasticity in the supercooled liquid region and is a very mature material which has been processed into a variety of shapes and sizes [92][93].

Among all the thermoplastic polymers, polyetherimide (PEI) is a suitable cladding that can be co-drawn with Pt_{57.5}Cu_{14.7}Ni_{5.3}P_{22.5} alloy because this polymer exhibits comparable glass transition temperature and viscosity at 260°C.

5.1 MG ribbon-based fiber fabrication, characterization and minimal feature size

In order to make MG-based fibers, a macroscopic perform was made first via the hot press method. As schematically shown in Fig. 5.1a, a MG ribbon with the thickness of 70 μm , the

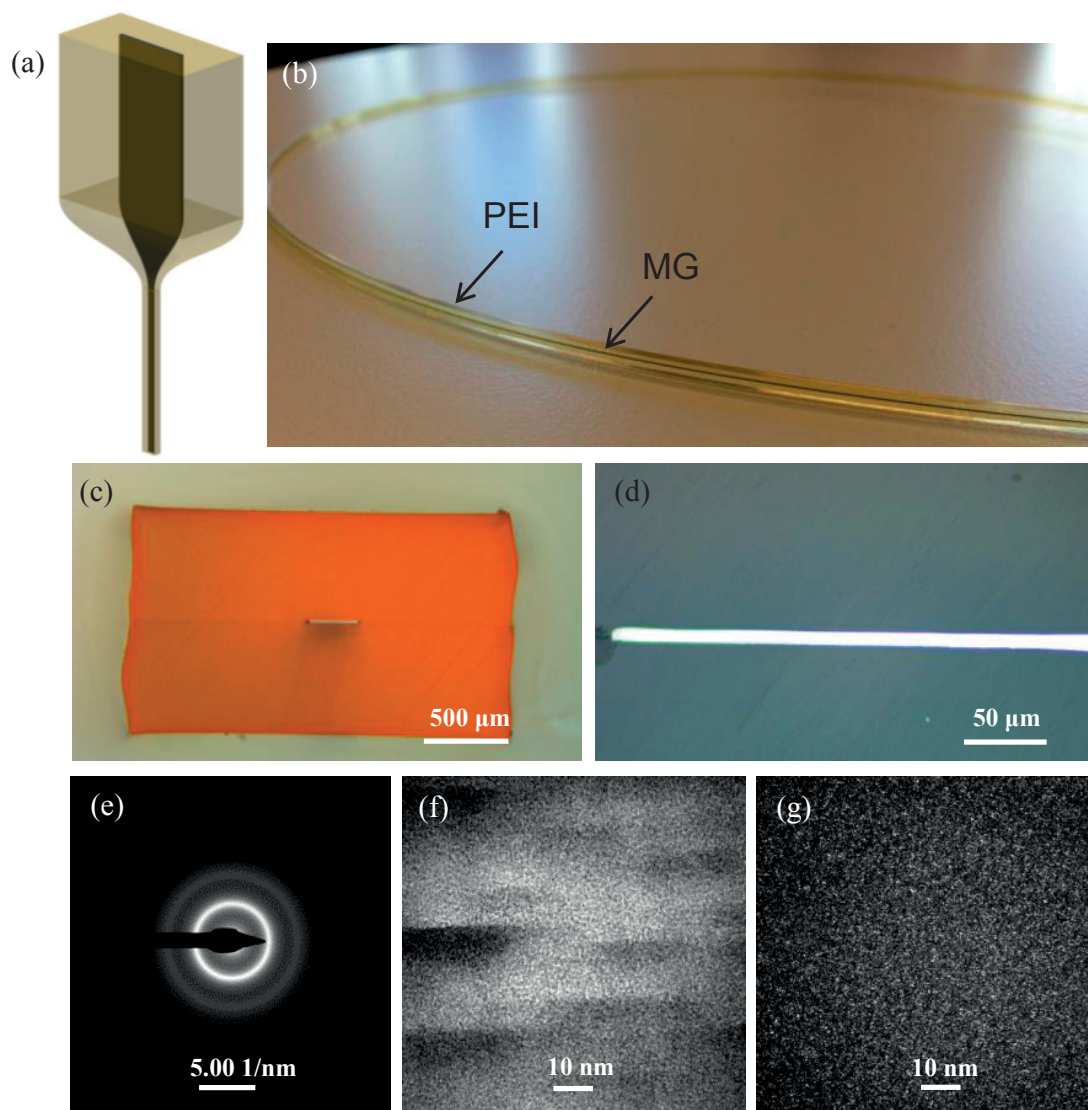


Fig. 5.1 (a) Schematic of thermal drawing of the once-drawn fiber; (b) Photograph of a few meters of fibers in which the PEI and MG is indicated; (c) Optical micrograph of the fiber cross-section; (d) High-magnification optical micrograph of the fiber cross-section; (e) SAED pattern of the MG; (f) Bright-field TEM image obtained by using an objective aperture in the back focal plane to collect the transmitted electrons that contribute to the central spot of the SAED pattern; (g) Dark-field TEM image obtained by using an objective aperture in the back focal plane to collect the diffracted electrons that contribute to the first ring of the SAED pattern.

width of 7.4 mm and the length of 4 cm encapsulated in a PEI plate was thermally drawn into several meters of fibers. The photograph in Fig. 5.1b clearly shows that the MG ribbon is continuous along the fiber length. The whole composite fiber is flexible and lightweight. The

cross sectional optical micrograph in Fig. 5.1c shows that the fiber has exactly the same architecture as the preform. The thickness of the MG was reduced to 8 μm , as shown in the magnified optical micrograph (Fig. 5.1d). We then studied the structure of the MG in the fiber via TEM technique. The SAED pattern indicates the MG in the as-drawn fiber remains amorphous (Fig. 5.1e). No crystalline structure is observed in the bright-field TEM micrograph (Fig. 5.1f). Using an objective aperture in the back focal plane to collect the diffracted electrons that contribute to the first ring of the SAED pattern, dark filed TEM image is taken in Fig. 5.1f that reveals some typical short-range orders and medium-range orders in metallic glasses. Although the MG was thermally drawn in the supercooled liquid region, the dwelling time in the neck-down region (the time it takes for the material to flow from the preform into the fiber) is much shorter than the crystallization time. Thus the MG kept its amorphous nature. We then further miniaturized the thickness of the MG by drawing a piece of the first fiber a second time. We cut a

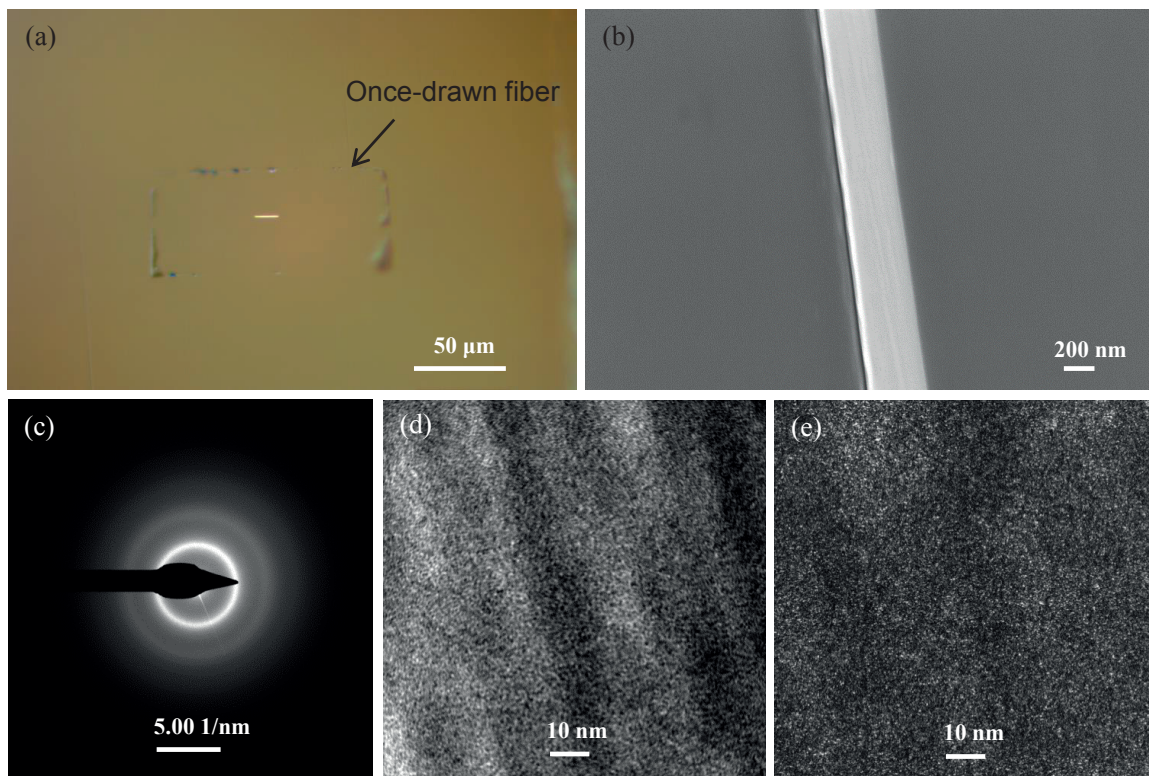


Fig. 5.2 (a) Optical micrograph of the twice-drawn fiber in which the scaled-down once-drawn fiber is indicated; (b) SEM micrograph of the fiber cross-section; (c) SAED pattern of the twice-drawn MG; (d) Bright-field TEM image; (e) Dark-field TEM image.

short piece of the once-drawn fiber and then encapsulated it in a PEI cladding. After consolidation in a hot press, the preform was drawn into tens of meters of fibers (referred to as twice-drawn fibers). The optical micrograph in Fig. 5.2a shows that the scaled-down, once-drawn, fiber can be clearly seen, and the MG has been scaled down by a ratio of 20 again. The SEM micrograph shows that the thickness of the MG has been reduced to 390 nm (Fig. 2.5b) after this second drawing. Again, the SAED, bright-field TEM image and dark-field TEM image demonstrate the MG in the twice-drawn fiber remains amorphous. The drawing step is then repeated a third time to continuously reduce the size of the MG. As shown in the cross sectional SEM micrograph (Fig. 5.3a), the thickness and the width of the MG in the fiber are reduced to 60 and 500 nm, respectively, with a scale-down ratio of 6.5. Fig. 5.3b shows a cross-sectional scanning transmission microscopy high-angle annular dark-field (STEM-HAADF) image of the third-drawn MG in the fiber along with energy-dispersive X-ray spectroscopy (EDX) elemental maps on Pt, Ni, Cu and P, indicating the wire is the MG nanowire in the fiber. Bright-field TEM image (Fig. 5.3c) and SAED pattern (Fig. 5.3d) demonstrate that the MG remains amorphous. It should be noted that the uneven contrast in bright field image can generally be related to variations in the specimen thickness due to the sample preparation. We then study the structure of another third-drawn fiber processed with a scale-down ratio of around 10. The thickness of the MG in this fiber should be, in principle, 40 nm. However, we surprisingly found that the MG ribbon in the fiber breaks up into fragments along the fiber length, as indicated by the optical micrograph in Fig. 5.4a. SAED pattern shows each fragment is crystallized (Fig. 5.4b). Many nanocrystals can be clearly seen from the dark-field TEM micrograph and they are elongated along the fiber drawing direction (Fig. 5.4c). A HRTEM image taken from the broken position (Fig. 5.4d) shows that there are many crystals along the broken area, as indicated by the lattices in the high-magnification HRTEM. This crystallization-induced breakup was also observed in the fiber where the thickness of MG is around 30 nm. The possible reason can be that the crystallization temperature of the MG with the thickness of 40 or 30 nm is significantly reduced due to the nanoscale size effect[94]. Once the size of the MG is reduced to below a critical value in the neck-down region, crystallization starts to happen due to the decrease in crystallization temperature. It seems that the minimal feature size for the in-fiber MG is around 40 nm. According to reference[94], the crystallization temperature for MGs with the size of a few nanometers (e.g. 10 nm) is much higher than that of the bulk due to the size-effect. Therefore, we possibly could beat the crystallization of in-fiber MG and keep the continuity if we draw a thick MG ribbon directly down to a few nanometers, e.g., drawing of 200 nm ribbon to 10 nm with a

scale-down ratio of 20. Thus, we might drive the minimal feature size down to a few nanometers. The work is underway to investigate the structure and the continuity of the 10 nm-MG in the fiber.

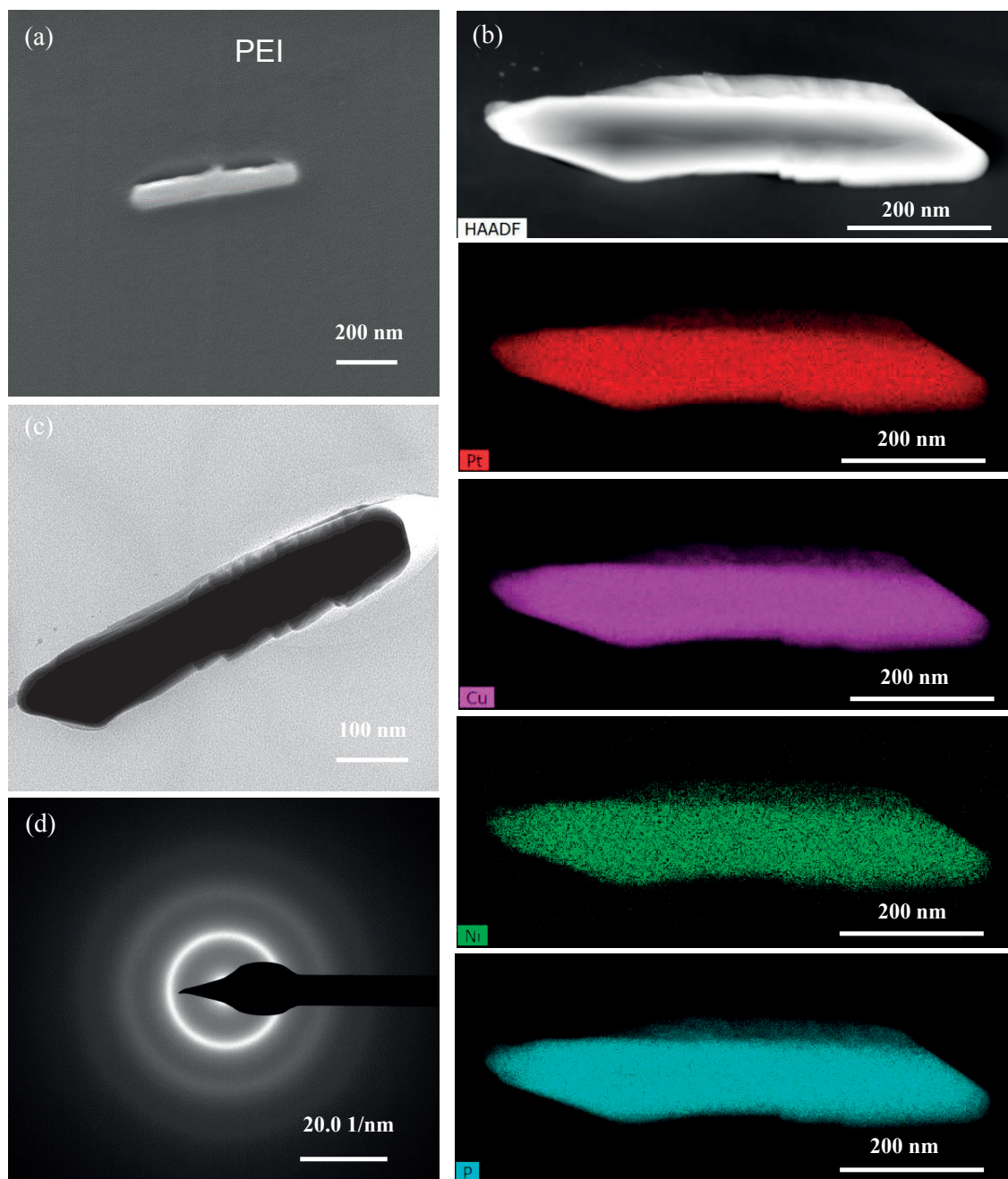


Fig. 5.3 (a) SEM micrograph of the third-drawn fiber cross-section; (b) Cross-sectional STEM-HAADF image and corresponding EDX elemental maps for Pt, Ni, Cu and P; (c) Bright-field TEM image; (d) SAED pattern of the MG nanowire.

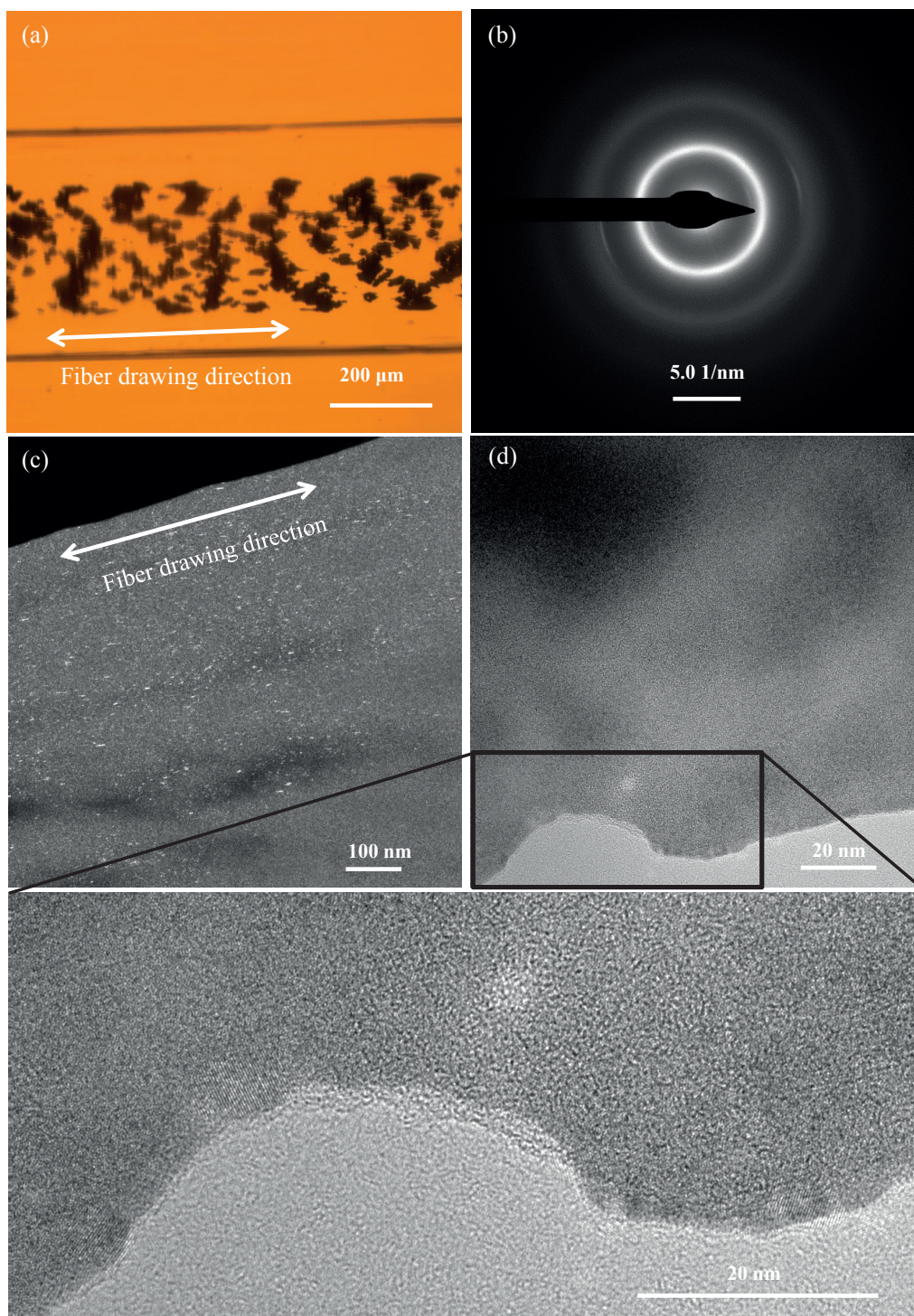


Fig. 5.4 (a) Optical micrograph (in transmission mode) of the broken MG in the fiber; (b) SAED pattern of a broken MG; (c) Dark-field TEM micrograph of the broken MG; (d) HRTEM micrograph of a broken MG along with HRTEM image in the broken region.

5.2 Sophisticated fiber architecture

We then demonstrated that this simple approach can also fabricate fiber –integrated MG with a rod architecture. A first thermal drawing of a MG rod with the diameter of 1.5 mm reduces its size to 293 μm (Fig. 5.5a). Followed by a second drawing, the size is reduced to 33 μm (Fig. 5.5b). Fig. 5.5c shows a single fiber that contains 8 MG nanowires with a diameter of 200 nm indicated by the insert SEM micrograph. Such a nanoelectronic fiber probe paves a novel way towards high-resolution neural interrogation and electrochemical investigation. We then demonstrated more sophisticated fibers can be produced. Fig. 5.5d reveals an alternating structure of PEI and MG. By judicious tuning the thickness of the two components, we could be able to fabricate a fiber metamaterial with a negative refractive index. Further work is underway to target such a novel fiber. Fig. 5.5e displays a fiber architecture in which a MG hollow ring contacting a very thin PEI layer (2 μm) that acts as supporting material surrounded by outmost PEI cladding.

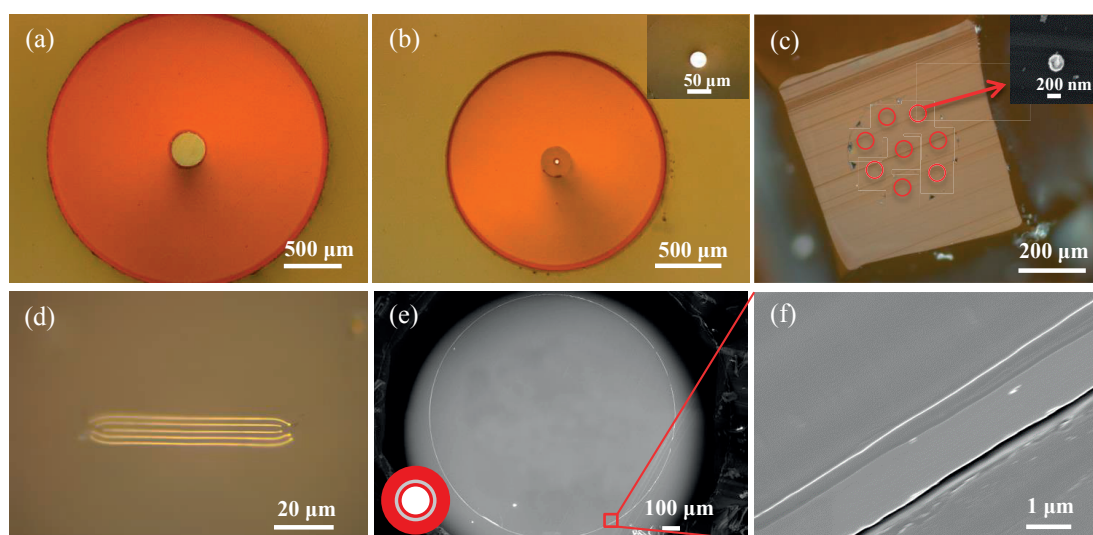


Fig. 5.5 (a) Optical micrograph of a MG rod-based fiber that was drawn once; (b) Optical micrograph of a MG rod-based fiber that was drawn twice and an insert SEM micrograph highlighting the diameter of the MG; (c) Optical micrograph of a fiber containing 8 MG nanowires and an insert SEM micrograph highlighting the diameter of the MG; (d) Optical micrograph of a fiber with an alternating structure of PEI and MG; (e) A MG-based waveguide fiber; (f) High-magnification SEM micrograph indicating the thickness of the MG in the fiber waveguide.

The thickness of the ring is around 1 μm , as indicated by the high-magnification SEM micrograph in Fig. 5.5f. This structure might open up an intriguing opportunity for high power laser transmission in the far infrared region. Further work is also underway to optimize the design and the thickness of each component of the fiber.

5.3 Electrical conductivity and electronic application

When regular metal becomes smaller, it suffers from poor electrical conductivity owing to surface scattering of free charge carriers. The electrical resistivity of a metal increases dramatically when the film thickness is smaller than the mean free path length[95]. The surface roughness and inevitable surface oxidation can further result in surface scattering for carriers, thereby further decreasing the conductivity. In this work, the MG was processed at a high temperature. The oxygen in the PEI cladding inevitably diffuses towards the MG, which particularly becomes more serious when the size of MG is reduced owing to a high surface-to-volume ratio. Therefore, we investigated the electrical conductivity of the MG in all different fibers as well as the bulk MG. We first measured the I-V curve of a raw MG ribbon (Fig. 5.6a), a once-drawn fiber (Fig. 5.6b) and a twice-drawn fiber (Fig. 5.6c) using four-probe method, namely a current was applied to the outer two contacts while a voltage was measured from the inner two contacts. The results show that the electrical resistivity remains the same ($10^{-6} \Omega \text{ m}$) even when the fiber was drawn twice. For another twice-drawn fiber fabricated via a high scaling-down ratio (Fig. 5.6d), only two probes were successfully made due to the extremely small size. The measured resistivity is the same with previous fibers, indicating that the contact resistance can be ignored. In order to successfully make contacts for the third-drawn fiber, we used an original MG ribbon with larger width such that the width in the third-drawn fiber is also larger, making it easier to make electrical contact. The measured resistivity of this third-drawn fiber in which the thickness of the MG is 60 nm is the same with previous fibers. We then conclude that iterative thermal drawing of MG does not impair its electrical conductivity and the MG in the drawn fibers exhibits the same electrical behavior.

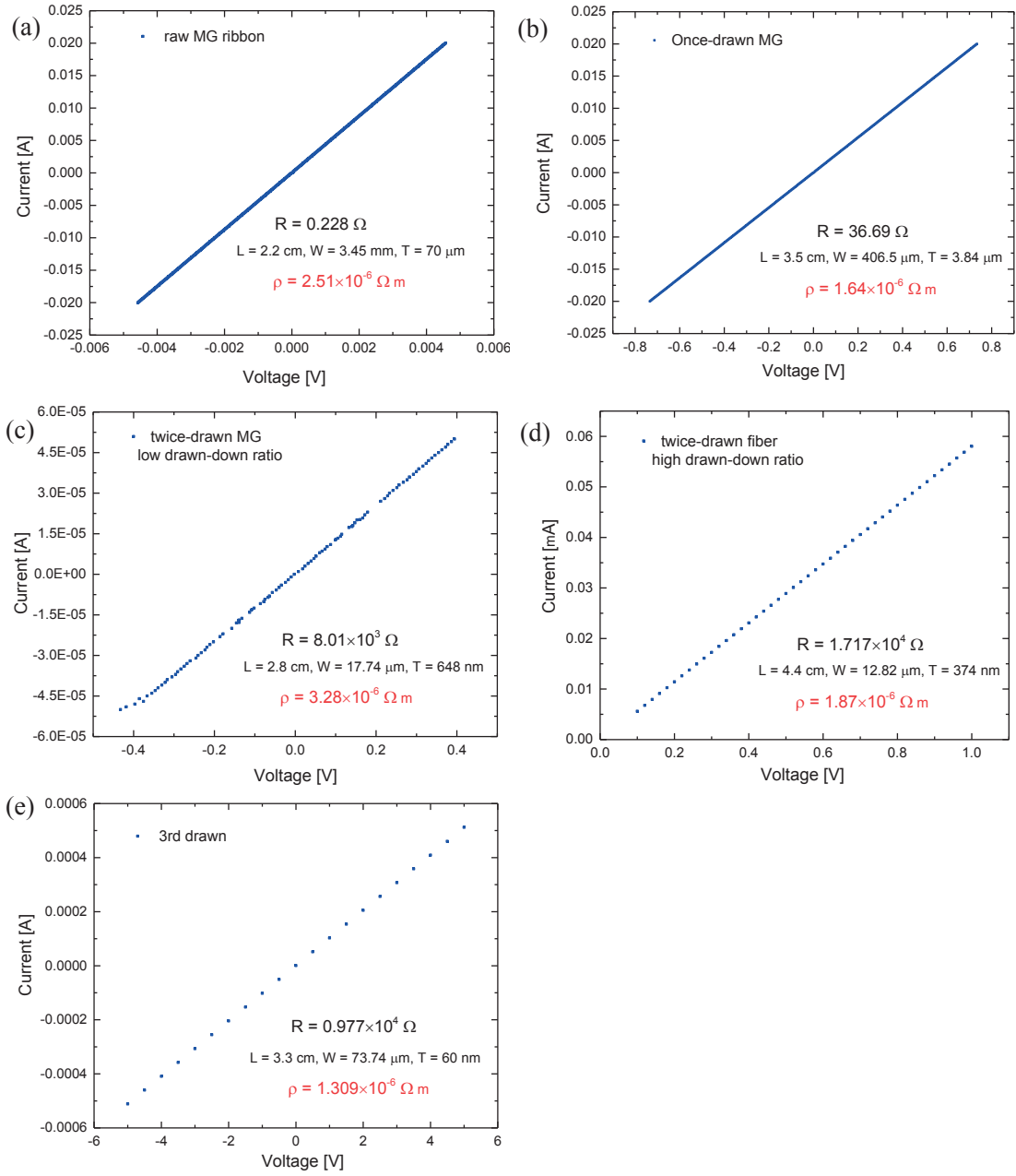


Fig. 5.6 (a-c) Electrical resistivity of a raw MG ribbon, a once-drawn fiber and a twice-drawn fiber measured using four-probe method; (d-e) Electrical resistivity of a twice-drawn fiber fabricated by a high scaling-down ratio and a third-drawn fiber measured using two-probe method.

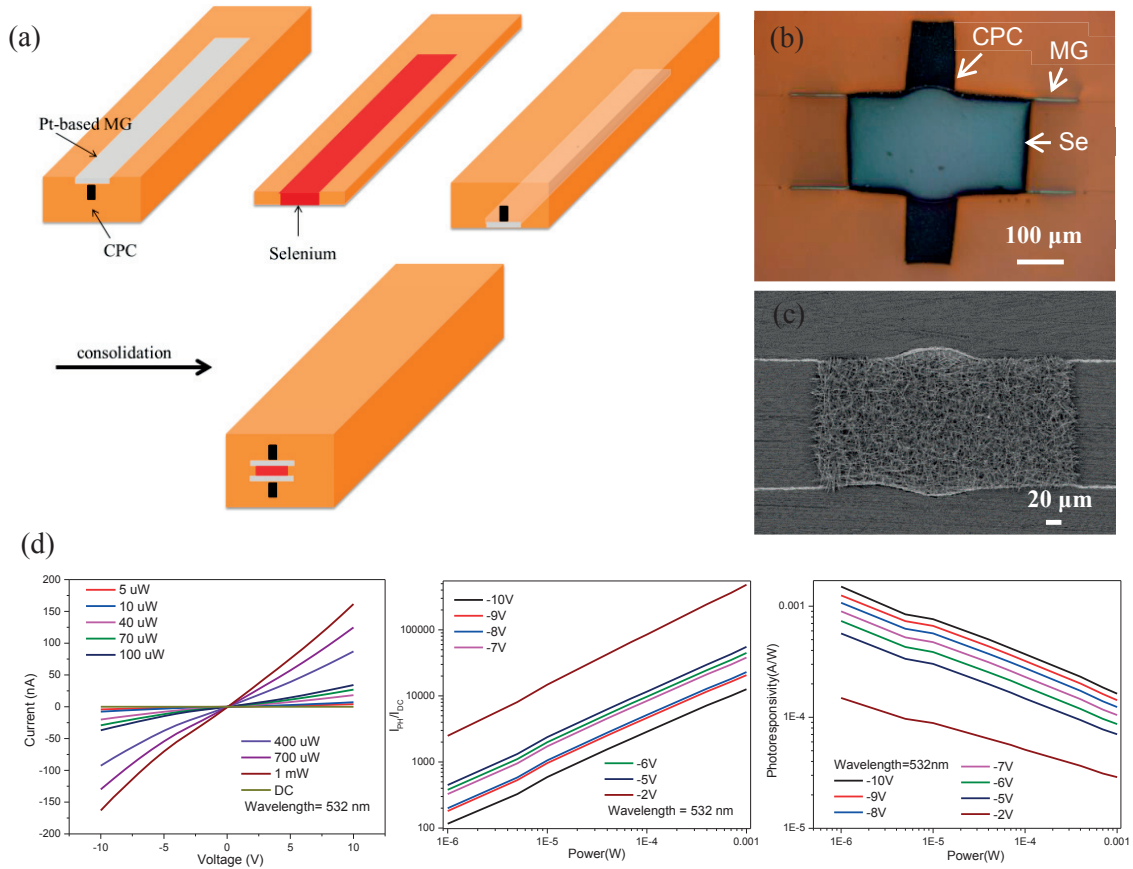


Fig. 5.7 (a) Schematic of a perform making in which MG ribbons act as electrodes; (b) Optical micrograph of the fiber cross-section; (c) SEM micrograph of the fiber cross-section after nanowire growth; (d) I-V curves of the nanowire-based device at fixed wavelength under different power illumination (left), photosensitivity as a function of power of the device at fixed wavelength under different voltages and photoresponsivity as a function of power of the device at fixed wavelength under different voltages.

The electrical conductivity of the MG in fibers is only two orders of magnitude lower than that of typical metal, such as Ag and Cu. This high conductivity allows us to use it as a high-performance conductor in multi-material fibers. As schematically shown in Fig. 5.7a, when use a MG ribbons as an electrode in contact with a semiconducting Se domain. The sandwich structure further interfaced by two CPC electrodes for the convenience of making electrical contacts is encapsulated in a PEI cladding. Optical micrograph in Fig. 5.7b shows the fiber cross-section, revealing the intimate interface between different materials. We then exploited the solution-based approach described in Chapter 4 to the fiber cross-section. A highly dense array of Se nanowires

is synthesized between the MG electrodes (Fig. 5.7c). The optoelectronic properties of the device illustrated by the I-V curves (Fig. 5.7 (left)), photosensitivity (Fig. 5.7 (middle)) and photoresponsivity (Fig. 5.7 (right)) indicate high performances. Specifically, the photoresponsivity is comparable to that of the nanowire-based precursor fiber in Chapter 4 whereas the photosensitivity is several orders of magnitude higher than that of the precursor fiber that exhibits the same electrode distance as current MG-based fiber.

5.4 Nanoscale size effect in crystallization

Bulk metallic glasses exhibit excellent mechanical properties in terms of elastic strain limit, tensile yield strength, Young's modulus, hardness etc., superior to their crystalline counterparts. However, the disordered, microscopically homogeneous and isotropic structure of bulk MGs does not provide a mechanism for work-hardening, namely no dislocation mechanism associated with plastic deformation. Consequently, lacking plasticity, which has been considered the Achilles' heel of these materials, limits their commercial proliferation. However, this intrinsic weakness can be bypassed by using MGs at smaller scales. Size-dependent bending plasticity[96][97], compressive plasticity[98], tensile ductility[99] and thermal stability[94] have been observed. Our approach provides a unique platform to fabricate MG samples straddling a wide range of sizes down to a few nanometers. At such small scales however, we need to take into account the changes in the thermophysical and crystallization behavior of these glasses. The attribute of high geometric perfection endowed by these samples at any scales facilitates the investigation on size effect in crystallization. We hence studied the crystallization behavior of MG samples varying size from micro- to nanoscale via in-situ heating MG ribbons inside a transmission electron microscope. The MG samples were collected by dissolving the PEI cladding. The first sample with the thickness of 50 nm loaded on a TEM chip is shown in Fig. 5.8a. The sample is so thin that the light in the optical microscope can pass through, as indicated by the optical micrograph in Fig. 5.8b in transmission mode. The strip region in the chip is an empty region where the electron beam in transmission electron microscope can also pass through. The TEM sample should be loaded in these regions. Before heating, the bright-field TEM image reveals an amorphous state of the sample (Fig. 5.8c), which is further confirmed by the SAED (Fig. 5.8d). We then heated the 50 nm sample from room temperature to the melting point ($T_m = 500\text{ }^{\circ}\text{C}$) inside the transmission electron microscope. Specifically, the sample was rapidly heated to $170\text{ }^{\circ}\text{C}$ from room temperature in one second. Then a heating with a ramp rate of $40\text{ }^{\circ}\text{C}/\text{min}$ was applied to the sample from 170 to $400\text{ }^{\circ}\text{C}$. Subsequently, the temperature remained at $400\text{ }^{\circ}\text{C}$ for 2.25 mins

before it was raised to 500 °C with a ramp rate of 40 °C/min. The temperature was then kept at 500 °C for 1 min. Finally, the sample was cooled down to room temperature in one second. The whole heating process is displayed in Fig. 5.9a. The structural changes of the 50 nm sample during heating were observed using SAED that were video-recorded in real time (Fig. 5.9b). The initial structure of the sample at 23 °C is amorphous (Fig. 5.9b-1). The second diffusive ring of the SAED pattern starts to become broad at 283 °C, as indicated by the two read marks in Fig. 5.9b-2, implying that crystallization occurs.

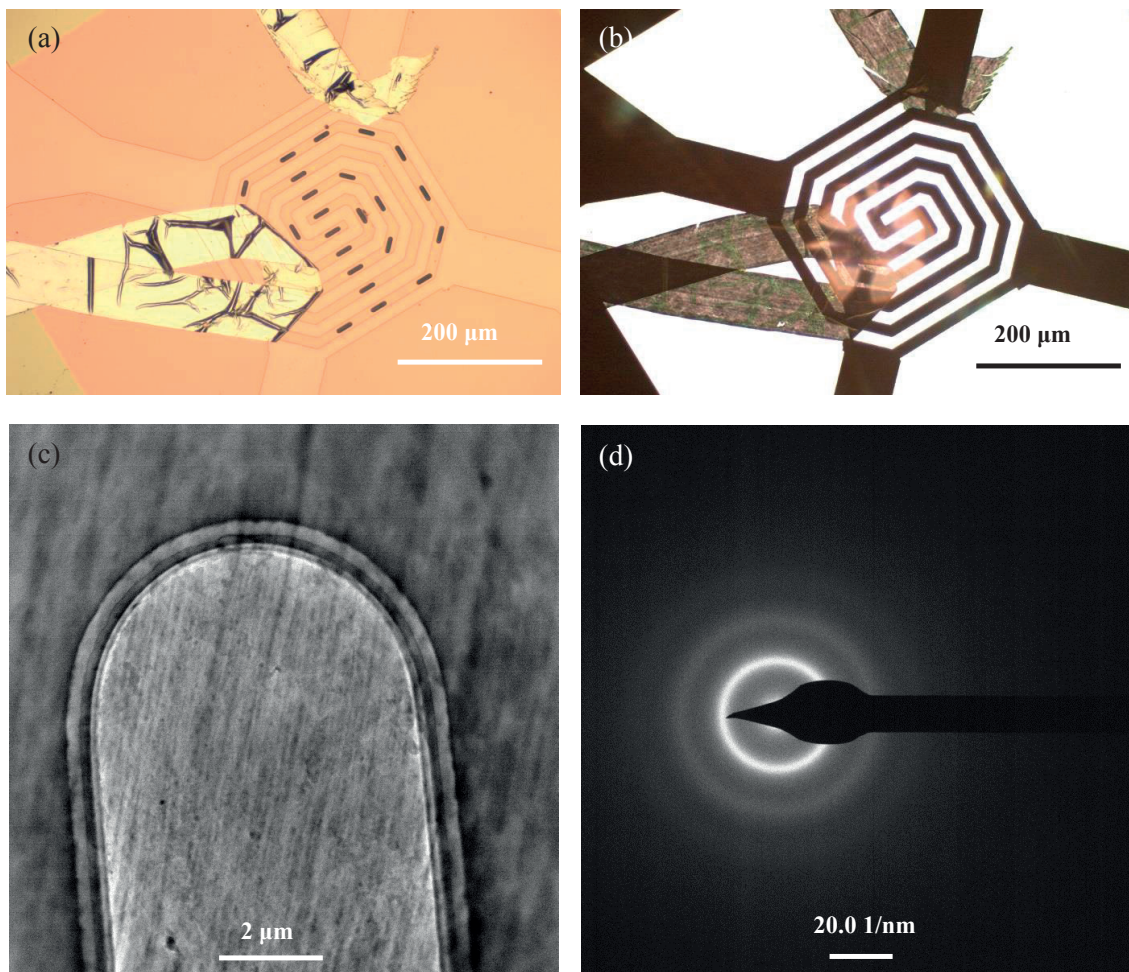


Fig. 5.8 (a) Optical micrograph in reflection mode showing MG ribbons with the thickness of 50 nm was loaded on a TEM chip. The strips are the empty regions where the electron beam can pass through; (b) Optical micrograph in transmission mode; (c) Bright-field TEM micrograph of a MG sample region staying on a strip; (d) SAED pattern of the MG sample before heating.

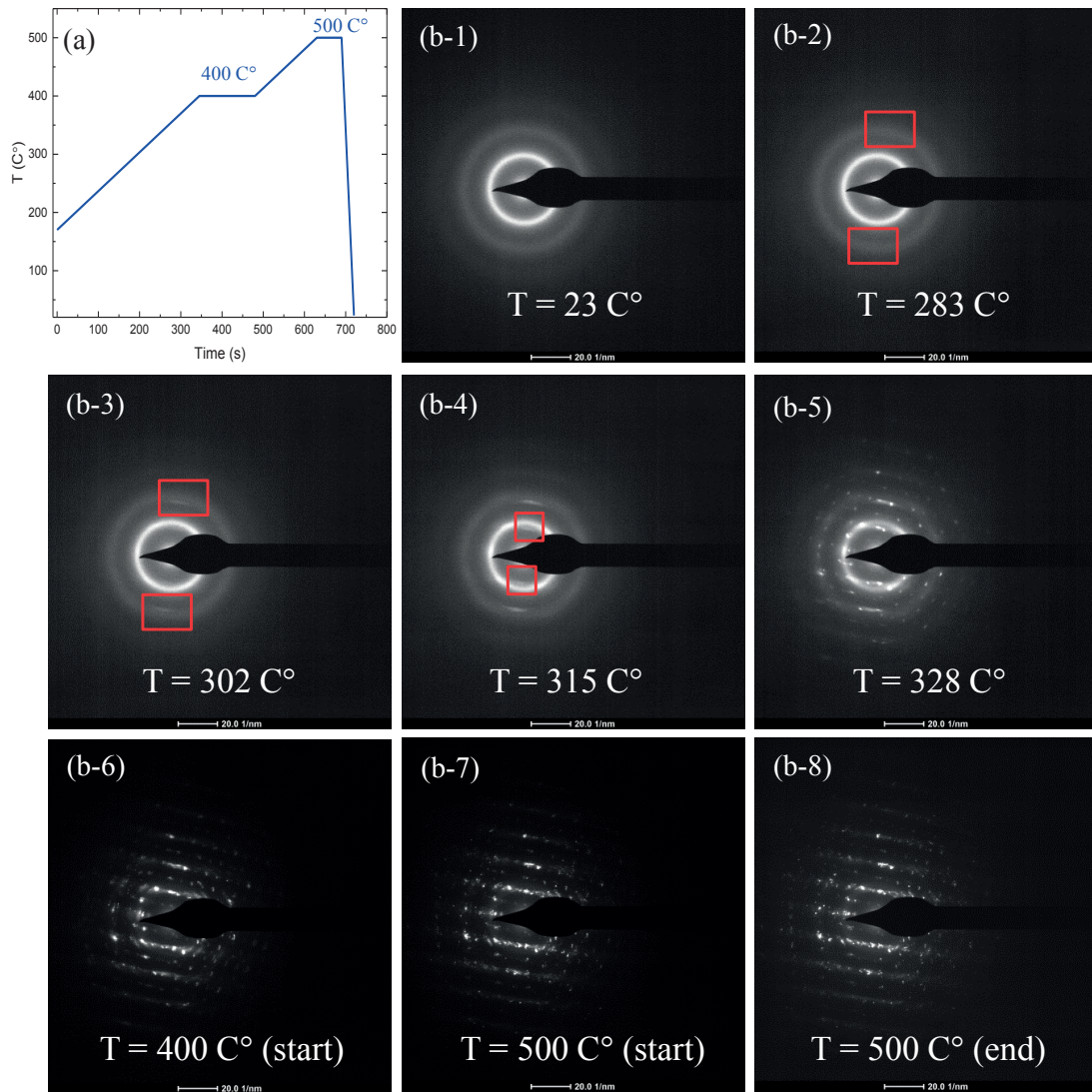


Fig. 5.9 (a) The heating process for the in-situ characterization; (b) Snapshot SAED patterns at different temperatures for the MG ribbon with the thickness of 50 nm.

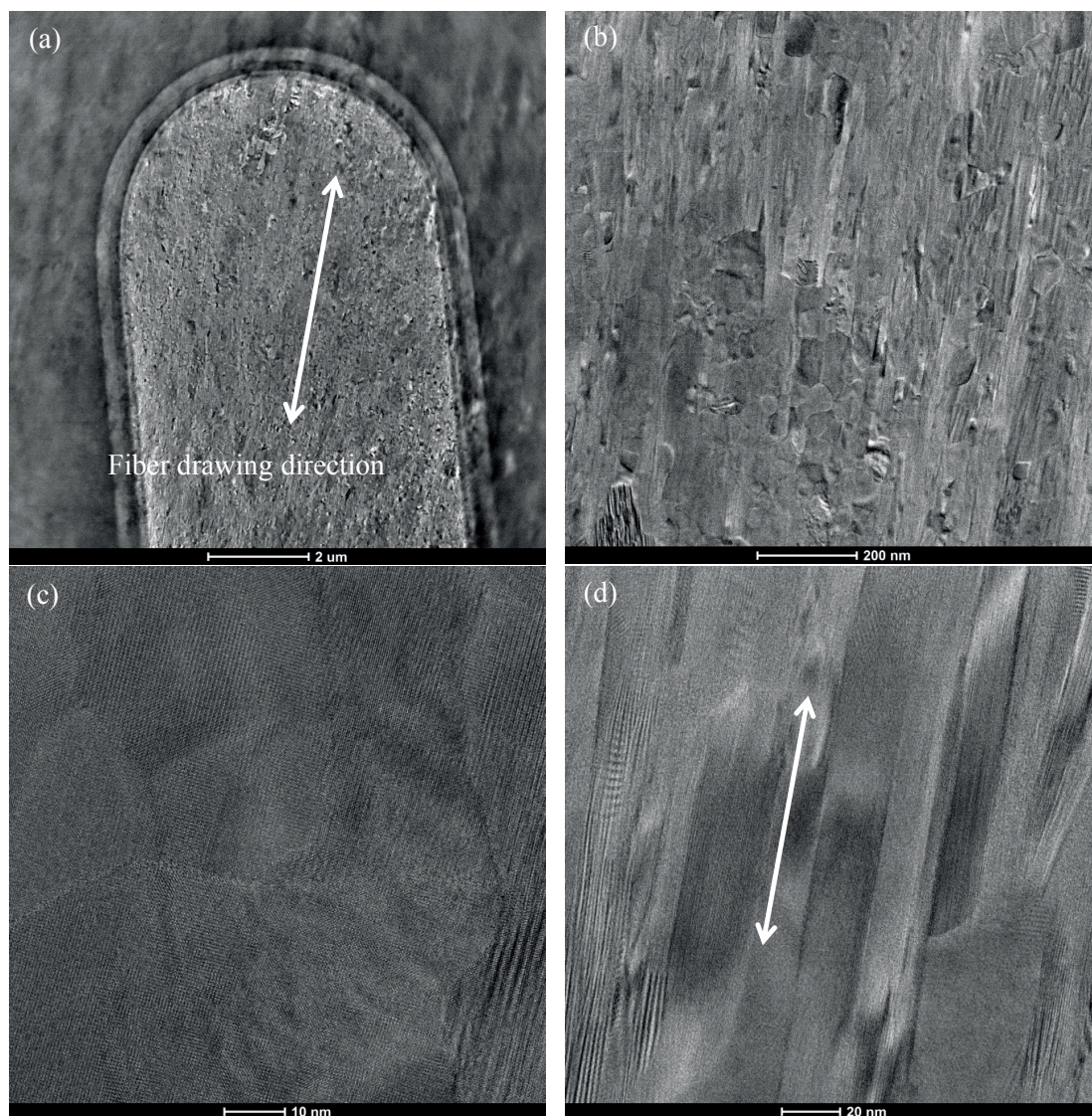


Fig. 5.10 (a) Bright-field TEM micrograph of the same region as that in Fig. 5.7c after in-situ heating. The fiber drawing direction is indicated here; (b) Bright-field TEM micrograph a region to show the polycrystalline structure after heating; (c) HRTEM micrograph of a region showing some regular grains; (d) HRTEM micrograph of a region showing the texture structure along the fiber drawing direction.

The crystallization temperature (around 283 °C) of this 50 nm sample is 20 °C lower than that of the bulk. This widening behavior becomes more obvious at 302 °C (Fig. 5.9b-3). When the temperature is increased more, the first ring becomes broad (Fig. 5.9b-4) due to the textured crystals formation. At 328 °C, diffraction dots appear on the diffusive rings (Fig. 5.9b-5), which

indicates that the material starts to crystallize significantly. The whole crystallization behavior ends at or before 400 °C (Fig. 5.9b-6). Crystallization does not evolve further even when the sample is heated to 500 °C and is maintained at 500 °C for several minutes, as shown in Fig. 5.9b-7 and Fig. 5.9b-8. We then characterized the microstructure of the MG after heating. Fig. 5.10a displays a bright-field TEM image of the same region as the one in Fig. 5.10c and a polycrystalline structure is observed there. The morphology and size of these crystals can be seen more clearly in the high-magnification bright-field TEM image in Fig. 5.10b. A HRTEM image highlights some regular grains with a few tens of nanometers (Fig. 5.10c). Strikingly, we also observed some strip-like grains with the orientation parallel to the fiber drawing direction (Fig. 5.10d).

5.5 Discussion and summary

As discussed in Chapter 4, miniaturizing fiber devices via thermal redrawing can enhance their performances. It requires that all the components in fibers can be continuously scaled down without losing functionalities. This cannot be achieved for a regular metal clad by a polymer in a multi-material fiber where Plateau-Rayleigh instabilities in the form of radial fluctuation happen when the size of a molten metal reduces to a critical value. The instability time scale from the Tomotika model[100] can be written as

$$\tau = \frac{2r\eta_{clad}}{\gamma \max \left[\left(1 - x^2 \right) \Phi \left(x, \eta_{core} / \eta_{clad} \right) \right]} \quad (5.1)$$

where τ is the break-up time scale, r is the radius of the metal core, γ is the surface tension between the cladding and the core metal, η_{clad} , η_{core} are the viscosity of the cladding and metal core, respectively, $x = \frac{2\pi r}{\lambda}$ (λ is the wavelength of a perturbation), Φ is an explicitly known function given in reference[100]. The perturbation with the $\max \left[\left(1 - x^2 \right) \Phi \left(x, \eta_{core} / \eta_{clad} \right) \right]$ will dominate the instability and will lead to breakup. We then take a multi-material fiber that consists of a Sn wire clad by a PSU polymer for example to model the time scale. The term $\left[\left(1 - x^2 \right) \Phi \left(x, \eta_{core} / \eta_{clad} \right) \right]$ is shown in Fig. 5.11a. It shows that the term reaches the maximum

when x is around 0.015 for a typical $\eta_{core}/\eta_{clad} \sim 10^{-8}$. Substituting the maximum $\left[(1-x^2)\Phi(x, \eta_{core}/\eta_{clad}) \right]$ into Equation (5.1) gives

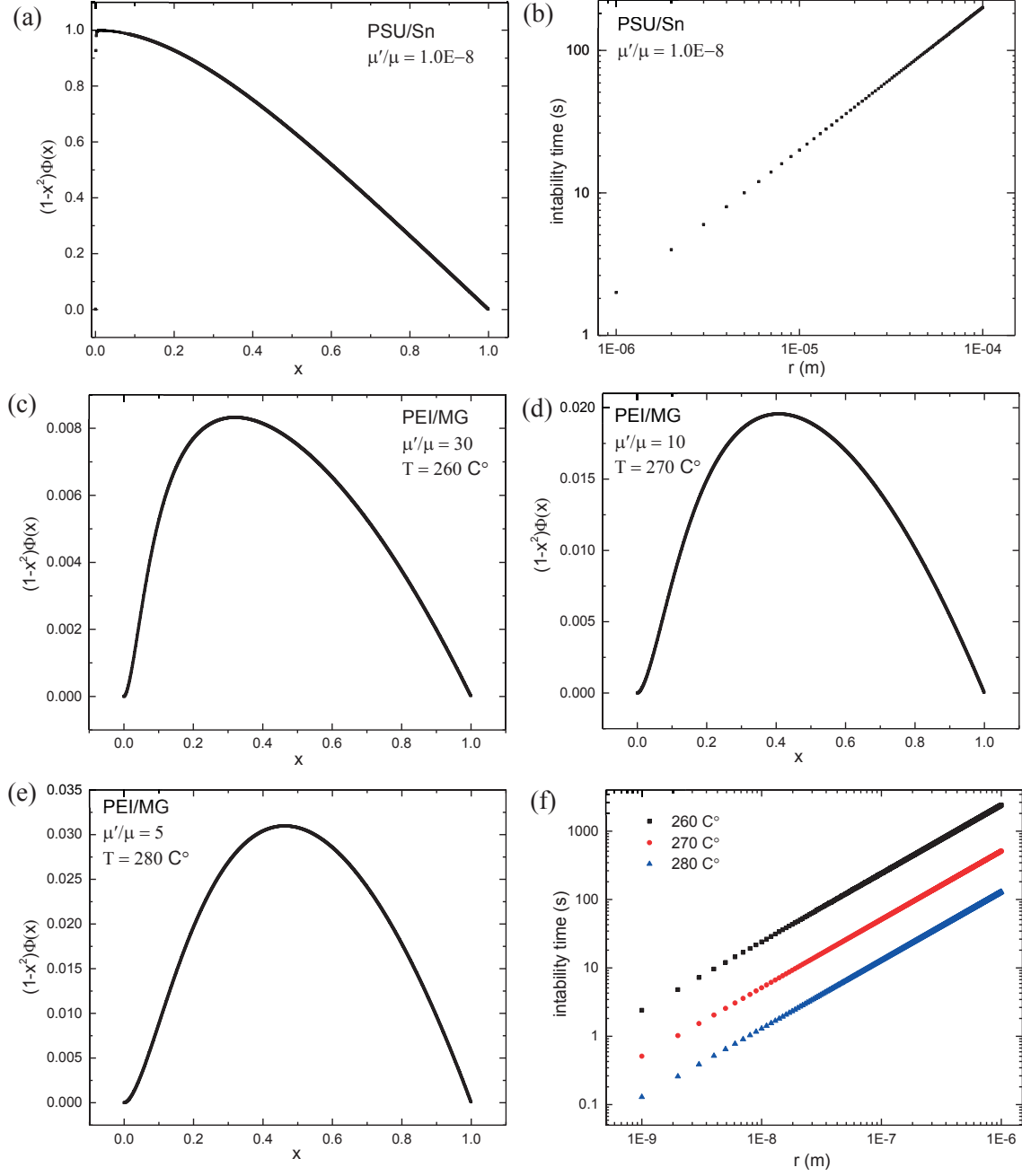


Fig. 5.11 (a) $\left[(1-x^2)\Phi(x, \eta_{core}/\eta_{clad}) \right]$ versus x for PSU/Sn system; (b) Instability time scale versus the core radius; (c-e) $\left[(1-x^2)\Phi(x, \eta_{core}/\eta_{clad}) \right]$ versus x for PEI/MG system at the

temperature of 260, 270 and 280 °C, respectively. η_{clad} and η_{core} are 1E6 and 3E7, 5E5 and 5E6, and 2E5 and 7E5 for 260, 270 and 280 °C, respectively; (f) Instability time scale for the three temperatures.

$$\tau = \frac{2r\eta_{clad}}{\gamma} \quad (5.2)$$

Hence, the instability time versus the diameter of the metal core for the Sn/PSU fiber system is plotted in Fig. 5.11b. It shows that the instability time for a Sn wire with a diameter of 1 μm is around 2 second. This time scale is much shorter than the dwelling time of the material in the neck- down region, which result in the wire breaking up into sections. The submicron metal wire in fibers has never been achieved.

The main reason that the regular metal in fibers breaks up at microscale is that η_{core}/η_{clad} is extremely small (10^{-8}). The typical viscosity of Sn at the melting point is around 10^{-3} Pa·s[101]. For Pt57.5Cu14.7Ni5.3P22.5 MG, the viscosity in the supercooled liquid region is between 10^5 and 10^8 Pa·s[91], leading to a high η_{core}/η_{clad} for MG/PEI system and thereby a long time scale. In Fig. 5.11c, d and e, we plot $\left[(1-x^2)\Phi(x, \eta_{core}/\eta_{clad})\right]$ versus x for temperature $T = 260, 270$ and 280 °C where η_{core}/η_{clad} is 30, 10, 5, respectively. All the curves give an extremum and the maximum $\left[(1-x^2)\Phi(x, \eta_{core}/\eta_{clad})\right]$ increases with increasing temperature. In Fig. 5.11f, we compare the instability time scale for the three typical drawing temperatures of MG/PEI fiber system. It can be seen that lowering the drawing temperature can drastically prolong the instability time scale. The MG wire with the feature size of 10 nm can still remain stable without capillary-induced breakup if the dwelling time in the neck-down region can be controlled in 24 s at 260 °C. A fast drawing speed can definitely achieve this. In addition, the crystallization time for the bulk MG at 260 °C reaches as high as 3500 s. This crystallization time might be longer for the MG with the thickness of 50 nm due to the nanoscale size effect. Although the time to crystallize at each drawing step is additive[102], such a long crystallization time can definitely allow us to process the bulk MG into a few nanometers via a multi-step thermal drawing.

In conclusion, we exploited the highly scalable thermal drawing approach to produce MGs-based multi-material fibers with promising novel architectures and functionalities. The bulk MG

ribbon can be continuously drawn from micrometers to a few tens of nanometers without crystallization-induced breakup or capillary-induced breakup. The crystallization-induced breakup happens when the thickness of the MG reaches around 40 nm. This can be due to the decreased crystallization temperature or shorter crystallization time at nanoscale. Shear or strain induced crystallization should also be considered in further analysis. The fragmentation of the in-fiber MGs might be bypassed if a thick ribbon is directly drawn into a nanoscale in which the MG exhibits enhanced thermal instability, featuring higher crystallization temperature and longer crystallization time. Our modelling work demonstrates that the in-fiber MGs can also maintain continuity without capillary-induced breakup. The scaled down MG ribbons maintains a high electrical conductivity as that of the bulk, which can be exploited to realize high-performance MG-based electronic and optoelectronic devices. We also showed many sophisticated MG-based fibers, paving a novel way toward optical, electronic, magnetic and bioengineering application. This simple approach also provides a unique platform to study the nanoscale size effect in crystallization, enabling fundamental understanding of the physics of MGs.

5.6 Experimental methods

All the SEM samples were coated with 10 nm carbon film. The SEM images were taken with the Zeiss Merlin field emission SEM (Zeiss, Göttingen, Germany) equipped with a GEMINI II column operating at 3.0 kV with a probe current 150 pA. The In-Lens annular detector allowed for high resolution secondary electrons imaging at all magnifications. Transmission electron microscope (TEM) samples for regular characterization were prepared by embedding fibers in epoxy resin followed by sectioning thin slices (60 nm) using ultramicrotomy (diamond grade) which were transferred on a carbon/Cu grid supports (300 Mesh). These TEM images and selected area electron diffraction (SAED) were taken using talos F200X operating at 200 kV. The “Super-X” EDX spectroscopy detector geometry allowed us to acquire chemical maps of the samples. TEM samples for in-situ characterization were prepared by dissolving PEI cladding with N-Methyl-2-Pyrrolidone (NMP) followed by ethanol to remove the residual NMP on the MGs. The released MG samples were loaded on in-situ TEM chips (DENS-D-6-F-1300-T, LOT-QuantumDesign GmbH). The TEM images and selected area electron diffraction (SAED) were taken using the double Cs-corrected, monochromated FEI Titan Themis with a high angle annular dark field (HAADF) detector operating at 300 kV.

Chapter 6 Conclusions and outlook

The integration of electronic and optoelectronic domains within thermally drawn multi-material polymer fibers opens up a wide range of applications. Thus far however, these fiber devices have exhibited limited optical, electronic and optoelectronic performances and poorly developed functionalities. The in-depth understanding of structure–property relationships could open new opportunities for increasingly sophisticated functionalities in fiber devices.

In this PhD work, two annealing approaches were employed to crystallize the amorphous semiconducting core in a multi-material fiber. Regardless of temperature and time, the regular furnace-based method induces a microstructure with nanoscale grains and a large crystallization depth that is hard to control. In contrast, the local laser-based approach induces crystallization in a controlled depth and a microstructure with microscale grains. Furthermore, a multi-step laser annealing allows for a polycrystalline structure with ultra-large grains, controllable crystallization depth and preferential orientation of crystals with the basal plane of (0001) perpendicular to the direction of the electric field planes, exhibiting drastically enhanced optoelectronic performances. The microstructure formation can be understood by the extended heterogeneous nucleation theory that considers the anisotropy of the interfacial energy. The laser annealing approach demonstrated here also has the potential to be applied in the longitudinal direction of the fiber. This would enable the ability to write, at any location along kilometer-long fibers, devices of controlled microstructure and performance.

We have also developed a simple approach for the fabrication of nanowire-based optoelectronic devices within multi-material fibers. The nanowire growth mechanism was elucidated via electron microscopy as well as first-principles calculations. Miniaturizing the device enhances the optoelectronic performance, featuring high photoresponsivity and photosensitivity, low dark currents, low noise-equivalent power and ultrafast response speed, on par with wafer-based devices. Most strikingly, this new approach facilitates high throughput and ultra-large area integration of selenium nanowires into devices without the need for complex contacting procedure in the clean room, demonstrated by the growth of high performance optoelectronic nanowire-based devices along the fiber length. Furthermore, we have demonstrated the unique capability of our hybrid fiber for fluorescent imaging based on single fiber exhibiting simultaneous efficient optical guidance and good optoelectronic performance.

In a final part, we exploited the highly scalable thermal drawing approach to produce MGs-based multi-material fibers towards unique functionalities. The bulk MG ribbon can be continuously drawn from micrometers to a few tens of nanometers in thickness without crystallization-induced breakup or capillary-induced breakup. We established a theoretical framework based on Plateau-Rayleigh capillary instability to explain the continuity of in-fiber MGs. The crystallization-induced breakup happens when the thickness of the MG reaches around 40 nm. This can be due to the decreased crystallization temperature or shorter crystallization time at nanoscale. The fragmentation of the in-fiber MGs might be bypassed if a thick ribbon is directly drawn into a nanoscale in which the MG exhibits enhanced thermal instability, featuring higher crystallization temperature and longer crystallization time. The scaled down MG ribbons remain a high electrical conductivity as that of the bulk, resulting in high-performance MG-based optoelectronic devices. We also showed many sophisticated MG-based fibers, paving a novel way toward optical, electronic, magnetic and bioengineering applications. This simple approach also provides a unique platform to study the nanoscale size effect in crystallization, enabling fundamental understanding of physics in MGs.

Some prospects can be concluded as follows: 1) the interplay between materials structure and properties is just beginning, and is emerging as an exciting field for fundamental and applied research. Tremendous efforts have been put into developing complex functionalities by designing sophisticated fiber architectures. A unique strategy to circumvent complicated design for fiber architecture is to desirably control the microstructure of the semiconductor. Our developed laser annealing approach cannot be only applied to Se, but also is amenable to other fiber semiconductors and geometries. It has the potential to be a universal approach to desirably control the microstructure of in-fiber semiconductors as long as laser parameters, annealing time and step can be judiciously controlled. 2) One-dimensional semiconducting nanowires represent attractive building blocks for electronic and photonic devices. We demonstrate that high-quality single-crystal Se nanowires can be synthesized in the solvent from amorphous bulk at room temperature. Other materials that show anisotropic interfacial-energy can also be investigated. Machine-learning technique can be used to predict the possible materials that are applicable to the sonochemical synthesis. The ability to realize mass fabrication of high-density nanowire-based devices over large scale is still at the center of high interest in semiconducting nanowire community. Our work enables nanowire growth and nanowire integration in a single step without any high-resolution patterning techniques. 3) Increasing the density of optical, electronic and

optoelectronic devices incorporated in a multi-material fiber makes it more functional. We demonstrate the unique functionality of our nanowire-based fiber by the integration of a photodetector that is very sensitive to weak photon illumination with an optical waveguide that efficiently transmits light. More functional domains such as, junctions for photodiodes or photovoltaic configurations, as well as piezoelectric or thermoelectric materials can be incorporated into a single fiber for more complex applications. 4) Incorporation of metallic glasses into multi-material fibers will likely have a significant impact in the field. It allows us to drive the metal-semiconductor-insulator optoelectronic fiber devices towards smaller and smaller scale. The ability to draw MG from the bulk to nanoscale without breakup while maintaining unique properties makes it possible to fabricate more sophisticated fiber architectures for intriguing functionalities. The MG fiber devices for optical waveguide in the infrared range, magnetic resonance, fiber-based metamaterials and neural interrogation with improved spatial resolution are being investigated. In addition, both the crystallization of MGs during thermal drawing either by heat or stress and the nanoscale size effect in crystallization can also offer a novel platform to investigate and understand several interesting topics in materials science.

Bibliography

- [1] B.A. Flusberg, E.D. Cocker, W. Piyawattanametha, J.C. Jung, E.L.M. Cheung, M.J. Schnitzer, Fiber-optic fluorescence imaging., *Nat. Methods.* 2 (2005) 941–50.
- [2] M. Alexander Schmidt, A. Argyros, F. Sorin, Hybrid Optical Fibers - An Innovative Platform for In-Fiber Photonic Devices, *Adv. Opt. Mater.* 4 (2016) 13–36.
- [3] M. Consales, M. Pisco, A. Cusano, Lab-on-fiber technology: a new avenue for optical nanosensors, *Photonic Sensors.* 2 (2012) 289–314.
- [4] G. Kostovski, P.R. Stoddart, A. Mitchell, The optical fiber tip: an inherently light-coupled microscopic platform for micro- and nanotechnologies., *Adv. Mater.* 26 (2014) 3798–820.
- [5] G. Tao, A.M. Stolyarov, A.F. Abouraddy, Multimaterial Fibers, *Int. J. Appl. Glas. Sci.* 3 (2012) 349–368.
- [6] A.F. Abouraddy, M. Bayindir, G. Benoit, S.D. Hart, K. Kuriki, N. Orf, et al., Towards multimaterial multifunctional fibres that see, hear, sense and communicate, 6 (2007) 336–47.
- [7] <http://www.southampton.ac.uk/news/2015/07/researchers-to-test-new-optical-fibre-3d-printing-technique.page>.
- [8] P.J.A. Sazio, A. Amezcua-Correa, C.E. Finlayson, J.R. Hayes, T.J. Scheidemantel, N.F. Baril, et al., Microstructured optical fibers as high-pressure microfluidic reactors., *Science.* 311 (2006) 1583–6.
- [9] A.C. Peacock, U.J. Gibson, J. Ballato, Silicon optical fibres – past, present, and future, *Adv. Phys. X.* 1 (2016) 114–127.
- [10] B. Temelkuran, S.D. Hart, G. Benoit, J.D. Joannopoulos, Y. Fink, Wavelength-scalable hollow optical fibres with large photonic bandgaps for CO₂ laser transmission., *Nature.* 420 (2002) 650–653.
- [11] S.D. Hart, G.R. Maskaly, B. Temelkuran, P.H. Prideaux, J.D. Joannopoulos, Y. Fink, External reflection from omnidirectional dielectric mirror fibers., *Science.* 296 (2002) 510–3.
- [12] G. Benoit, S.D. Hart, B. Temelkuran, J.D. Joannopoulos, Y. Fink, Static and Dynamic Properties of Optical Microcavities in Photonic Bandgap Yarns, *Adv. Mater.* 15 (2003) 2053–2056.
- [13] O. Shapira, K. Kuriki, N.D. Orf, A.F. Abouraddy, G. Benoit, F. Viens, et al., Surface-emitting fiber lasers, 14 (2006) 1921–1923.

- [14] A.A.M. Stolyarov, L. Wei, O. Shapira, F. Sorin, S.L. Chua, J.D. Joannopoulos, et al., Microfluidic directional emission control of an azimuthally polarized radial fibre laser, *Nat. Photonics*. 6 (2012) 229–233.
- [15] J. Ballato, T. Hawkins, P. Foy, R. Stolen, B. Kokuoz, M. Ellison, et al., Silicon optical fiber., *Opt. Express*. 16 (2008) 18675–18683.
- [16] J. Ballato, T. Hawkins, P. Foy, B. Yazgan-Kokuoz, R. Stolen, C. McMillen, et al., Glass-clad single-crystal germanium optical fiber., *Opt. Express*. 17 (2009) 8029–8035.
- [17] D. A. Coucheron, M. Fokine, N. Patil, D.W. Breiby, O.T. Buset, N. Healy, et al., Laser recrystallization and inscription of compositional microstructures in crystalline SiGe-core fibres, *Nat. Commun*. 7 (2016) 13265.
- [18] J. Ballato, T. Hawkins, P. Foy, B. Yazgan-Kokuoz, C. McMillen, L. Burka, et al., Advancements in semiconductor core optical fiber, *Opt. Fiber Technol*. 16 (2010) 399–408.
- [19] N. Healy, J.R. Sparks, R.R. He, P.J.A. Sazio, J. V Badding, A.C. Peacock, High index contrast semiconductor ARROW and hybrid ARROW fibers, *Opt. Express*. 19 (2011) 10979.
- [20] A.C. Peacock, P. Mehta, P. Horak, N. Healy, Nonlinear pulse dynamics in multimode silicon core optical fibers., *Opt. Lett*. 37 (2012) 3351–3.
- [21] N.F. Baril, R. He, T.D. Day, J.R. Sparks, B. Keshavarzi, M. Krishnamurthi, et al., Confined high-pressure chemical deposition of hydrogenated amorphous silicon, *J. Am. Chem. Soc*. 134 (2012) 19–22.
- [22] J.R. Sparks, R. He, N. Healy, M. Krishnamurthi, A.C. Peacock, P.J.A. Sazio, et al., Zinc selenide optical fibers, *Adv. Mater*. 23 (2011) 1647–1651.
- [23] J.R. Sparks, R. He, N. Healy, S. Chaudhuri, T.C. Fitzgibbons, A.C. Peacock, et al., Conformal coating by high pressure chemical deposition for patterned microwires of II-VI semiconductors, *Adv. Funct. Mater*. 23 (2013) 1647–1654.
- [24] M. Bayindir, F. Sorin, A.F. Abouraddy, J. Viens, S.D. Hart, J.D. Joannopoulos, et al., Metal-insulator-semiconductor optoelectronic fibres., *Nature*. 431 (2004) 826–9.
- [25] A.F. Abouraddy, O. Shapira, M. Bayindir, J. Arnold, F. Sorin, D.S. Hinczewski, et al., Large-scale optical-field measurements with geometric fibre constructs., *Nat. Mater*. 5 (2006) 532–6.
- [26] F. Sorin, G. Lestoquoy, S. Danto, J.D. Joannopoulos, Y. Fink, Resolving optical illumination distributions along an axially symmetric photodetecting fiber., *Opt. Express*. 18 (2010) 24264–75.

- [27] F. Sorin, O. Shapira, A.F. Abouraddy, M. Spencer, N.D. Orf, J.D. Joannopoulos, et al., Exploiting Collective Effects of Multiple Optoelectronic Devices Integrated in a Single Fiber, 9 (2009) 2630–5.
- [28] F. Sorin, A.F. Abouraddy, N. Orf, O. Shapira, J. Viens, J. Arnold, et al., Multimaterial Photodetecting Fibers: a Geometric and Structural Study, *Adv. Mater.* 19 (2007) 3872–3877.
- [29] A. Gumennik, A.M. Stolyarov, B.R. Schell, C. Hou, G. Lestoquoy, F. Sorin, et al., All-in-fiber chemical sensing., *Adv. Mater.* 24 (2012) 6005–9.
- [30] S. Danto, F. Sorin, N.D. Orf, Z. Wang, S.A. Speakman, J.D. Joannopoulos, et al., Fiber field-effect device via in situ channel crystallization., *Adv. Mater.* 22 (2010) 4162–6.
- [31] M. Bayindir, A. F. Abouraddy, J. Arnold, J.D. Joannopoulos, Y. Fink, Thermal-Sensing Fiber Devices by Multimaterial Codrawing, *Adv. Mater.* 18 (2006) 845–849.
- [32] M. Bayindir, O. Shapira, D. Saygin-Hinczewski, J. Viens, A.F. Abouraddy, J.D. Joannopoulos, et al., Integrated fibres for self-monitored optical transport, *Nat. Mater.* 4 (2005) 820–825.
- [33] R. He, P.J.A. Sazio, A.C. Peacock, N. Healy, J.R. Sparks, M. Krishnamurthi, et al., Integration of gigahertz-bandwidth semiconductor devices inside microstructured optical fibres, *Nat. Photonics.* 6 (2012) 174–179.
- [34] N.D. Orf, O. Shapira, F. Sorin, S. Danto, M.A. Baldo, J.D. Joannopoulos, et al., Fiber draw synthesis., *Proc. Natl. Acad. Sci. U. S. A.* 108 (2011) 4743–4747.
- [35] C. Hou, X. Jia, L. Wei, A.M. Stolyarov, O. Shapira, J.D. Joannopoulos, et al., Direct atomic-level observation and chemical analysis of ZnSe synthesized by in situ high-throughput reactive fiber drawing, *Nano Lett.* 13 (2013) 975–979.
- [36] C. Hou, X. Jia, L. Wei, S.-C. Tan, X. Zhao, J.D. Joannopoulos, et al., Crystalline silicon core fibres from aluminium core preforms, *Nat. Commun.* 6 (2015) 6248.
- [37] D.S. Deng, N.D. Orf, A.F. Abouraddy, A.M. Stolyarov, J.D. Joannopoulos, H.A. Stone, et al., In-fiber semiconductor filament arrays., *Nano Lett.* 8 (2008) 4265–9.
- [38] D.S. Deng, J.C. Nave, X. Liang, S.G. Johnson, Y. Fink, Exploration of in-fiber nanostructures from capillary instability, *Opt. Express.* 19 (2011) 16273–16290.
- [39] J.J. Kaufman, G. Tao, S. Shabahang, D.S. Deng, Y. Fink, A.F. Abouraddy, Thermal drawing of high-density macroscopic arrays of well-ordered sub-5-nm-diameter nanowires, *Nano Lett.* 11 (2011) 4768–4773.
- [40] B. Gates, B. Mayers, B. Cattle, Y. Xia, Synthesis and Characterization of Uniform Nanowires of Trigonal Selenium, *Adv. Funct. Mater.* 12 (2002) 219.

- [41] S. Shabahang, J.J. Kaufman, D.S. Deng, A.F. Abouraddy, Observation of the Plateau-Rayleigh capillary instability in multi-material optical fibers, *Appl. Phys. Lett.* 99 (2011) 57–60.
- [42] J.J. Kaufman, G. Tao, S. Shabahang, E.-H. Banaei, D.S. Deng, X. Liang, et al., Structured spheres generated by an in-fibre fluid instability., *Nature*. 487 (2012) 463–7.
- [43] G. Tao, J.J. Kaufman, S. Shabahang, R. Rezvani Naraghi, S. V. Sukhov, J.D. Joannopoulos, et al., Digital design of multimaterial photonic particles, *Proc. Natl. Acad. Sci.* 113 (2016) 201601777.
- [44] J.J. Kaufman, R. Ottman, G. Tao, S. Shabahang, E.-H. Banaei, X. Liang, et al., In-fiber production of polymeric particles for biosensing and encapsulation., *Proc. Natl. Acad. Sci. U. S. A.* 110 (2013) 15549–54.
- [45] A. Gumennik, L. Wei, G. Lestoquoy, A.M. Stolyarov, X. Jia, P.H. Rekemeyer, et al., Silicon-in-silica spheres via axial thermal gradient in-fibre capillary instabilities., *Nat. Commun.* 4 (2013) 2216.
- [46] L. Wei, C. Hou, E. Levy, G. Lestoquoy, A. Gumennik, A.F. Abouraddy, et al., Optoelectronic Fibers via Selective Amplification of In-Fiber Capillary Instabilities, *Adv. Mater.* (2016) 1–6.
- [47] M. Rein, E. Levy, A. Gumennik, A.F. Abouraddy, J.J. Joannopolous, Y. Fink, Self-assembled fibre optoelectronics with discrete translational symmetry, *Nat. Commun.* 7 (2016) 1–8.
- [48] A. Gumennik, E.C. Levy, B. Grena, C. Hou, M. Rein, A.F. Abouraddy, et al., Confined in-fiber solidification and structural control of silicon and silicon-germanium microparticles., *Proc. Natl. Acad. Sci. U. S. A.* (2017) 201707778.
- [49] M. Fokine, A. Theodosiou, S. Song, T. Hawkins, J. Ballato, K. Kalli, et al., Laser structuring, stress modification and Bragg grating inscription in silicon-core glass fibers, *Opt. Mater. Express.* 7 (2017) 1589.
- [50] N. Healy, M. Fokine, Y. Franz, T. Hawkins, M. Jones, J. Ballato, et al., CO₂ Laser-Induced Directional Recrystallization to Produce Single Crystal Silicon-Core Optical Fibers with Low Loss, *Adv. Opt. Mater.* (2016) 1004–1008.
- [51] X. Ji, S. Lei, S.-Y. Yu, H.Y. Cheng, W. Liu, N. Poilvert, et al., Single-Crystal Silicon Optical Fiber by Direct Laser Crystallization, *ACS Photonics.* 4 (2016) 85–92.
- [52] X. Ji, R.L. Page, S. Chaudhuri, W. Liu, S.Y. Yu, S.E. Mohny, et al., Single-Crystal Germanium Core Optoelectronic Fibers, *Adv. Opt. Mater.* (2016).
- [53] A.C. Peacock, J.R. Sparks, N. Healy, Semiconductor optical fibres: Progress and opportunities, *Laser Photonics Rev.* 8 (2014) 53–72.

- [54] N. Gupta, C. McMillen, R. Singh, R. Podila, A.M. Rao, T. Hawkins, et al., Annealing of silicon optical fibers, *J. Appl. Phys.* 110 (2011).
- [55] S. Morris, C. McMillen, T. Hawkins, P. Foy, R. Stolen, J. Ballato, et al., The influence of core geometry on the crystallography of silicon optical fiber, *J. Cryst. Growth.* 352 (2012) 53–58.
- [56] C. McMillen, G. Brambilla, S. Morris, T. Hawkins, P. Foy, N. Broderick, et al., On crystallographic orientation in crystal core optical fibers II: Effects of tapering, *Opt. Mater.* 35 (2012) 93–96.
- [57] S. Shaudhuri, J.R. Sparks, X. Ji, M. Krishnamurthi, L. Shen, N. Healy, et al., Crystalline Silicon Optical Fibers with Low Optical Loss, *ACS Photonics.* 3 (2016) 378–384.
- [58] W. Yan, Y. Qu, T. Das Gupta, A. Darga, D.T. Nguyễn, A.G. Page, et al., Semiconducting Nanowire-Based Optoelectronic Fibers, *Adv. Mater.* 1700681 (2017) 1700681.
- [59] W. Yan, T.D. Nguyen, C. Cayron, T. Dasgupta, A.G. Page, Y. Qu, et al., Microstructure tailoring of selenium-core multimaterial optoelectronic fibers, 7 (2017) 1135–1140.
- [60] M. Yaman, T. Khudiyev, E. Ozgur, M. Kanik, O. Aktas, E.O. Ozgur, et al., Arrays of indefinitely long uniform nanowires and nanotubes., *Nat. Mater.* 10 (2011) 494–501.
- [61] O.T. Naman, M.R. New-Tolley, R. Lwin, A. Tuniz, A.H. Al-Janabi, I. Karatchevtseva, et al., Indefinite Media Based on Wire Array Metamaterials for the THz and Mid-IR, *Adv. Opt. Mater.* 1 (2013) 971–977.
- [62] A. Tuniz, K.J. Kaltenecker, B.M. Fischer, M. Walther, S.C. Fleming, A. Argyros, et al., Metamaterial fibres for subdiffraction imaging and focusing at terahertz frequencies over optically long distances., *Nat. Commun.* 4 (2013) 2706(8).
- [63] N. Sakai, T. Kajiwara, Thermal crystallization of vitreous selenium, *Jpn. J. Appl. Phys.* 21 (1982) 1383.
- [64] F. Ye, K. Lu, Pressure effect on polymorphous crystallization kinetics in amorphous selenium, *Acta Mater.* 46 (1998) 5965–5971.
- [65] Y. Zhao, K. Zhang, K. Lu, Structure characteristics of nanocrystalline element selenium with different grain sizes, *Phys. Rev. B.* 56 (1997) 14322–14329.
- [66] Y. Zhao, K. Lu, Grain-size dependence of thermal properties of nanocrystalline elemental selenium studied by x-ray diffraction, *Phys. Rev. B.* 56 (1997) 14330–14337.
- [67] D.W. deQuiletters, S.M. Vorpahl, S.D. Stranks, H. Nagaoka, G.E. Eperon, M.E. Ziffer, et al., Impact of microstructure on local carrier lifetime in perovskite solar cells, *Science* 348 (2015) 683–86

- [68] C.H. Seager, Grain Boundaries in polycrystalline silicon, *Rev. Mater. Sci* 15 (1985) 271–302.
- [69] K. Hu, H. Chen, M. Jiang, F. Teng, L. Zheng, X. Fang, Broadband Photoresponse Enhancement of a High-Performance *t*-Se Microtube Photodetector by Plasmonic Metallic Nanoparticles, *Adv. Funct. Mater.* 26 (2016) 6641–48.
- [70] Y. Jiang, W.J. Zhang, J.S. Jie, X.M. Meng, X. Fan, S.T. Lee, Photoresponse properties of CdSe single-nanoribbon photodetectors, *Adv. Funct. Mater.* 17 (2007) 1795–1800.
- [71] Y. Lee, J. Kwon, E. Hwang, C.H. Ra, W.J. Yoo, J.H. Ahn, et al., High-performance perovskite-graphene hybrid photodetector, *Adv. Mater.* 27 (2015) 41–46.
- [72] E. Horváth, M. Spina, Z. Szekrényes, K. Kamarás, R. Gaal, D. Gachet, et al., Nanowires of Methylammonium Lead Iodide (CH₃NH₃PbI₃) prepared by low temperature solution-mediated crystallization, *Nano Lett.* 14 (2014) 6761–6766.
- [73] E. Oksenberg, R. Popovitz-Biro, K. Rechav, E. Joselevich, Guided Growth of Horizontal ZnSe Nanowires and their Integration into High-Performance Blue-UV Photodetectors, *Adv. Mater.* (2015)
- [74] J.A.Dantzig and M. Rappaz, *Solidification*, EPFL Press, 2009.
- [75] A. Mariaux, M. Rappaz, Influence of anisotropy on heterogeneous nucleation, *Acta Mater.* 59 (2011) 927–933.
- [76] K.E.E. D.A. Porter, *Phase Transformations in Metals and Alloys*, New York, Van Nostrand Reinhold, 1981.
- [77] Y. Li, F. Qian, J. Xiang, C.M. Lieber, Nanowire electronic and optoelectronic devices, *Mater. Today.* 9 (2006) 18–27.
- [78] K.S. Suslick, Sonochemistry, *Science* 247 (1990) 1439–45.
- [79] B.T. Mayers, K. Liu, D. Sunderland, Y. Xia, Sonochemical synthesis of trigonal selenium nanowires, *Chem. Mater.* 15 (2003) 3852–3858.
- [80] S. Chaudhary, A. Umar, S.K. Mehta, Selenium Nanomaterials: An Overview of Recent Developments in Synthesis, Properties and Potential Applications, *Prog. Mater. Sci.* 83 (2016) 270–329.
- [81] P. Cherin, P. Unger, The crystal structure of trigonal selenium, *Inorg. Chem.* 6 (1967) 1589–1591.
- [82] A. Tkatchenko, R.A. Distasio, R. Car, M. Scheffler, Accurate and efficient method for many-body van der Waals interactions, *Phys. Rev. Lett.* 108 (2012) 1–5.

- [83] A. Ambrosetti, A.M. Reilly, R.A. Distasio, A. Tkatchenko, Long-range correlation energy calculated from coupled atomic response functions, *J. Chem. Phys.* 140 (2014).
- [84] V. Blum, R. Gehrke, F. Hanke, P. Havu, V. Havu, X. Ren, et al., Ab initio molecular simulations with numeric atom-centered orbitals, *Comput. Phys. Commun.* 180 (2009) 2175–2196.
- [85] E. Van Lenthe, E.J. Baerends, J.G. Snijders, Relativistic regular two-component Hamiltonians, *J. Chem. Phys.* 99 (1993) 4597.
- [86] J. Perdew, A. Ruzsinszky, G. Csonka, O. Vydrov, G. Scuseria, L. Constantin, et al., Restoring the Density-Gradient Expansion for Exchange in Solids and Surfaces, *Phys. Rev. Lett.* 100 (2008) 136406.
- [87] Y. Jiang, W.J. Zhang, J.S. Jie, X.M. Meng, X. Fan, S.T. Lee, Photoresponse properties of CdSe single-nanoribbon photodetectors, *Adv. Funct. Mater.* 17 (2007) 1795–1800.
- [88] J. Miao, W. Hu, N. Guo, Z. Lu, X. Liu, L. Liao, et al., High-responsivity graphene/InAs nanowire heterojunction near-infrared photodetectors with distinct photocurrent on/off ratios, *Small.* 11 (2015) 936–942.
- [89] S. Ye, A.R. Rathmell, Z. Chen, I.E. Stewart, B.J. Wiley, Metal nanowire networks: The next generation of transparent conductors, *Adv. Mater.* 26 (2014) 6670–6687.
- [90] R. Yamauchi, S. Hata, J. Sakurai, A. Shimokohbe, Combinatorial Search for Low Resistivity Pd–Cu–Si Thin Film Metallic Glass Compositions, *Jpn. J. Appl. Phys.* 45 (2006) 5911–5919.
- [91] E. Bryn Pitt, G. Kumar, J. Schroers, Temperature dependence of the thermoplastic formability in bulk metallic glasses, *J. Appl. Phys.* 110 (2011) 043518.
- [92] G. Kumar, H.X. Tang, J. Schroers, Nanomoulding with amorphous metals., *Nature.* 457 (2009) 868–72.
- [93] G. Kumar, A. Desai, J. Schroers, Bulk metallic glass: the smaller the better., *Adv. Mater.* 23 (2011) 461–76.
- [94] S. Sohn, Y. Jung, Y. Xie, C. Osuji, J. Schroers, J.J. Cha, Nanoscale size effects in crystallization of metallic glass nanorods, *Nat. Commun.* 6 (2015) 1–6.
- [95] D.S. Hecht, L. Hu, G. Irvin, Emerging transparent electrodes based on thin films of carbon nanotubes, graphene, and metallic nanostructures., *Adv. Mater.* 23 (2011) 1482–513.
- [96] J. Schroers, W.L. Johnson, Ductile bulk metallic glass, *Phys. Rev. Lett.* 93 (2004) 255506.
- [97] X.K. Xi, D.Q. Zhao, M.X. Pan, W.H. Wang, Y. Wu, J.J. Lewandowski, Fracture of brittle metallic glasses: Brittleness or plasticity, *Phys. Rev. Lett.* 94 (2005) 25–28.

- [98] C.C. Hays, C.P. Kim, W.L. Johnson, Microstructure controlled shear band pattern formation and enhanced plasticity of bulk metallic glasses containing in situ formed ductile phase dendrite dispersions, *Phys. Rev. Lett.* 84 (2000) 2901–2904.
- [99] D.C. Hofmann, J. Suh, A. Wiest, G. Duan, M. Lind, M.D. Demetriou, et al., Designing metallic glass matrix composites with high toughness and tensile ductility, *Nature*. 451 (2008) 1085–1090.
- [100] S. Tomotika, On the Instability of a Cylindrical Thread of a Viscous Liquid Surrounded by Another Viscous Fluid, *Proc. R. Soc. Lond. A* 150 (1935) 322–37.
- [101] L. Battezzati, A.L. Greer, The viscosity of liquid metals and alloys, *Acta Metall.* 37 (1989) 1791–1802.
- [102] P. Bordeenithikasem, S. Sohn, Z. Liu, J. Schroers, Protocols for multi-step thermoplastic processing of metallic glasses, *Scr. Mater.* 104 (2015) 56–59.

Curriculum Vitae

Wei Yan

- EPFL-IMX-FIMAP, Lausanne, Switzerland
- Email: wei.yan@epfl.ch
- Office: +41 21 693 4798, Cell : +41 76 795 15 43
- Website: <http://fimap.epfl.ch/page-96206-en.html>

Education and Training

- 09/2013 – now **Ecole Polytechnique Fédérale de Lausanne (EPFL)**, Lausanne, Switzerland.

PhD candidate, Materials Science, Laboratory of Photonic Materials and Fiber Devices

Advisor: Prof. Fabien Sorin
- 11/2014 – 12/2014 **Massachusetts Institute of Technology (MIT)**, Cambridge MA, U.S.

Visiting researcher, Research Laboratory of Electronics

Advisor: Prof. Yoel Fink
- 09/2010 – 06/2013 **Chinese Academy of Sciences (CAS)**, Shenyang, China

Master, Materials Science, Shenyang National Laboratory for Materials Science

Advisor: Prof. Dianzhong Li
- 09/2006 – 06/2010 Central South University (CSU), Changsha, China

Bachelor, Materials Science, State Key Laboratory of Powder Metallurgy

GPA: 89.8/100 or 3.8/4.0 RANK: 1/93

Peer-reviewed Articles

PhD Work

13. **Wei Yan**, Inès Richard, Fabien Sorin* et al. Metallic glass nanostructured fibers. Prepare to submit to Nature Materials.
12. **Wei Yan**, Fabien Sorin* et al. Crystallographically aligned semiconductor in optoelectronic fibers for high-performance flexible photodetectors. Prepare to submit to Advanced Functional Materials.
11. Yunpeng Qu, **Wei Yan**, Fabien Sorin* et al. Super-elastic multi-material electronic and photonic fibers via thermal drawing. Submitted to Nature.

10. Fabien Sorin*, **Wei Yan**, Marco Volpi, Alexis Page, Tùng Nguyễn-Dang, Yunpeng Qu. Multi-material optoelectronic fiber devices. **Proc. SPIE Defense+Security**, 10194, 1019407-1, 2017 (**Invited Paper**)
9. **Wei Yan**, Yunpeng Qu, Tapajyoti Das Gupta, Arouna Darga, Tùng Nguyễn-Dang, Alexis Page, Mariana Rossi, Michele Ceriotti, Fabien Sorin*. Semiconducting nanowire-based optoelectronic fibers. **Advanced Materials**, 29 (2017) 1700681.
8. **Wei Yan**, Tùng Nguyễn-Dang, Cyril Cayron, Tapajyoti Das Gupta, Alexis Page, Yunpeng Qu, Fabien Sorin*. Microstructure tailoring selenium-core multimaterial optoelectronic fibers. **Optical Materials Express**, 7 (2017) 1388 (**Editor's pick**)
7. **Wei Yan**, Yunpeng Qu, Tùng Nguyễn-Dang, Marco Volpi, Alexis G r ald Page, Fabien Sorin*. Multi-material optical fibers with integrated optoelectronic devices. **Proceedings of the ACP 2016**, paper AF3A.3 (2016) – **Awarded Best Student Paper Award**.
6. Tùng Nguyễn-Dang, Alba C. de Luca, **Wei Yan**, Yunpeng Qu, Alexis Page, Marco Volpi, Tapajyoti Das Gupta, St phanie P. Lacour, Fabien Sorin*. Controlled sub-micrometer hierarchical textures engineered in polymeric fibers and micro-channels via thermal drawing. **Advanced Functional Materials**, 27 (2017) 1605935.
5. Yi Zhang, Zhaofer Zhang, **Wei Yan**, Bao Zhang, Yaqing Feng, Abdullah M. Asiri, Mohammad Khaja Nazeeruddin*, Peng Gao*. Hexagonal mesoporous silica islands to enhance photovoltaic performance of planar junction perovskite solar cells. **Journal of Materials Chemistry A**, 5 (2017) 1415.
4. Tùng Nguyễn-Dang, Alexis Page, Yunpeng Qu, **Wei Yan**, Marco Volpi, Fabien Sorin*. Multi-material micro-electromechanical fibers with bendable functional domains. **Journal of Physics D: Applied Physics**, 50 (2017) 144001. (Invited Paper)

Master Work

3. **Wei Yan**, Namin Xiao*, Yun Chen, Dianzhong Li. Phase-field modeling of Widmanst tten ferrite formation during isothermal transformation in low carbon steels. **Computational Materials Science**, 81 (2014) 503.

Bachelor Work

2. **Wei Yan**, Yong Liu*, Yitian Zhu, Sen Niu. Glass-forming ability and thermal stability of gas-atomized Zr50Cu40Al10 metallic glass powders. **International Journal of Materials Research**, 102 (2011) 435.
1. Yong Liu*, Yitian Zhu, Fei Li, **Wei Yan**. Processing porous bulk metallic glass using prealloyed powders. **Advanced Engineering Materials**, 12 (2010) 1131.

Patents

3. Fabien Sorin, Yunpeng Qu, **Wei Yan**, Tùng Nguyễn-Dang, Marco Volpi, Alexis Page. Multi-material stretchable optical, electronic and optoelectronic fibers and ribbons composites via thermal drawing. EP 2016. European Patent: WO2017137945(A1).
2. Fabien Sorin, Tùng Nguyễn-Dang, **Wei Yan**, Alexis Page. Fabrication method of functional micro/nano structures over large-area, flexible and high curvature surfaces, by drawing a fiber from a preform. European Patent: WO2017085323 (A1).
1. Yong Liu, Fei Li, Yitian Zhu, **Wei Yan**. A thermal forming technique of fabricating porous bulk metallic glass using powders. Application number: 201010298619.7 (Chinese Patent)

Invited Presentations

15. **Wei Yan**, Fabien Sorin*. Tailoring Semiconductors Microstructure in Optoelectronic Fiber Devices. WSOF, Limassol, Cyprus (2017)
14. Fabien Sorin, Tùng Nguyễn-Dang, **Wei Yan**, Yunpeng Qu, Alexis Page, Tapajyoti Das Gupta. Surface Textured Multi-material Fibers. ELEO-PR | OECC | PGC, Singapore (2017)
13. Fabien Sorin, Yunpeng Qu, Tùng Nguyễn-Dang, **Wei Yan**, Alexis Page, Tapajyoti Das Gupta, Federica Sordo. Engineering Surface and Rheological Properties for the Next Generation of Thermally Drawn Fiber-based Devices. ELEO-PR | OECC | PGC, Singapore (2017)
12. **Wei Yan**, Yunpeng Qu, Tùng Nguyễn-Dang, Tapajyoti Das Gupta, Alexis Page, Fabien Sorin*. In-fiber high performance monocrystalline semiconducting nanowires-based optoelectronic devices. IMX Research Day, EPFL (2017) (Invited)
11. Tùng Nguyễn-Dang, Alexis Page, Yunpeng Qu, **Wei Yan**, Fabien Sorin. Thermally Drawn Multi-material Fibers: a Novel Opportunity for Advanced Electronic Fibers and Textiles. European Materials Research Society, spring, Strasbourg, France (2017)
10. Fabien Sorin*, **Wei Yan**, Marco Volpi, Alexis Page, Tùng Nguyễn-Dang, Yunpeng Qu. Multi-material optoelectronic fiber devices. SPIE Defense + Commercial Sensing 2017, Anaheim, California.
9. **Wei Yan**, Yunpeng Qu, Tapajyoti Das Gupta, Tùng Nguyễn-Dang, Alexis Page, Fabien Sorin*. Microstructure tailoring of semiconducting materials within high performance optoelectronic fibers. The Fiber Society, spring, Germany (2017).
8. **Wei Yan**, Tùng Nguyễn-Dang, Yunpeng Qu, Tapajyoti Das Gupta, Marco Volpi, Alexis Page, Fabien Sorin*. In-Fiber high performance monocrystalline semiconducting nanowires-based optoelectronic devices. Materials Research Society, spring, U.S. (2017)
7. Fabien Sorin, Tùng Nguyễn-Dang, **Wei Yan**, Alexis Page, Yunpeng Qu, Marco Volpi, Shahrzad Shadman, Tapajyoti Das Gupta, Federica Sordo. Tailoring Surface and Rheological Properties of Fiber Materials: Novel Scientific Insight and Opportunities for Multi-Material Fibers. Materials Research Society, spring, Phoenix, U.S. (2017)
6. Tùng Nguyễn-Dang, Alexis Page, **Wei Yan**, Yunpeng Qu, Tapajyoti Das Gupta, Marco Volpi, Fabien Sorin*. Novel method for micro/nano patterning using fiber thermal drawing technique. Materials Research Society, spring, Phoenix, U.S. (2017)
5. Alexis Page, Tùng Nguyễn-Dang, Yunpeng Qu, Marco Volpi, **Wei Yan**, Fabien Sorin*. Multi-Material fibers for electromechanical touch sensing. Materials Research Society, spring, Phoenix, U.S. (2017)
4. Fabien Sorin*, Yunpeng Qu, Tapajyoti Das Gupta, Tùng Nguyễn-Dang, **Wei Yan**, Alexis Page, Marco Volpi. Multi-material hybrid optical fibers. Société Française d'Optique, Bordeaux (2016)
3. Fabien Sorin*, **Wei Yan**, Yunpeng Qu, Tapajyoti Das Gupta, Tùng Nguyễn-Dang, Alexis Page, Marco Volpi. Novel fabrication approaches of 1D and 2D nanostructured photonic systems. 6th Nano Science & Technology Conference, Singapore (2016)
2. **Wei Yan**, Fabien Sorin*. Promises of multi-material fiber devices for advanced light delivery systems. Swiss National Fiber Laboratory (SNFL, Swiss Photonics) Workshop, Burdgof, Switzerland, (2015)
1. Tùng Nguyễn-Dang, **Wei Yan**, Fabien Sorin*. Recent development and opportunities of Multi-material optoelectronic fibres. PIERS 2014, Guangzhou, China

Awards & Honors

06/2017 **Nominated Best Graduate Student** at EDMX Research Day, EPFL

11/2016	Best Student Paper Award at ACP 2016, The Optical Society.
04/2016	Reviewer of Optical Materials Express
07/2017	Reviewer of Optics Letters
08/2017	Reviewer of Applied Optics
Prior to EPFL	
2010	Best Undergraduate Thesis Award at CSU
2008	National Scholarship (highest national award for undergraduates)
2007, 2010	National Encouragement Scholarship (2nd highest national award for undergraduates)
2010	Outstanding Graduates Award of Hunan Province (award for TOP 1% undergraduates)
2009	Southwest Aluminum Group Co., LTD Educational Scholarship (highest enterprise scholarship for TOP 1% undergraduates)
2008	Huang Peiyun Educational Scholarship (scholarship for TOP 1% undergraduates)
2009	Pacemaker to Merit Student at CSU (award for TOP 1% undergraduates)
2007, 2008	Merit Student award of CSU (award for TOP 3% undergraduates)
2008-2010	The First-Class scholarship at CSU (scholarship for TOP 1% undergraduates)

Mentoring

I have trained and guided 8 master students for their semester projects.